NANO-BIOTHIOL INTERACTIONS OF ENGINEERED NANOPARTICLES

by

Qinhan Zhou

APPROVED BY SUPERVISORY COMMITTEE:

_____

Jie Zheng, Chair

_____

Bruce E. Gnade

_____

Steven O. Nielsen

_____

Gabriele Meloni

_____

Sheena D'Arcy

This work is dedicated to my family.

NANO-BIOTHIOL INTERACTIONS OF ENGINEERED NANOPARTICLES

by

QINHAN ZHOU, BS

DISSERTATION

Presented to the Faculty of

The University of Texas at Dallas

in Partial Fulfillment

of the Requirements

for the Degree of

DOCTOR OF PHILOSOPHY IN

CHEMISTRY

THE UNIVERSITY OF TEXAS AT DALLAS

December 2021

ACKNOWLEDGMENTS

I would like to sincerely thank my PhD advisor, Dr. Jie Zheng, for his support throughout my entire PhD program. I was inspired by his passion for science. Meanwhile, his attitude towards research sets a standard for me when I encountered the choices for my future academic career. I would also like to thank my committee members, Dr. Gnade, Dr. Nielsen, Dr. Meloni, and Dr. D'Arcy, for their support and valuable suggestions on my qualifying exam and committee meetings. I would also thank Dr. Kesden for his help on my final oral exam.

I would like to thank all the group members in the Zheng group for their help in my research program. I would like to thank Dr. Yu for her suggestion on my research projects and her help on the liver GSH measurement experiments. I would like to thank Dr. Tang for his suggestions on my choice for the academic career and his kindness for my daily life. I sincerely thank my former colleagues, Dr. Du, Dr. Jiang, and Dr. Peng, who taught me the experimental skills after I joined Dr. Zheng's lab. I also want to thank Dr. Ning for all his help in my daily life. I would like to sincerely thank Dr. Huang. We are friends for over 11 years. He generously helped me in my research and daily life, I hope we both can conquer the difficulty for in our future career. I would like to sincerely thank Siqing Li, for her support and help in research and daily life. I hope Siqing and I can support each other to meet the numerous challenges and enjoy the scenery along the way of our future life. I want to thank Chong Yue. He taught me a lot of things regarding clinical practice. I also want to thank Dr. Yan for her generous help in my daily life. I would also like to thank Samira, Simin, Wei Xiao, and my former colleague, Dr. Linxi Shi for their help in my research. I would like to thank Li Wan for his help on the cancer cell culture and tumor implantation.

I would like to thank Dr. Jer-Tsong Hsieh and his group member Elizabeth Hernandez from the Department of Urology, The University of Texas Southwestern Medical Center, for their help on tissue processing. I would like to thank Dr. Liu from The University of Texas Southwestern Medical Center for the tumor model offering.

I would like to thank all the faculty and staff in the Department of Chemistry and Biochemistry and the core facilities of UTD. Special thanks to Betty Maldonado, Kelli Lewis, Dr. Qingxiao Wang, and Dr. Ved Prakash. I would also like to thank all my friends at UTD, Jason Lin, Dr. Wang, Dr. Du, Dr. Ren, Dr. Wang, Dr. Zhang, Ziyuan Ma, Yafen Tian.

November 2021

NANO-BIOTHIOL INTERACTIONS OF ENGINEERED NANOPARTICLES

Qinhan Zhou, PhD
The University of Texas at Dallas, 2021

Supervising Professor: Dr. Jie Zheng

Nanomedicines have been extensively studied in the past decades at the fundamental level because they could potentially make a paradigm shift in human healthcare. Nano-bio interactions play a central role in the precise control of the benefit and hazards of nanomedicines, but current studies mainly focus on how nanoparticles are taken up by cells and interact with different receptors. There is still not enough investigation of how the physiological environment transforms engineered nanoparticles through a variety of biochemical reactions. This dissertation aims to fundamentally understand the nanoparticle-biochemical interactions and the *in vivo* transport of engineered nanoparticles modulated by these interactions.

In Chapter 1 of this dissertation, an overall review is given on the current understanding of nano-bio interactions at the molecular and chemical levels, particularly. In Chapter 2, we systematically investigated how the nanoparticle size, the thiols species, and the protein binding affect the interactions between the nanoparticles and thiols at the *in vitro* level. In Chapter 3, we focused on unraveling the relation between the nanoparticle-biothiol interactions *in vitro* and the nanoparticle-biothiol interactions *in vivo*. In Chapter 4, we explored the nanoparticle-biothiol interactions in the diseased mice model and illustrated the application of nanoparticle-biothiol

interactions in disease diagnosis. Finally, in Chapter 5, we present the summary and outlook. These new understanding on nano-biochemical interactions at both *in vitro* and *in vivo* levels will help further advance physiology at the nanoscale as well as open new pathways to early disease diagnosis and treatment.

TABLE OF CONTENTS

LIST OF FIGURES

LIST OF TABLES

CHAPTER 1

OVERVIEW OF NANO-BIOCHEMICAL INTERACTIONS

1.1 Introduction of nano-biochemical interactions

Over the past decades, engineered nanomaterials have been rapidly developed for therapeutic purposes like disease detection and treatment[1-6]. Because of the unique physicochemical properties, the engineered nanomaterials have been widely applied in different biomedical applications like drug delivery[1, 2], bioimaging[3, 7, 8], disease diagnosis[9, 10], and gene therapy[11, 12], etc. Though tremendous strategies have been designed, few of these engineered nanomaterials have been approved nor been utilized in the clinic[13]. Most engineered nanomaterials exhibit nonspecific distribution[14] and low target efficiency to desired diseased sites like tumors after administration[13, 14]. These problems need to be solved so that the clinical translation of engineered nanomaterials can be promoted. Therefore, fundamental understanding of the nanomaterials *in vivo* behaviour is critical to solving the problems that exist currently and provides a solid foundation for the rational design of nanomaterials for biomedical use in the future.

The understanding of the nanomaterial's *in vivo* behaviour includes investigating the absorption, distribution, metabolism, and excretion, namely ADME[15, 16]. The investigation of the ADME process of nanomaterials is to fundamentally understand the interaction between nanomaterials and the biostructures/biochemicals, as well as investigate the *in vivo* transport of nanomaterials after administration, as shown in Figure 1.1. Briefly, upon intravenous injection, nanomaterials enter the blood circulation system[17, 18], and are distributed into organs and tissues[19, 20], followed

by being excreted out of the body through hepatic and/or renal systems[21-23]. In the bloodstream, nanomaterials first interact with various biomolecules and biochemicals, such as proteins and peptides. Such interactions between nanomaterials and biochemicals would change the physicochemical properties (like size, shape, and surface chemistry) of the nanomaterials[24, 25]. This is the first type of nano-bio interaction of the nanomaterials after administration.

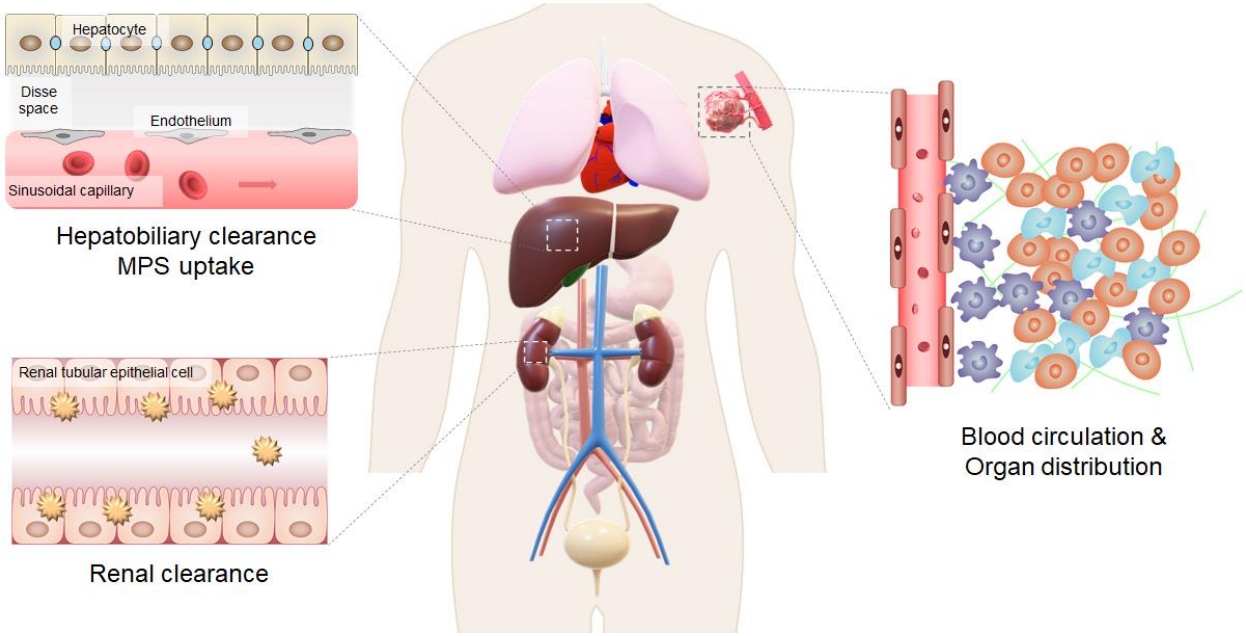

Figure 1.1. A journey of engineered nanomaterials in the body. After systematic administration, engineered nanomaterials will circulate the body through the blood vessel and extravasate from the blood vessel to different organs and tissues including the tumor. After that, these circulating nanomaterials will be eliminated through three main mechanisms: 1, renal clearance through glomerular filtration or tubular secretion in the kidney; 2, hepatobiliary clearance through the hepatocytes in the liver; 3, uptake by the mononuclear phagocyte system like Kupffer cells in the liver which is the so-called MPS uptake.

After the first type of nano-bio interactions, usually, a layer of protein corona will be formed at the surface of administrated nanomaterials. The formation of protein corona will not only alter the physicochemical properties of administrated nanomaterials but also lead to the sequestration of administrated nanomaterials by the mononuclear phagocyte system[26] (MPS). This is the

second nano-bio interaction that the nanomaterials will meet after their administration. During the circulation of nanomaterials in the bloodstream, a portion of such nanomaterials will interact with endothelial cells and extravasate the blood vessels[27, 28]. This is the third type of nano-bio interaction the nanomaterials will meet after administration. It is noteworthy here that if the size of nanomaterials is smaller than 5.5 nm, these nanomaterials are probably filtrated out and will be eliminated into the urine when they "pass-through" the glomerulus[29-31].

After the extravasation of the blood vessels, the nanomaterials will interact with the interstitial fluid and cells in the tissue and organs. For most types of engineered nanoparticles, this should be the last type of nano-bio interactions that nanomaterials will encounter *in vivo*. After this type of nano-bio interaction, the nanomaterials either will be metabolized inside the cells and then eliminated through the urinary/biliary system or sequestrated inside the cells for quite a long time[32]. Some types of engineered nanoparticles will interact with the biochemicals in the urine, bile, and feces after the elimination process through the urinary/biliary system[33, 34], and this is the fifth type of nano-bio interaction.

Therefore, there are typically five types of nano-bio interactions in the *in vivo* fate of the administrated nanomaterials. These five types of nano-bio interactions can be further divided into two parts: nano-biostructure interactions and nano-biochemical interactions. Nano-biostructure interactions refer to the interactions between nanomaterials and the interactions with the cells and the interstitial matrix, while the nano-biochemical interactions refer to the interactions between nanomaterials and the non-cell components. The biochemicals are usually excreted or effluxed by the cells, thus most of the biochemicals will transport in the bloodstream. Compared to the biochemicals, the biostructures are typically static.

Researchers have now been focused on two directions to investigate the nano-biochemical interactions. In the first direction, the researchers focus on the fundamental understanding of the nano-biochemical interactions. They designed a series of nanomaterials with different physicochemical properties and then investigate how these different physicochemical properties affect the nano-biochemical interactions[35]. In this area, protein is the most frequently studied one. The effects of physical and physiochemical properties of nanomaterials like size[36-38], shape[38, 39], surface chemistry[36, 40, 41] on the interactions between nanomaterials and proteins have been systematically and comprehensively investigated at both *in vitro* level and *in vivo* level. In the second direction, the researchers deliberately modify the biological environment and then investigate how these modifications of the biological environment affect the nanoparticle-biochemical interactions[22, 42, 43]. These two methodologies are also applied in disease conditions[44-46]. The exploring of the difference of the nanoparticle-biochemical interactions in the normal and disease conditions not only provides a comprehensive understanding of the nano-bio interactions *in vivo* but also builds up a strong foundation for the design of new generation nanomaterials to achieve therapeutic use in the future.

1.2 Applications of the nano-biochemical interactions

The understanding of the nano-biochemical interactions facilitates the design and manufacture of nanomaterials with significant functionality as well as promising biomedical use. In this section, we focus on the nano-biochemical interactions in the design of nanomaterials for biomedical and biological applications. Nanochelator, reactive oxygen species (ROS) and reactive nitrogen species (RNS) scavenger, and other types of responsive nanomaterials have been designed according to their interactions with metal ions, ROS/RNS, and other types of biochemicals. The

nanoparticle-biochemical interactions which were applied in these nanomaterials can be divided into two different groups: (1) interactions between nanomaterials and extracellular biochemicals, and (2) interactions between nanomaterials and intracellular biochemicals. The significant difference between the extracellular and intracellular nanoparticle-biochemical interactions is the effect of such nanoparticle-biochemical interactions on the *in vivo* behaviour of nanoparticles. The extracellular nanoparticle-biochemical interactions would greatly alter the pharmacokinetics profiles of nanoparticles and further affect the interactions of nanoparticles with different organs and tissues. The intracellular nanoparticle-biochemical interactions typically affect the *in vivo* integrity of nanoparticles and determine the clearance pathway of nanoparticles.

1.2.1 Interactions between the nanomaterials and extracellular biochemicals

In this section, the design and application of a nanochelator, which is a typical nanoparticle-biochemical interaction (nanoparticle-metal ions interaction) will be discussed and this nanochelator would be used as an example to illustrate the design criteria of nanomaterials using the nanoparticle-biochemical interactions.

Metal ions are involved in many critical physiological processes of the human and play an essential role in several structural components of the human body. Therefore, the equilibrium of metal ions is required, and the elevation or absence of metal ions will lead to disease. Chelation is a kind of interaction between the chelators and the metal ions. Although the mechanism of chelation is not complicated, the manufacture of a nanochelator requires rational design and professional evaluation[47-51]. Usually, chelation therapy is conducted when the metal builds up to toxic concentrations in the body. Therefore, the desired nanochelator should not only efficiently bind the excess metal from in the bloodstream or the diseased tissues, but also can eliminate out

of the body with the binding metal rapidly. In 2016, Kalanaky and co-workers developed a 40 nm iron chelator-- TLc-A[47]. They found that TLc-A exhibited a higher efficiency of the remove overload iron in the Caco 2 cell line than deferoxamine (DFO), which is a clinically used iron chelator molecule. In rats with iron overload, the authors head-to head compared the iron concentration in the serum of rats injected with the same dose of TLc-A and DFO, respectively. the iron concentration in serum from the TLc-A treated mice were significantly lower than DFO treated mice. Meanwhile, compared with DFO, TLc-A also significantly reduced hepatic iron content. In 2019, Kang and co-workers utilized ε-poly-L-lysine to modify DFO and prepared the renal clearable iron chelator—DFP-NPs[49]. Compared to native deferoxamine (DFO), these DFP-NPs exhibited favourable pharmacokinetic properties, such as kidney-specific distribution and rapid renal excretion efficiency (more than 80% ID within 4 h p.i.). Apart from scavenging the excess metal ions in the bloodstream, a nanochelator has been designed to inhibit the Zn^{2+} or Cu^{2+} induced Aβ aggregation in the brain. A silica-based nanochelator, silicacyclen, was designed by Wang in 2019[50]. This type of nanochelator could effectively inhibit the Aβ aggregation. At the meantime, it can also reduce the generation of ROS induced by the Cu-Ab40 complex, thereby lessening the metal-induced Aβ toxicity. This silica-cyclen nanochelator was also proved to cross the blood-brain barriers (BBB), which may inspire the construction of novel Aβ inhibitors. Moreover, the nanochelator strategy can not only be utilized to scavenge the excess metal ions but also can be applied in the nanoparticle *in vivo* transformation. This novel strategy was reported by Yang and co-workers in 2019[48]. They designed a sub-6 nm Si-based (Imi-OSi) nanoparticle with the ability of depleting the excess copper in a tumor. Meanwhile, the Cu-binding Imi-OSi exhibited the ability to form aggregation. Such aggregation can achieve

anti-vasculature functions, demonstrating significantly enhanced tumor inhibition activity in both breast cancer and colon cancer tumor models.

In summary, the design of the nanochelator is tailoring the *in vivo* behavior of the pre-identified chelator without sacrificing the metal ion chelation efficiency. Such design criteria include: (1) Switching the pharmacokinetic profiles of the nanochelator to deliver a sufficient amount of nanochelators into the desired sites in the body, and (2) After binding the metal ions, the nanochelator with the metal ions is supposed to be eliminated out of the body instead of being taken up by the MPS. These design criteria are not limited to nanochelators but can also be applied to other nanomaterials.

1.2.2 Interactions between the nanomaterials and intracellular chemicals

In this section, we will discuss the most widely used nanoparticle-intracellular biochemical interactions—nanoparticle-ROS/RNS interactions.

Reactive oxygen species and reactive nitrogen species serve as significant components in regulating various physiological functions of living organisms. It is noteworthy that although a moderate concentration of ROS/RNS can act as a second messenger for physiological regulation, however, excessive ROS/RNS may damage cells and trigger cell death[52]. Herein, nanomaterials are designed to either generate ROS/RNS or scavenge ROS/RNS to maintain the ROS/RNS at the regular level to achieve desired therapeutic efficacy.

In cancer therapy, ROS-generated nanomaterials are widely used to generate cancer cell death. For example, Lin and co-workers reported a UCNP@TiO2 composite, in which TiO_2 was coated on the surface of the up-conversion nanoparticles (UCNP)[53]. After being irradiated by a near IR

laser, this UCNP@TiO2 composite induced the mitochondria-involved apoptosis of cancer cells. Apart from cancer, ROS depleted nanomaterials are also applied for the treatment of other diseases such as acute kidney disease[54] and inflammation[55]. For example, Li et al designed a ROS-scavenging nanomaterial for inflammation treatment[55]. This type of nanoplatform exhibited multiple ROS-scavenging capabilities ($O_2^{\bullet-}$, H_2O_2, and HClO), presenting superior therapeutic efficacy in murine models of inflammatory diseases. Meanwhile, the ROS nanosensor is regarded as a promising indicator for the early detection of the disease, like liver inflammation and drug-induced liver injury[56]. In 2004, Shuhendler first reported a semiconducting polymer-based nanosensor which can detect RNS and ROS at the same time without interference between them. The fluorescence resonance energy transfer (FRET) and chemiluminescence resonance energy transfer (CRET) were utilized for detect RNS and ROS respectively[56]. Due to such unique properties, their nanomaterials were applied in the detection of the drug-induced hepatotoxicity and its remediation through longitudinally and noninvasively monitoring the oxidative and nitrosative stress in the liver after the administration of the overdosed drugs acetaminophen and isoniazid. Based on this work, Huang and co-workers developed a renal-clearable ROS-responsive nanoreporter with the FRET/CRET, which detects the upregulation of $O_2^{\bullet-}$ and lysosomal damage (N-acetyl-b-dglucosaminidase, NAG). Due to the specificity of the response to ROS and the high renal clearance efficiency (80% injected doses after 24 h injection), their nanoreporter can detect the acute kidney injury at least 8 hours (based on fluorescence) and 16 hours (based on chemiluminescence) earlier than the significant decrease of glomerular filtration rate.

In summary, the design criteria of nanomaterials that use the nanoparticle-ROS/RNS interactions include: (1) The nanomaterials should specifically react with ROS/RNS or generate/scavenge ROS/RNS *in vivo* level, which is so-called "ROS/RNS-responsive", (2) The nanomaterials should remain unresponsive with ROS/RNS during the circulation in the body until the nanomaterials are delivered into the target cells, and (3) The response of ROS/RNS could be monitored at the *in vivo* level.

In this dissertation, a series of atomically precise gold-organic dye hybrid nanoclusters were designed with activatable fluorescence, which was utilized to explore nano-biochemical interactions, especially the nano-biothiols interactions at both *in vitro* and *in vivo* levels. At the *in vitro* level, we systematically studied how the physicochemical properties of nanoparticles, the species of the biothiols, and protein binding affect the nanoparticle-biothiol interactions. At the *in vivo* level, we investigated how the nanoparticles interact with the biothiols in the liver as well as how this interaction affects the *in vivo* transport of nanoparticles. Apart from investigating the nanoparticle-biothiol interactions in normal mice, we also explored how this interaction affects the tumor-targeting effect of nanoparticles in tumor-bearing mice. We hope that these new understanding we explored on nano-biochemical interactions at both *in vitro* and *in vivo* levels will provide the foundation for the design of new generation nanoprobes to achieve early disease diagnosis and treatment.

CHAPTER 2

NANOPARTICLE-BIOTHIOL INTERACTIONS *IN VITRO*

Authors – Qinhan Zhou, Siqing Li, Yingyu Huang, Ziyuan Ma, and Jie Zheng

Department of Chemistry and Biochemistry, BSB 13

The University of Texas at Dallas

800 West Campbell Road

Richardson, Texas 75080, USA

2.1 Abstract

Great efforts have been made to understand how nanoparticles interact with the biological structure, such as organs, tissues, and bloodstream. Meanwhile, the interactions between the nanoparticles and biochemicals like ions and molecules remain less understood. By designing a library of organic dye conjugated gold nanoparticle-ICG-AuNPs with different sizes, we systematically investigated the nanoparticle-biothiol interactions at the *in vitro* level. We studied how the physicochemical properties especially the size of the nanoparticles affects the nanoparticle-biothiol interactions. The nanoparticle-biothiol interactions of ICG-AuNPs were found to be size-dependent. Furthermore, the effect of thiol species and protein binding were also comprehensively investigated. Thiols with lower molecular weight were found to react more efficiently with ICG-AuNPs. Meanwhile, the protein binding significantly facilitates the nanoparticle-biothiol interactions at the *in vitro* level. These findings at the *in vitro* level provided a foundation for the understanding of the nanoparticle-biochemical interactions *in vivo*.

2.2 Introduction

Engineered nanoparticles have been widely applied to achieve multiple therapeutic purposes, such as bio sensing[57] and imaging[58], drug delivery[59, 60], disease diagnosis, and treatment[61] due to the outstanding physical and physiochemical properties of engineered nanomaterials. Although numerous nanomaterials have been developed so far, most nanomaterials fail in clinical trials due to the lack of efficacy and clinical safety[13]. Such circumstances mainly result from the fact that our understanding of nanomaterial–biology system (nano-bio) interactions remain insufficient[61-63]. Upon entering the biological systems, the nanoparticles will continuously interact with the

biochemicals and biostructures, which will significantly alter the *in vivo* behavior of engineered nanoparticles[15, 28, 64, 65]. Therefore, the understanding of interactions between the nanoparticles and biochemicals and biostructures is of great importance for the design of a new generation nanomedicines for clinical use. Among the numerous biochemicals, biothiols like glutathione (GSH) are synthesized in all types of cells and can be transport between different tissues and organs[66]. Therefore, there is a high chance that engineered nanoparticles would interact with biothiols during their *in vivo* journey.

In this chapter, we first systematically prepared a library of AuNPs with different sizes, which are $Au_{10\text{-}11}(SG)_{10,}$ $Au_{18}(SG)_{14}$, $Au_{25}(SG)_{18}$, and $Au_{640}(SG)_{385}$. These AuNPs with different sizes were carefully purified and characterized. After that, ICG, an organic fluorescent dye, was conjugated on the surface of different-sized AuNPs to serve as an indicator to visualize the reaction between nanoparticles and thiols under various conditions. Due to the unique optical properties of ICG conjugated AuNPs (ICG-AuNPs), that the fluorescence of ICG was completely quenched by the AuNPs and can be instantaneously recovered once the ICG molecules were released from the surface of AuNPs when ICG-AuNPs were reacted with thiols, the interaction between the nanoparticles and the thiols could be quantitatively measured. By systematically comparing the reaction kinetics of the interaction between the nanoparticles and the thiols under various conditions, the size dependency and thiol species dependency of the nanoparticle-thiol interactions *in vitro* were discovered. Furthermore, the effect of protein binding on the nanoparticle-thiol interactions *in vitro* was also investigated. The protein binding could significantly accelerate the reaction between the nanoparticles and the thiols. These findings not only provide insight into the nanoparticle-biochemical interactions at the *in vitro*

level but also provide critical information for the investigation of the nanoparticle-biochemical interactions at the *in vivo* level.

2.3 Results and discussion

2.3.1 Synthesis and characterization of the gold nanoparticles

2.3.1.1 Synthesis and purification of different sized gold nanoclusters and nanoparticles

Atomically precise gold nanoclusters: $Au_{10-11}(SG)_{10}$, $Au_{18}(SG)_{14}$, and $Au_{25}(SG)_{18}$ were synthesized according to the reported method with serval modifications[67-69]. The $Au_{10-11}(SG)_{10}$ was synthesized according to the previous published method[67] with the modification of introducing a mild reducing agent, sodium cyanoborohydride ($NaBH_3CN$). For detailed information on the synthesis and purification of $Au_{10-11}(SG)_{10}$, please see **section 2.5.2**.

For the synthesis of $Au_{18}(SG)_{14}$, the reported two-phase synthesis method[68] was modified by altering the pH of the reaction system from 2.7 to 5 to allow the reaction to be performed in one phase. Meanwhile, the amount of reducing agent-- borane tert-butylamine (TBAB) was reduced to slow down the reaction rate to avoid the formation of larger-sized gold nanoparticles. For detailed information on the synthesis and purification of $Au_{18}(SG)_{14}$, please see **section 2.5.2**.

For the synthesis of $Au_{25}(SG)_{18}$, the reported method[69] was modified by changing the strong reducing agent Sodium borohydride ($NaBH_4$) with a mild reducing agent TBAB. Meanwhile, the reaction temperature was increased from 0 ºC to room temperature to reduce the reaction time. For detailed information on the synthesis and purification of $Au_{25}(SG)_{18}$, please see **section 2.5.2**.

The synthesis method of 2 nm gold nanoparticles $Au_{640}(SG)_{385}$ was developed and published by our group previously[30, 70]. For detailed information on the synthesis and purification of $Au_{640}(SG)_{385}$, please see **section 2.5.2**.

2.2.1.2 Characterization of the purity of different sized gold nanoparticles

The purified gold nanoclusters $Au_{10\text{-}11}(SG)_{10,}$ $Au_{18}(SG)_{14}$, $Au_{25}(SG)_{18}$, and 2 nm gold nanoparticles $Au_{640}(SG)_{385}$ are monodispersed, which can be confirmed by the polyacrylamide gel electrophoresis (PAGE) as shown in Figure 2.1. Figure 2.1 represents the PAGE results of different-sized gold nanoclusters and nanoparticles under (a) visible light, and (b) UV light.

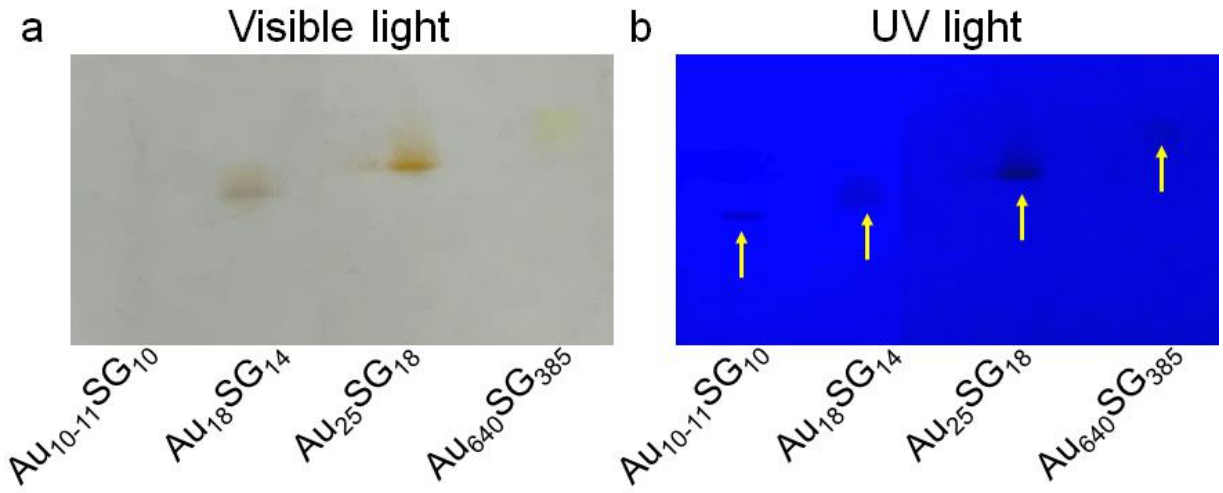

Figure 2.1. PAGE results of different sized gold nanoparticles under (a) visible light, and (b) UV light. Yellow arrows indicate the bands of different-sized gold nanoparticles under UV light.

$Au_{18}(SG)_{14}$, $Au_{25}(SG)_{18}$, and 2 nm gold nanoparticles $Au_{640}(SG)_{385}$ display one band under visible light, which indicates that there are no other sized gold nanoclusters or gold nanoparticles

formed in the products of $Au_{18}(SG)_{14}$, $Au_{25}(SG)_{18}$ and $Au_{640}(SG)_{385}$. The $Au_{10\text{-}11}(SG)_{10}$ solution is transparent, therefore, the band of $Au_{10\text{-}11}(SG)_{10}$ under visible light cannot be observed. While under UV light, $Au_{10\text{-}11}(SG)_{10}$ displays only one narrow band, suggesting the high purity of $Au_{10\text{-}11}(SG)_{10}$.

2.3.1.2 Determination of the chemical compositions of the different sized gold nanoclusters and gold nanoparticles

Nuclear magnetic resonance (NMR) has proved to be a powerful analysis technique to probe the structure information of metal nanoclusters in investigating the binding between the surface ligands with the metal core of metal nanoclusters[71, 72]. Meanwhile, it has been reported that the chemical compositions of atomically precise metal nanoclusters can be successfully determined by electrospray ionization mass spectrometry (ESI-MS)[72, 73]. Therefore, in this section, NMR and ESI-MS were employed to probe the chemical composition information of the different-sized gold nanoparticles.

The ^{1}H NMR spectra of GSH and different AuNPs are displayed in Figure 2.2. The GSH and AuNP samples were dissolved in D_2O for the NMR measurement. The proton peaks of free GSH and different AuNPs are located in the range of 2.0 to 5.0 ppm. It is noteworthy that the strong peaks at about 4.7 ppm result from the residual H_2O and HDO in the D_2O solvent. The carbon atoms in free GSH and the GSH ligands of AuNPs are labeled with the letter a-f (Figure 2.2, insets). The peak assignment of free GSH has been well-documented[71, 72]. As shown in Figure 2.2 a, the peak at 3.98 ppm is assigned to the CH_2 at C-e of GSH because it does not couple with other protons. The peak at 2.18 ppm is assigned to the CH_2 at C-a due to the coupling of two hydrogen groups. The other proton can be assigned unambiguously based on the information of

J-coupling and the integrated peaks. The peaks at 2.56 ppm, 2.96 ppm, 3.83 ppm, and 4.54 ppm are assigned to the proton of C-b, C-c, C-d, and C-f.[72] After GSH is coated on the surface of AuNPs as ligands, all the peaks of $Au_{10\text{-}11}(SG)_{10,}$ $Au_{18}(SG)_{14}$, $Au_{25}(SG)_{18}$, and $Au_{640}(SG)_{385}$ become broader compared to free GSH (Figure 2.2 b-e). The peaks of H-a, H-b, H-d, and H-e from the GSH ligands on the surface of AuNPs can be readily assigned since the chemical shifts of these protons are not significantly changed. However, the chemical shifts of H-c and H-f from the GSH ligands on the surface of AuNPs significantly downfield shift. Such downfield shift fundamentally results from the electron density of H-c (α-CH_2) and H-f (β-CH) being reduced because these protons are very close to the gold core of AuNPs which exhibits higher electronegativity than H. Combining these NMR results suggests the surface ligands of different types of AuNPs are GSH, and the ligand of GSH is coated on the gold core through the Au-S bond.

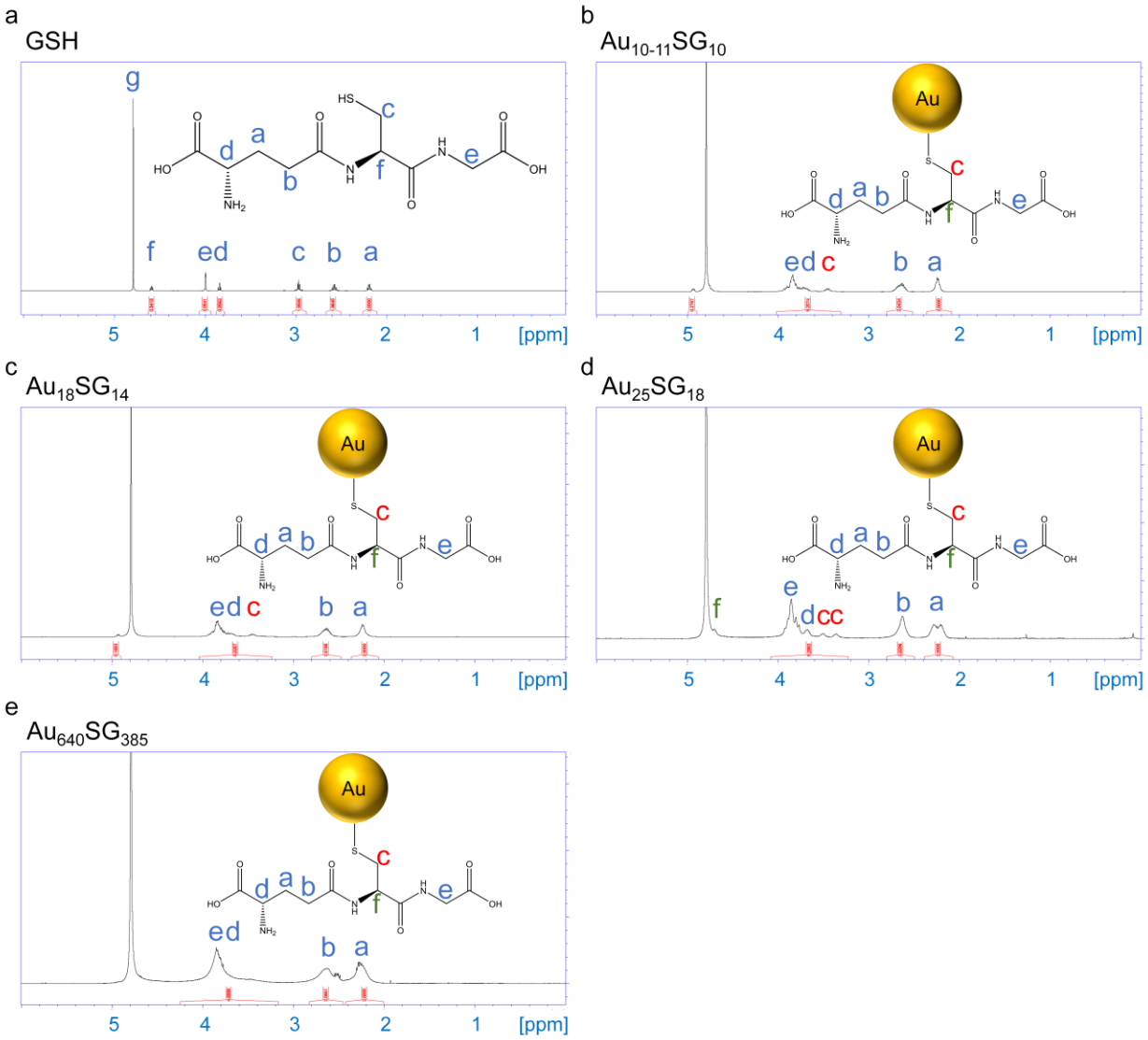

Figure 2.2. ^{1}H NMR spectra of (a) free GSH, (b) $Au_{10\text{-}11}(SG)_{10}$, (c) $Au_{18}(SG)_{14}$, (d) $Au_{25}(SG)_{18}$, and (e) $Au_{640}(SG)_{385}$. Solvent for NMR measurement: D_2O. The carbon atoms of GSH in free GSH and AuNPs were labeled as a-f with blue, red, and green colors.

Due to the high purity of as-synthesized gold nanoclusters, the chemical compositions of $Au_{10\text{-}11}(SG)_{10}$, $Au_{18}(SG)_{14}$, and $Au_{25}(SG)_{18}$ can be determined by ESI-MS. Figure 2.2 represents the negative-ion ESI mass spectra of (a) $Au_{10\text{-}11}(SG)_{10}$, (b) $Au_{18}(SG)_{14}$ and (c) $Au_{25}(SG)_{18}$, with the simulated isotope pattern of (d) $Au_{10\text{-}11}(SG)_{10}$, (e) $Au_{18}(SG)_{14}$ and (f) $Au_{25}(SG)_{18}$.

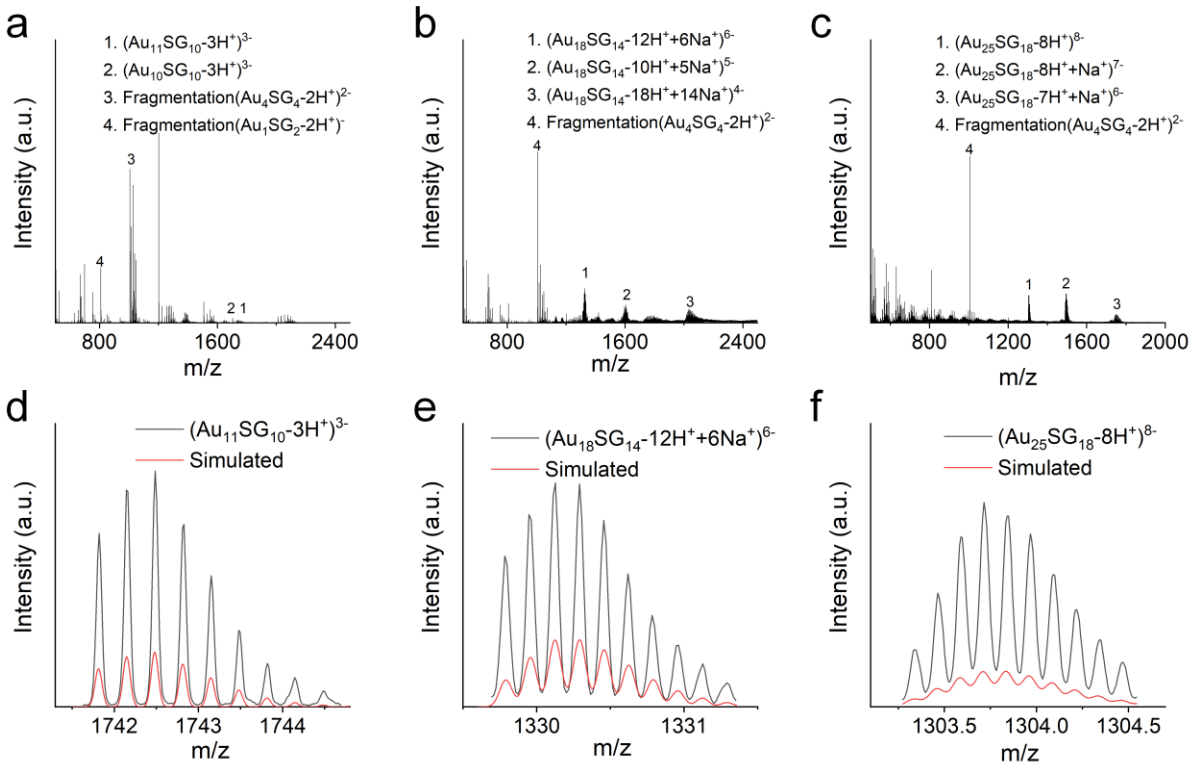

Figure 2.3. The determination of the chemical compositions of the different-sized gold nanoclusters. a-c, The negative-ion ESI mass spectra of (a) $Au_{10\text{-}11}(SG)_{10,}$ (b) $Au_{18}(SG)_{14}$ and (c) $Au_{25}(SG)_{18}$. d-f, The simulated isotope pattern of (d) $Au_{10\text{-}11}(SG)_{10,}$ (e) $Au_{18}(SG)_{14}$ and (f) $Au_{25}(SG)_{18}$.

As shown in Figure 2.3 a-c, one set of intense peaks with the *m/z* of 1005 is present in all three gold nanoclusters, which are labeled as peak 3 in $Au_{10\text{-}11}(SG)_{10}$ and are labeled as peak 4 in $Au_{18}(SG)_{14}$, $Au_{25}(SG)_{18}$. Such peaks with the *m/z* of 1005, which is consistent with the chemical composition of $[Au_4(SG)_4\text{-}2H]^{2-}$, (molecular weight of 1005.6 Da). This $[Au_4(SG)_4\text{-}2H]^{2-}$ is supposed to be the fragment formed during the ionization of $Au_{10\text{-}11}(SG)_{10,}$ $Au_{18}(SG)_{14}$, and $Au_{25}(SG)_{18.}$ In Figure 2.3 a, the peak 1 was at the *m/z* of 1742.5 in the related zoomed-in spectrum Figure 2.3 d, which is fully matched to the simulated isotope pattern of $[Au_{11}(SG)_{10}$-

$3H^+]^{3-}$. Meanwhile, peak 2 in Figure 2.3 a is also consistent with the simulated isotope pattern of $[Au_{10}(SG)_{10}\text{-}3H^+]^{3-}$. These results confirmed the chemical composition of $Au_{10\text{-}11}(SG)_{10}$. As shown in Figure 2.3 b, the peak 1, peak 2 and peak 3 of $Au_{18}(SG)_{14}$ are consistent with the simulated isotope pattern of $[Au_{18}(SG)_{14}\text{-}12H^+\text{+}6Na^+]^{6-}$, $[Au_{18}(SG)_{14}\text{-}10H^+\text{+}5Na^+]^{5-}$, and $[Au_{18}(SG)_{14}\text{-}18H^+\text{+}14Na^+]^{4-}$ (Figure 2.3 e). Similar to $Au_{18}(SG)_{14}$, $Au_{25}(SG)_{18}$ also displayed three peaks with the formula of $[Au_{25}(SG)_{18}\text{-}8H^+]^{8-}$, $[Au_{25}(SG)_{18}\text{-}8H^+\text{+}Na^+]^{7-}$, and $[Au_{25}(SG)_{18}\text{-}7H^+\text{+}Na^+]^{6-}$, which are consistent with the simulated isotope pattern (Figure 2.3 f). The sodium ion found in the ESI mass spectra of $Au_{18}(SG)_{14}$ and $Au_{25}(SG)_{18}$ was due to the addition of saturated sodium chloride solution during the purification process of $Au_{18}(SG)_{14}$ and $Au_{25}(SG)_{18}$ (see **Section 2.5.2**). The other identified peaks and the correlated simulated isotope pattern in the ESI-MS spectra are summarized in Figure 2.4.

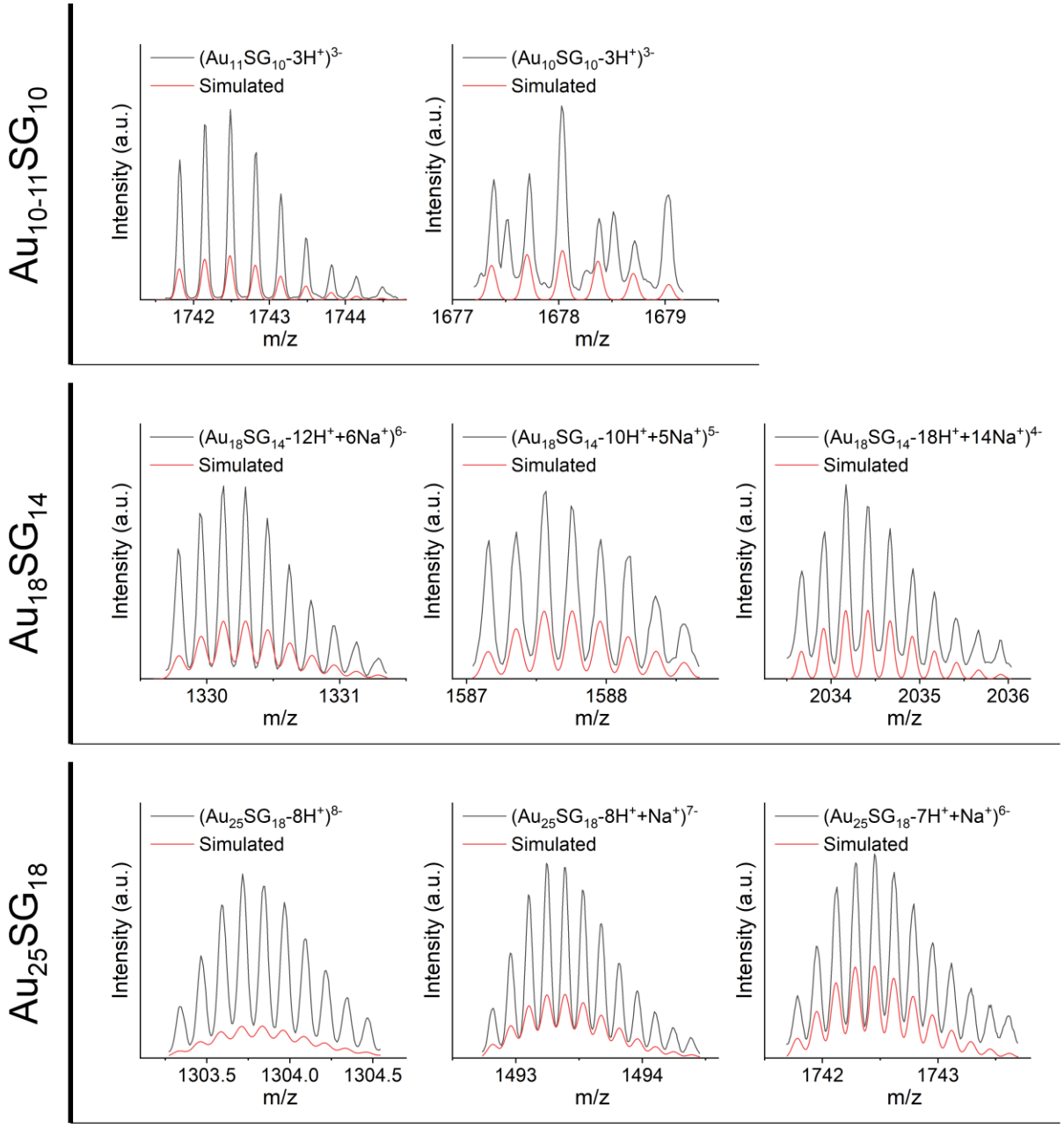

Figure 2.4. The identified peaks and simulated isotope pattern of $Au_{10\text{-}11}(SG)_{10}$, $Au_{18}(SG)_{14}$, and $Au_{25}(SG)_{18}$.

The determination of the chemical composition of 2 nm gold nanoparticles $Au_{640}(SG)_{385}$ has been reported by our group previously[70]. Unlike the atomically precise gold nanocluster $Au_{10\text{-}}$

$_{11}(SG)_{10,}$ $Au_{18}(SG)_{14}$, and $Au_{25}(SG)_{18}$, the chemical composition of 2 nm gold nanoparticle $Au_{640}(SG)_{385}$ cannot be determined by ESI-MS due to the $Au_{640}(SG)_{385}$ is not atomically monodispersed. Therefore, the Au atom (640) and GSH molecule number (385) $Au_{640}(SG)_{385}$ are the average numbers rather than the precise Au atom and GSH molecule numbers. The calculation method of Au atom and GSH molecule number is discussed in Section 2.5.2.

2.3.1.3 The Optical properties of the gold nanoclusters and nanoparticles

The purified gold nanoclusters $Au_{10-11}(SG)_{10,}$ $Au_{18}(SG)_{14}$, $Au_{25}(SG)_{18}$, and 2 nm gold nanoparticle $Au_{640}(SG)_{385}$ display different colors: the $Au_{10-11}(SG)_{10}$ solution is transparent; the color of $Au_{18}(SG)_{14}$ solution is dark gray; the solution of $Au_{25}(SG)_{18}$ displays dark brown color; the color of $Au_{640}(SG)_{385}$ is yellow (Figure 2.5 insets). It has been widely reported that the atomically precise gold nanoclusters display characteristic optical absorption spectra, and the gold nanoclusters with different sizes exhibit different characteristic absorption peaks[71, 73-75]. Figure 2.5 shows the UV-vis absorption spectrum of different sized gold nanoparticles $Au_{10-11}(SG)_{10,}$ $Au_{18}(SG)_{14}$, $Au_{25}(SG)_{18}$, and $Au_{640}(SG)_{385}$, with the digital photos of the purified gold nanoparticle solutions. As shown in Figure 2.5 a, the solution of $Au_{10-11}(SG)_{10}$ is colorless, which is consistent with the fact that the absorption of $Au_{10-11}(SG)_{10}$ in the visible region is nearly undetectable. Meanwhile, $Au_{10-11}(SG)_{10}$ displays two characteristic peaks at 330 nm and 370 nm. In Figure 2.5 b, $Au_{18}(SG)_{14}$ exhibits two distinct peaks at 560 nm and 620 nm. $Au_{25}(SG)_{18}$ shows two well-defined peaks at 675 nm and 803 nm, and $Au_{640}(SG)_{385}$ displays a broad peak at the position of 400 nm (Figure 2 5 c and d). All these four different-sized gold nanoparticles display

strong absorption in the UV region (< 400 nm), which is also consistent with the black bands in the PAGE results of gold nanoparticles under UV light (Figure 2.1 b).

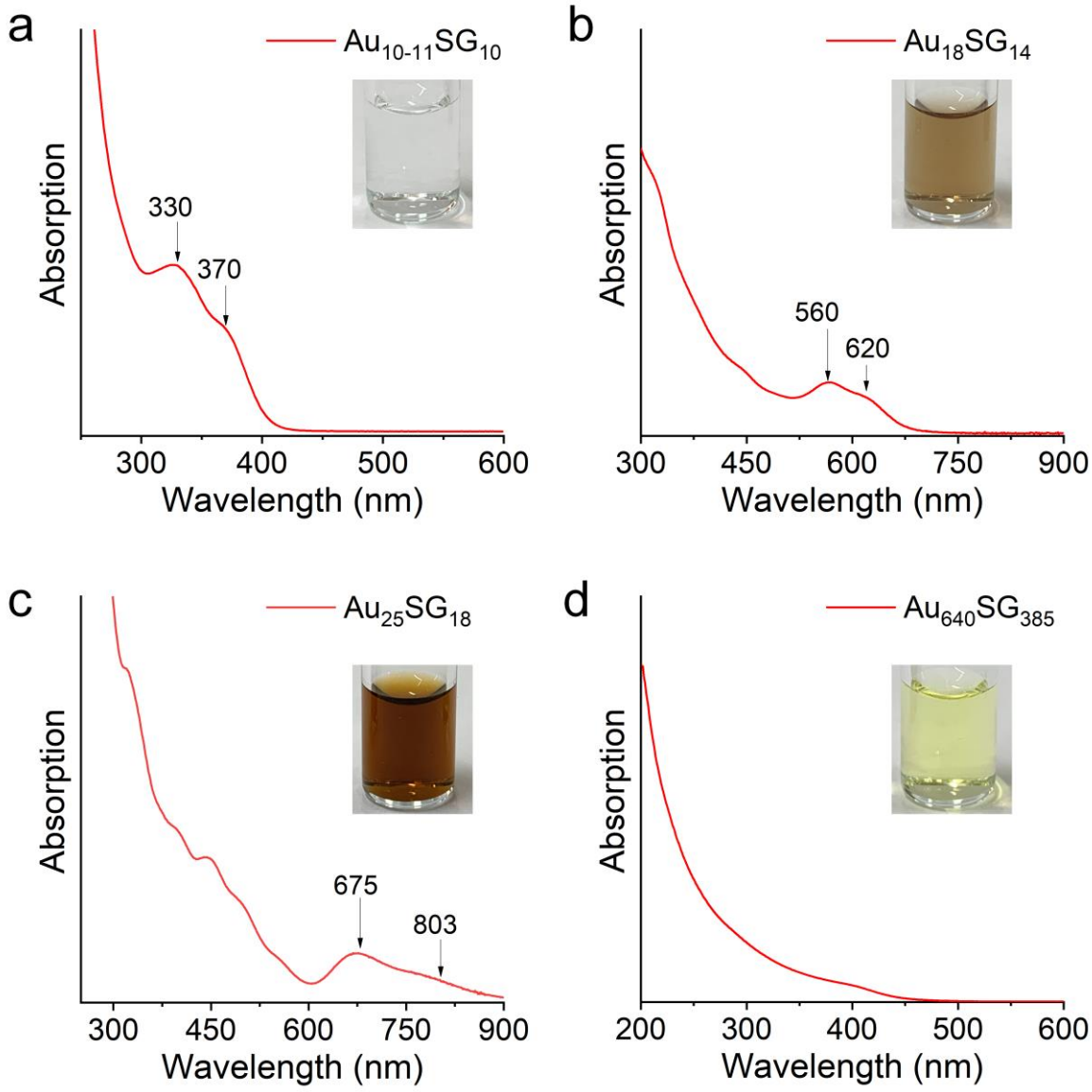

Figure 2.5. The UV-vis absorption spectrum of $Au_{10\text{-}11}(SG)_{10}$, $Au_{18}(SG)_{14}$, $Au_{25}(SG)_{18}$, and $Au_{640}(SG)_{385}$. The insets in a-d show the digital photos of the $Au_{10\text{-}11}(SG)_{10}$, $Au_{18}(SG)_{14}$, $Au_{25}(SG)_{18}$, and $Au_{640}(SG)_{385}$ dissolved in deionized water.

The characteristic peaks of these four different-sized nanoparticles are exactly consistent with the literature reported previously[31, 71], indicating the successful synthesis and high purity of these gold nanoparticles.

Apart from the distinct absorption spectrum, these four different-sized gold nanoparticles also display different fluorescence spectrum (Figure 2.6).

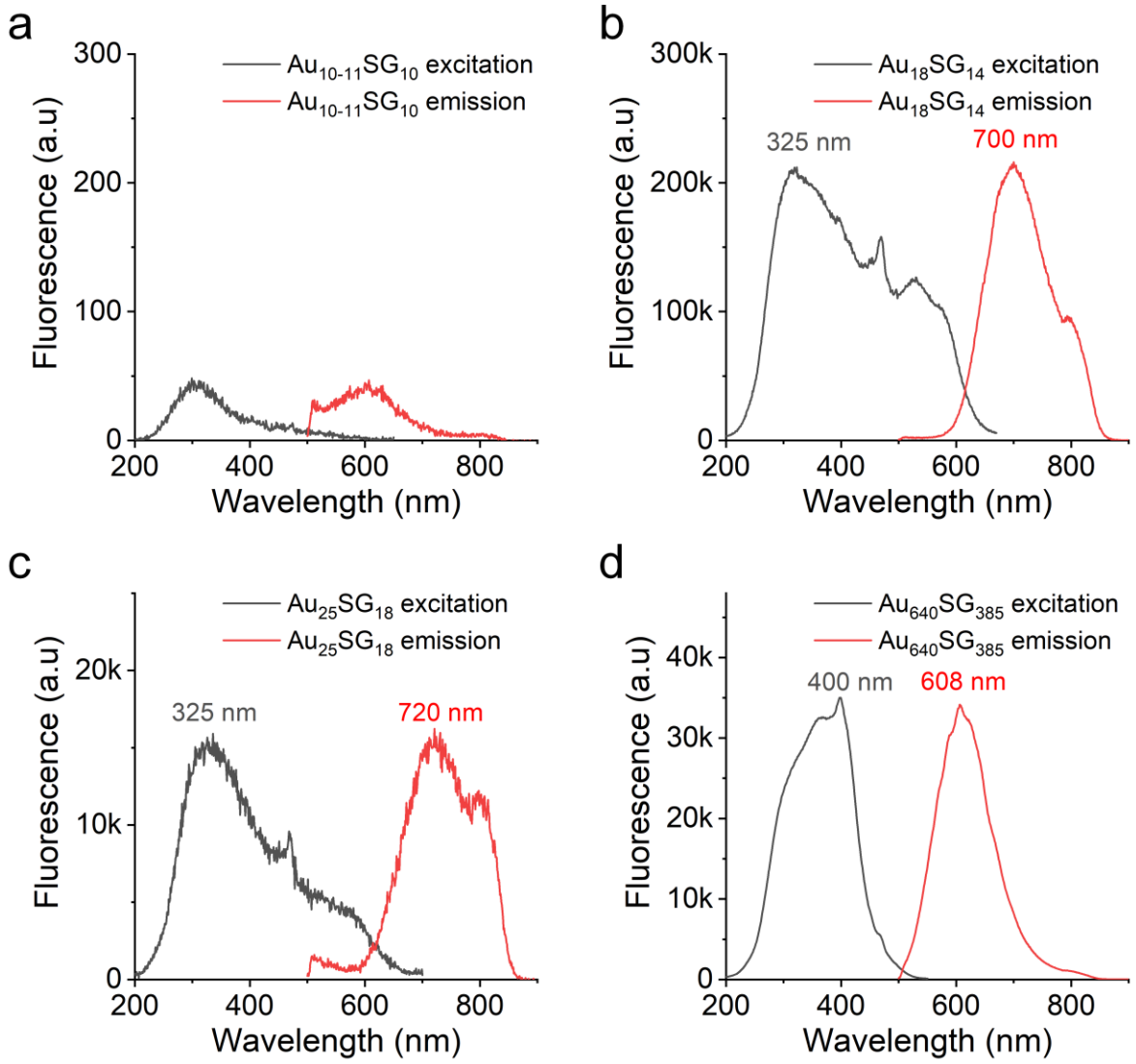

Figure 2.6. The excitation and emission spectra of (a) $Au_{10\text{-}11}(SG)_{10}$, (b) $Au_{18}(SG)_{14}$, (c) $Au_{25}(SG)_{18}$ and (d) $Au_{640}(SG)_{385}$.

As shown in Figure 2.6 a, $Au_{10\text{-}11}(SG)_{10}$ is nearly non-fluorescent compared to the other three gold nanoparticles. In Figure 2.6 b, $Au_{18}(SG)_{14}$ emits strong red fluorescence at the wavelength of 700 nm with the excitation peaks at 325 nm. $Au_{25}(SG)_{18}$ displays a distinct emission peak at

720 nm under the excitation of 325 nm (Figure 2.6 c). As shown in Figure 2.6 d, the emission peak of $Au_{640}(SG)_{385}$ is located at 600 nm while the excitation peak is located at 400 nm. All these excitation and emission spectra are consistent with the previous report[30, 31, 70]. Taken together, the well-defined UV-vis absorption spectra and fluorescence spectra indicate the successful synthesis, as well as the high purity of these four gold nanoparticles. In Table 2.1, the optical properties of different-sized gold nanoparticles are summarized.

Table 2.1. The optical properties of different-sized gold nanoparticles.

	Absorption (nm)	Excitation (nm)	Emission (nm)
$Au_{10\text{-}11}(SG)_{10}$	330/370	306	606
$Au_{18}(SG)_{14}$	560/620	325	700
$Au_{25}(SG)_{18}$	675/803	325	720
$Au_{640}(SG)_{385}$	400	400	600

2.3.1.4 Size characterizations of gold nanoclusters and gold nanoparticles

Thiolated gold nanoparticles $Au_{10\text{-}11}(SG)_{10}$, $Au_{18}(SG)_{14}$, $Au_{25}(SG)_{18}$, and $Au_{640}(SG)_{385}$ are composed of different numbers of gold atoms and GSH molecules, indicating that these four types of gold nanoparticles exhibit different sizes. It has been well documented that different-sized gold nanoclusters can be efficiently separated through electrophoresis due to the different mobility of gold nanoclusters in electrophoresis[73]. The difference in the mobility of gold nanoclusters is fundamentally due to the different sizes and surface charges of gold nanoclusters. In sodium dodecyl sulfate-polyacrylamide gel electrophoresis (SDS-PAGE), it is the

nanoparticle size rather than the surface charge that governs the mobility of the nanoparticle. In SDS-PAGE, smaller-sized nanoparticles display higher mobility than larger ones. As shown in Figure 2.1, four types of gold nanoparticles were separated in SDS-PAGE. It is clear that $Au_{10-11}(SG)_{10}$ exhibits the highest mobility, which followed by $Au_{18}(SG)_{14}$, $Au_{25}(SG)_{18}$, and $Au_{640}(SG)_{385}$, which indicates the size trend of these four nanoparticles: the size of these four gold nanoparticles increases as the gold atom number increases.

Apart from the size trend of these four gold nanoparticles, transmission electron microscopy (TEM) was used to quantify the core size of these four types of gold nanoparticles. As shown in Figure 2.7 a-d, the core size of these four types of gold nanoparticles increases with the increase of the number of gold atoms in the gold nanoparticles. The core size distributions of these four types of gold nanoparticles are quantified in Figure 2.7 e-h, where the blue curves are the results of Gaussian fitting for each gold nanocluster and nanoparticle. As shown in Figure 2.7 e-h, the core size of $Au_{10-11}(SG)_{10,}$ $Au_{18}(SG)_{14}$, $Au_{25}(SG)_{18}$ and $Au_{640}(SG)_{385}$ are 0.80 ± 0.23 nm, 0.95 ± 0.23 nm, 1.22 ± 0.20 nm, and 2.23 ± 0.16 nm, respectively. It is noteworthy that the image contrast of $Au_{10-11}(SG)_{10,}$ $Au_{18}(SG)_{14}$, is relatively low because their sizes are extremely small (within 1 nm) while the current electron microscopes have a resolution of 0.18-0.17 nm due to electron microscopes reach the physical limitations due to the lens aberration and energy width[76]. For $Au_{25}(SG)_{18}$ and $Au_{640}(SG)_{385}$, they can be imaged by electron microscopes with higher contrast than that of $Au_{10-11}(SG)_{10,}$ $Au_{18}(SG)_{14}$, and the TEM results of $Au_{25}(SG)_{18}$ and $Au_{640}(SG)_{385}$ are consistent with the reported work published by other groups[72, 77], and our group previously[7, 10, 30].

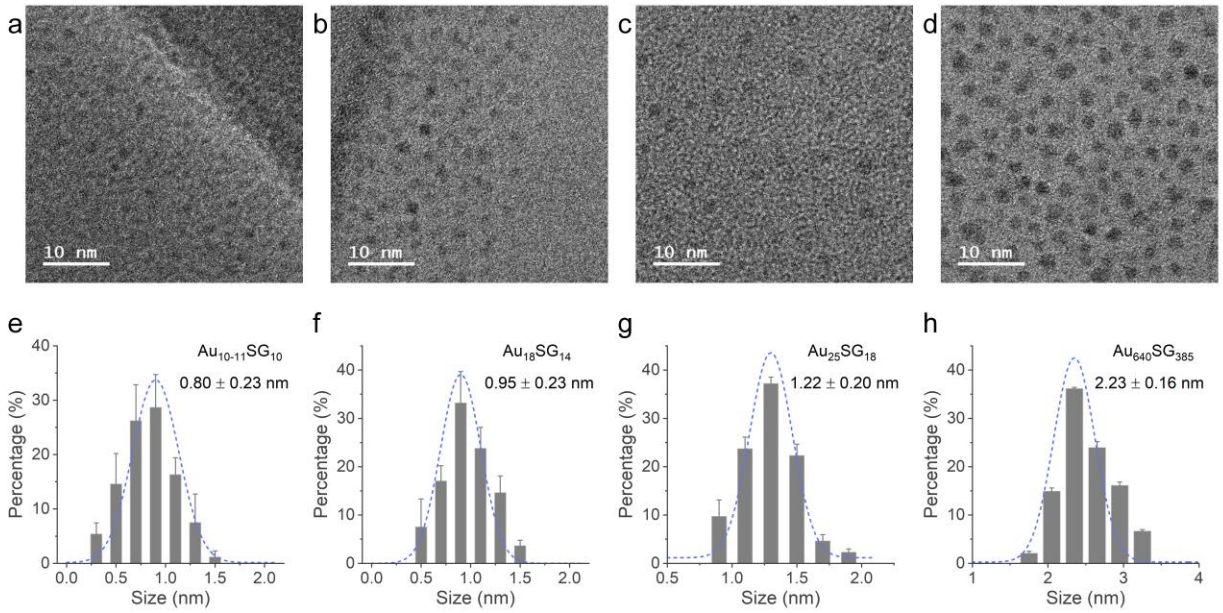

Figure 2.7. Transmission electron microscopy images of $Au_{10\text{-}11}(SG)_{10}$, $Au_{18}(SG)_{14}$, $Au_{25}(SG)_{18}$ and $Au_{640}(SG)_{385}$. The core size of $Au_{10\text{-}11}(SG)_{10}$, $Au_{18}(SG)_{14}$, $Au_{25}(SG)_{18}$ and $Au_{640}(SG)_{385}$ are 0.80 ± 0.23 nm, 0.95 ± 0.23 nm, 1.22 ± 0.20 nm, and 2.23 ± 0.16 nm, respectively. Scale bar: 10 nm.

High-performance liquid chromatography (HPLC) is another powerful technique to quantify the nanoparticle size distribution. A size exclusive column (Superose^{TM} 6 increase 10/300 GL) was chosen for the size comparison of these four gold nanoparticles. The stationary phase (matrix) of this column is a composite of cross-linked agarose and the fractionation range of this column was 5,000 Da to 5,000,000 Da in terms of the molecular weight of globular proteins. The molecular weight of $Au_{10\text{-}11}(SG)_{10}$, $Au_{18}(SG)_{14}$, $Au_{25}(SG)_{18}$, and $Au_{640}(SG)_{385}$ are 5030/5527, 7830, 10433, and 243890 respectively. The molecular weight of our gold nanoclusters and gold nanoparticles are located in the fractionation range of the column (from 5,000 to 5,000,000), indicating this column is suitable for the size separation of our nanoprobes. However, the fractionation range of this column is designed in terms of the molecular weight of a globular

protein not the size of protein. Therefore, we convert the molecular weight of the fractionation range in this column to hydrodynamic diameters. The hydrodynamic diameters (HD) of the protein can be calculated using the following power law fit to literature values[29, 78]: HD = A *MW^B + C * MW^D, where A = -0.000000002614, B = 3.326, C = 0.9482 and D = 0.5001.MW, molecular weight. Therefore, the fractionation range of this column was calculated as about 2.12 nm to 25 nm. The core sizes of our gold nanoclusters and gold nanoparticles are from about 0.80 nm to 2.23 nm (Figure 2.7). With the surface coating of glutathione, the HD of our nanoclusters and nanoparticles would be estimated to increase to about 0.8 nm, based on the previous observations in our group[7]. Therefore, the estimated HD of $Au_{10\text{-}11}(SG)_{10,}$ $Au_{18}(SG)_{14}$, $Au_{25}(SG)_{18}$, and $Au_{640}(SG)_{385}$ would be 1.60 nm, 1.75 nm, 2.02 nm, and 3.03 nm, which is very close to the estimated size fractionation range of this column. Combing these results suggest the "Superose^{TM} 6 increase 10/300 GL" column would be suitable for the separation of our gold nanoclusters and nanoparticles. Theoretically, smaller nanoparticles would display a longer retention time in size-exclusive columns since the smaller nanoparticles would be retarded in the column more easily than larger nanoparticles. As shown in Figure 2.8, the retention time of these four gold nanoparticles decreases as the size of gold nanoparticles increase. For $Au_{10\text{-}11}(SG)_{10,}$ $Au_{18}(SG)_{14}$, $Au_{25}(SG)_{18}$ and $Au_{640}(SG)_{385}$, the retention time is 16.28 ± 0.02 minutes, 16.17 ± 0.03 minutes, 15.72 ± 0.01 minutes, and 15.66 ± 0.03 minutes, respectively. These results also suggest the high purity of these four gold nanoparticles since each nanoparticle only displays one peak. As shown in Figure 2.8 f, there are statistically significant differences in the retention time between the different sized AuNPs, indicating that different sized AuNPs were well purified and could be efficiently separated by the HPLC. In Figure 2.8 g, the correlation between retention

time (quantified by HPLC) and the core size (quantified by TEM) of different-sized AuNPs was plotted. The retention time of AuNPs increases with the increase of the AuNPs core size, which further confirms that the size difference of $Au_{10\text{-}11}(SG)_{10,}$ $Au_{18}(SG)_{14}$, $Au_{25}(SG)_{18}$, and $Au_{640}(SG)_{385}$.

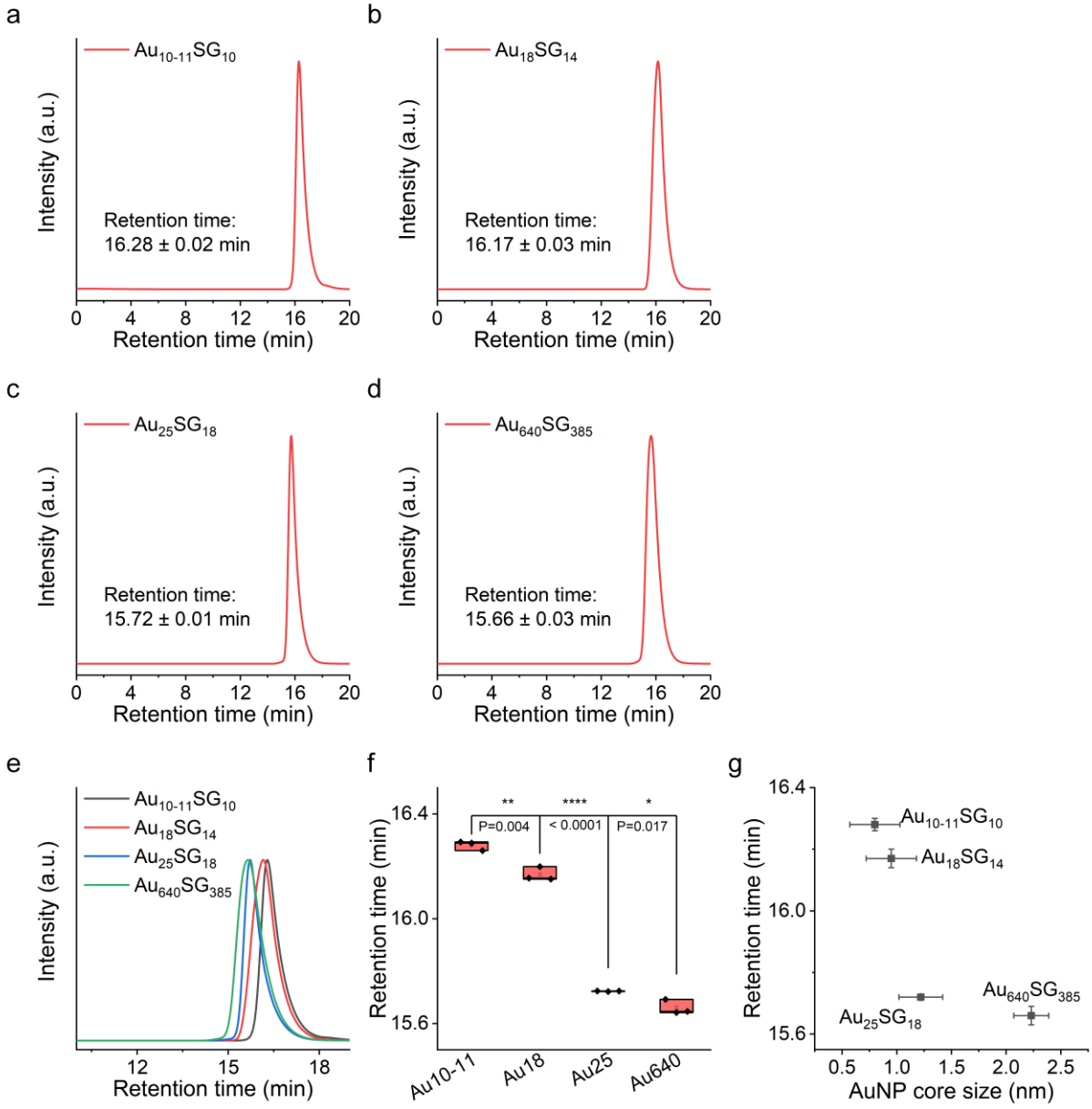

Figure 2.8. Size exclusion chromatography (SEC) of different sized AuNPs. (a) to (d) The SEC of $Au_{10\text{-}11}(SG)_{10}$, $Au_{18}(SG)_{14}$, $Au_{25}(SG)_{18}$ and $Au_{640}(SG)_{385}$. (e) The zoomed-in SEC of different sized AuNPs. (f) The comparison of the retention time between different sized AuNPs. (g) The correlation of the retention time of different sized AuNPs with their core size.

Combing the SDS-PAGE and HPLC results together suggest that the size of these four gold nanoparticles increases with the increase of the number of gold atoms. Meanwhile, the TEM images of $Au_{10-11}(SG)_{10,}$ $Au_{18}(SG)_{14}$, $Au_{25}(SG)_{18}$, and $Au_{640}(SG)_{385}$ suggest that these AuNPs are ultrasmall (sub-10 nm) and monodispersed.

2.3.2 Conjugation of the organic dye on gold nanoparticles

2.3.2.1 Synthesis and purification of the ICG conjugated gold nanoparticles

The synthesis method of ICG conjugated $Au_{25}(SG)_{18}$ (ICG-Au25) was developed by Dr. Xingya Jiang in our lab and this method has been reported previously[9, 10]. To synthesis the different sized ICG conjugated AuNPs: ICG-Au11, ICG-Au18, and ICG-Au640, the synthesis and purification method was modified as described below:

For the synthesis of ICG conjugated $Au_{10-11}(SG)_{10}$ (ICG-Au11), 1.5 mg $Au_{10-11}(SG)_{10}$ (0.3 μmole) were dissolved in 1 mL deionized water. Then, a certain amount of 10 M NaOH solution was added to the solution of $Au_{10-11}(SG)_{10}$ to adjust the pH to around 8. After that, 0.5 mg Indocyanine green NHS active ester (ICG-NHS) (0.6 mmol) was dissolved in 1 mL DMSO. This ICG-NHS solution was added into the $Au_{10-11}(SG)_{10}$. The mixture was then vortexed for 16 hours. To purify the as-synthesized ICG-Au11, the unreacted ICG-NHS and unreacted $Au_{10-11}(SG)_{10}$ need to be removed. First, 1 mL of reaction solution was diluted two times with water and then purified using a Sephadex LH-20 column to remove unconjugated ICG-NHS. Then, 30 k Da Ultra centrifugal filters were used to remove the unconjugated $Au_{10-11}(SG)_{10}$ since the unconjugated $Au_{10-11}(SG)_{10}$ would pass out of the 30 K Da filter while the ICG-Au11 would not. The centrifugal filtration can be stopped once no $Au_{10-11}(SG)_{10}$ is observed in the filtrate (no

$Au_{10\text{-}11}(SG)_{10}$ absorption (peak 330nm/370nm) could be observed). The purified ICG-Au11 was then redissolved in deionized water and can be freeze-dried for future usage.

The synthesis of ICG conjugated $Au_{18}(SG)_{14}$ (ICG-Au18), $Au_{25}(SG)_{18}$ (ICG-Au25) and $Au_{640}(SG)_{385}$ (ICG-Au640) is similar to that of ICG-Au11 except for the concentration of ICG-NHS and gold nanoparticles are different. Briefly, the concentration of ICG-NHS dissolved in DMSO for the synthesis of ICG-Au18, ICG-Au25, and ICG-Au640 was 0.8 mg/mL, 1 mg/mL, and 0.8 mg/mL, respectively. While the concentration of $Au_{18}(SG)_{14}$, $Au_{25}(SG)_{18}$ and $Au_{640}(SG)_{385}$ was 1.8 mg/mL, 1.5 mg/mL, and 4.2 mg/mL, respectively. The purification method of ICG-Au18, ICG-Au25, and ICG-Au640 was also composed of removing the unreacted ICG-NHS and removing the unconjugated gold nanoparticles. To remove the unreacted ICG-NHS in ICG-Au18, ICG-Au25, and ICG-Au640, 100 µL of saturated sodium chloride solution and 2 mL ethanol were added into 1 mL of reaction solution of ICG-Au18, ICG-Au25, and ICG-Au640, respectively. Then, the mixture was centrifugated at 4500 rpm for 10 minutes. The unconjugated ICG-NHS was dissolved in the supernatant and was disposed of while the unconjugated gold nanoparticles and ICG conjugated gold nanoparticles (ICG-AuNPs) were precipitated together. Next, the precipitate was resuspended in 1X PBS Phosphate-buffered saline for the removal of free unconjugated gold nanoparticles. The removal of unconjugated gold nanoparticles of ICG-Au18, ICG-Au25, and ICG-Au640 is the same as that of ICG-Au11. The purified ICG-Au18, ICG-Au25, and ICG-Au640 samples were then redissolved in deionized water, lyophilized, and stored in -20 ºC for future use. For detailed information on the synthesis and purification method of different-sized ICG-AuNPs, please see section 2.5.2.

2.3.2.2 Optical properties of the ICG conjugated gold nanoparticles

As shown in Figure 2.9 b, the characteristic absorption peak of ICG is located at 780 nm. After the conjugation of ICG on the gold nanoparticle surface, the absorption of ICG-Au11, ICG-Au18, ICG-Au25, and ICG-Au640 were bule-shifted from 780 nm to 703 nm, 683 nm, 706 nm, and 697 nm, (Figure 2.9 c-f). Such a blue shift was the result of H aggregation of ICG molecules on the surface of gold nanoparticles.

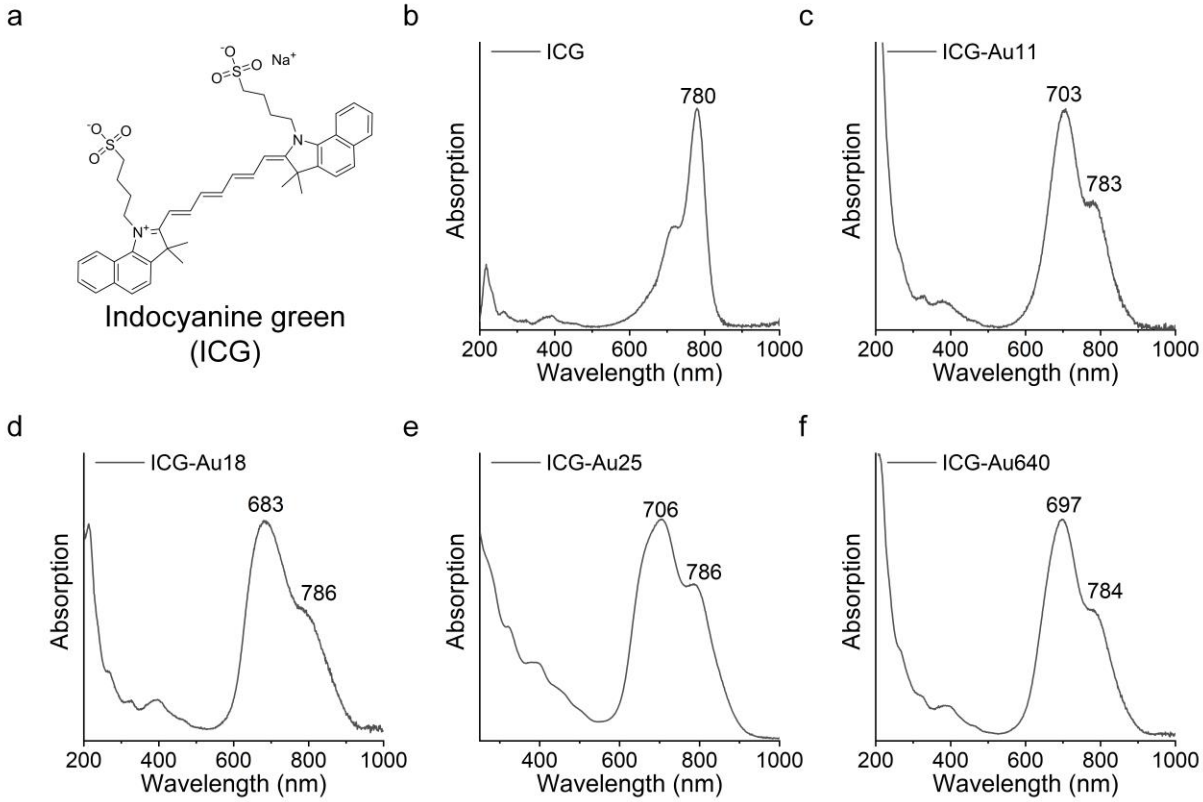

Figure 2.9. The UV-vis absorption spectrum of ICG and ICG conjugated gold nanoparticles. (a) molecular structure of ICG. b-f, absorption spectrum of (b) ICG, (c) ICG-Au11, (d) ICG-Au18, (e) ICG-Au25, and (f) ICG-Au640.

Interestingly, the blue shift of different-sized gold nanoparticles was different. As shown in Table 2.2, ICG-Au18 displays the largest blue shift of 97 nm, which is followed by ICG-Au640

(83 nm), ICG-Au11 (77 nm), and ICG-Au25 (74 nm). The largest blue shift of ICG-Au18 among these four different sized ICG conjugated gold nanoparticles indicates the strongest H coupling effect of multiple ICG molecules on the surface of $Au_{18}(SG)_{14}$. We hypothesized that the ICG density on the surface of $Au_{18}(SG)_{14}$ is the highest compared to the other three ICG-AuNPs, which results in the highest attraction between ICG molecules on the $Au_{18}(SG)_{14}$ surface, and therefore causes the highest absorption blue shift. In section 2.3.2.3, the average ICG numbers on these four types of nanoparticles were quantitatively analyzed.

Table 2.2. The blue shift of ICG absorption peaks after the conjugation on the surface of different-sized gold nanoparticles.

	Blue shift (nm)
$Au_{10\text{-}11}(SG)_{10}$	77
$Au_{18}(SG)_{14}$	97
$Au_{25}(SG)_{18}$	74
$Au_{640}(SG)_{385}$	83

ICG is a near-infrared emitting dye with the excitation at around 780 nm and the emission at 810 nm (Figure 2.10). When ICG was conjugated on the surface of the gold nanoparticle, the ICG fluorescence was nearly completely quenched due to the electron transfer process between ICG and gold nanoparticles.[10] The quenching efficiency of ICG-Au11, ICG-Au18, ICG-Au25, and ICG-Au640 was 99.19%, 99.41%, 99.17%, and 98.65%, respectively. However, when the ICG molecule conjugated on the gold nanoparticle surface was replaced (etched) by the

environmental thiols like GSH, the fluorescence of ICG instantaneously recovered, as shown in Figure 2.11. The fluorescence of ICG-AuNPs was enhanced around 100-fold after the ICG molecules of ICG-AuNPs were replaced by external thiols. As shown in Table 2.3, the fluorescence enhancement of ICG-Au11, ICG-Au18, ICG-Au25, and ICG-Au640 was 124-fold, 170-fold, 120-fold, and 74-fold respectively. Among these four ICG-AuNPs, the fluorescence enhancement, as well as the quenching efficiency of ICG-Au18, was the largest one. Our hypothesis of this phenomenon is the density of the ICG molecules on the $Au_{18}(SG)_{14}$ surface are the highest among these four nanoparticles, which leads to the strongest H coupling effect of ICG on the surface of $Au_{18}(SG)_{14}$ and therefore the strongest self-quenching of ICG fluorescence in ICG-Au18. The average ICG molecule numbers were quantitatively analyzed in section 2.3.2.3.

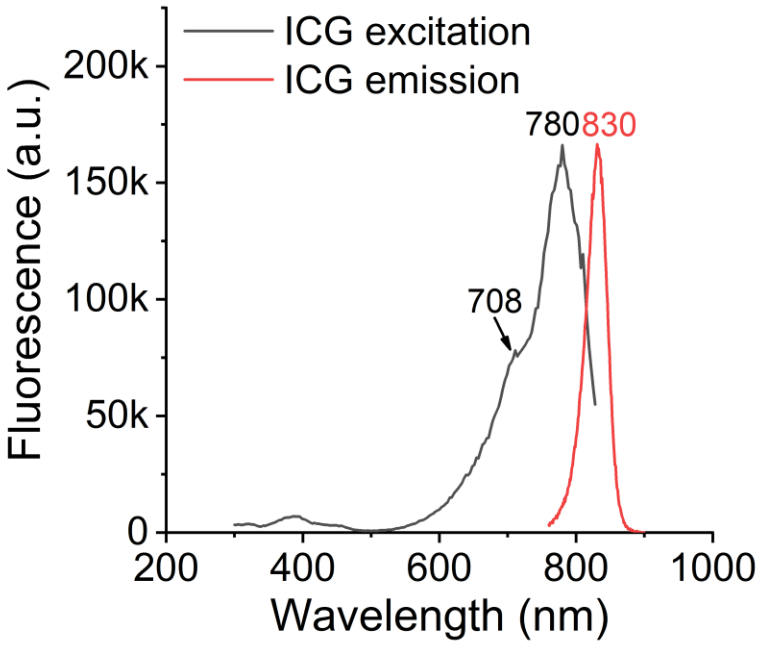

Figure 2.10. The excitation and emission spectra of ICG. Solvent: Pure water. Excitation/Emission: 780 nm/830 nm.

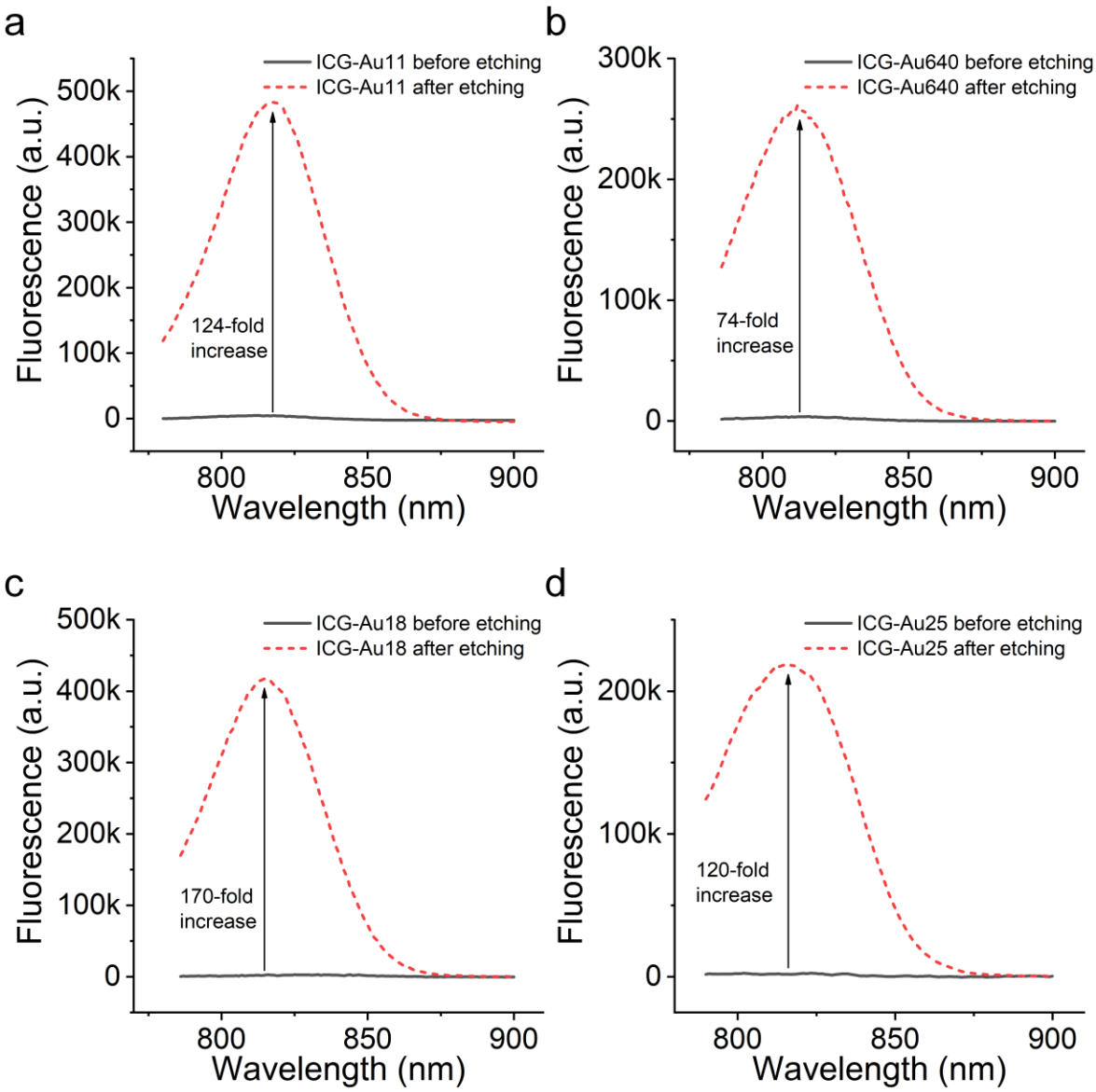

Figure 2.11. The emission spectrum of ICG-AuNPs before and after the surface ICG were replaced (etched) by the environmental thiols.

Table 2.3. The fluorescence enhancement and quenching efficiency of ICG-AuNPs before and after the surface ICG were replaced (etched) by the environmental thiols.

	Fluorescence enhancement	Quenching efficiency
$Au_{10\text{-}11}(SG)_{10}$	124-fold	99.19%
$Au_{18}(SG)_{14}$	170-fold	99.41%
$Au_{25}(SG)_{18}$	120-fold	99.17%
$Au_{640}(SG)_{385}$	74-fold	98.65%

2.3.2.3 Quantification of the ICG numbers on the surface of gold nanoparticles

When ICG was conjugated on the surface of the AuNPs, the absorption peak of ICG was blue shifted and the fluorescence of ICG was nearly completely quenched. As shown in Table 2.2 and Table 2.3, different-sized ICG-AuNPs display different blue shifts and fluorescence quenching efficiencies. We hypothesized that such differences result from the different densities of ICG molecules on the surface of different-sized ICG-AuNPs. To prove this, the number of ICG molecules on the surface of different-sized ICG-AuNPs needs to be quantified. The amount of AuNPs and the number of ICG on the surface need to be quantified separately to calculate the average ICG molecules on the surface of AuNPs. Figure 2.12 represents the method to quantify the number of ICG molecules on the surface of AuNPs.

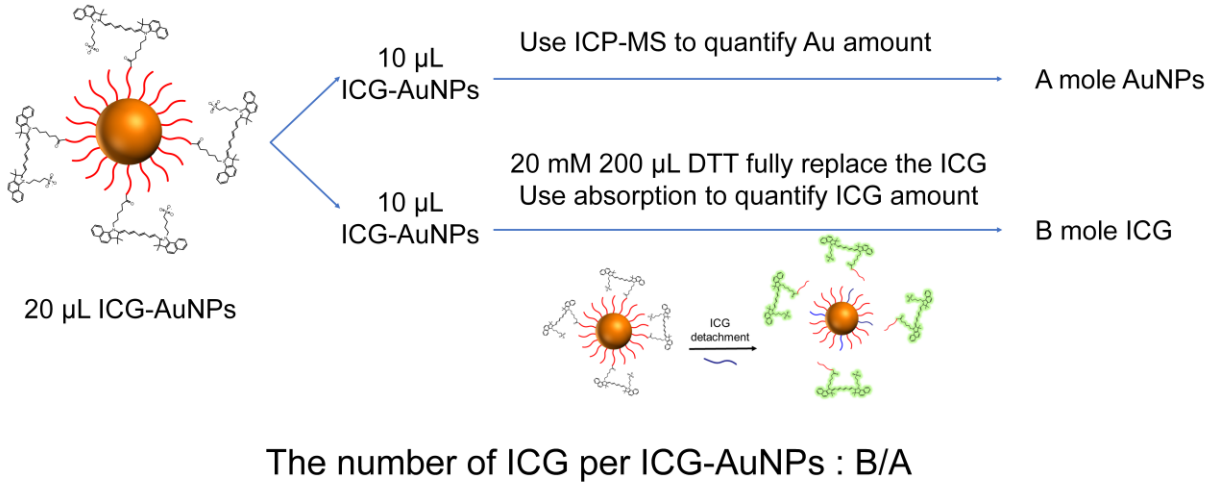

Figure 2.12. Schematic of quantification of the number of ICG molecules on the AuNPs surface.

Briefly, 20 μL purified ICG-AuNPs were split into two samples A and B with equal volume (10 μL). Sample A was used for the quantification of the amount of Au and sample B was used for the quantification of the amount of ICG. Sample A was digested using aqua regia, and the amount of Au was measured by ICP-MS. For sample B, the dithiothreitol (DTT) was used to fully replace (etch) the ICG molecules on the surface of the AuNPs (Figure 2.13). Then, the ICG amount was quantified by the absorption of ICG at 780 nm using the ICG absorption standard curve as a reference (Figure 2.14). The average number of ICG per AuNPs was calculated by dividing the amount of ICG by the amount of AuNPs.

As shown in Figure 2.12 and Figure 2.13, DTT was used to fully etch the ICG molecules off the surface of AuNPs and the characteristic peaks of ICG-AuNPs were all red shifted back to 780 nm. After that, the ICG amount can be quantified by using the ICG absorption standard curve as

a reference (Figure 2.14). The establishment of the ICG absorption standard curve was discussed in section 2.5.2 methods.

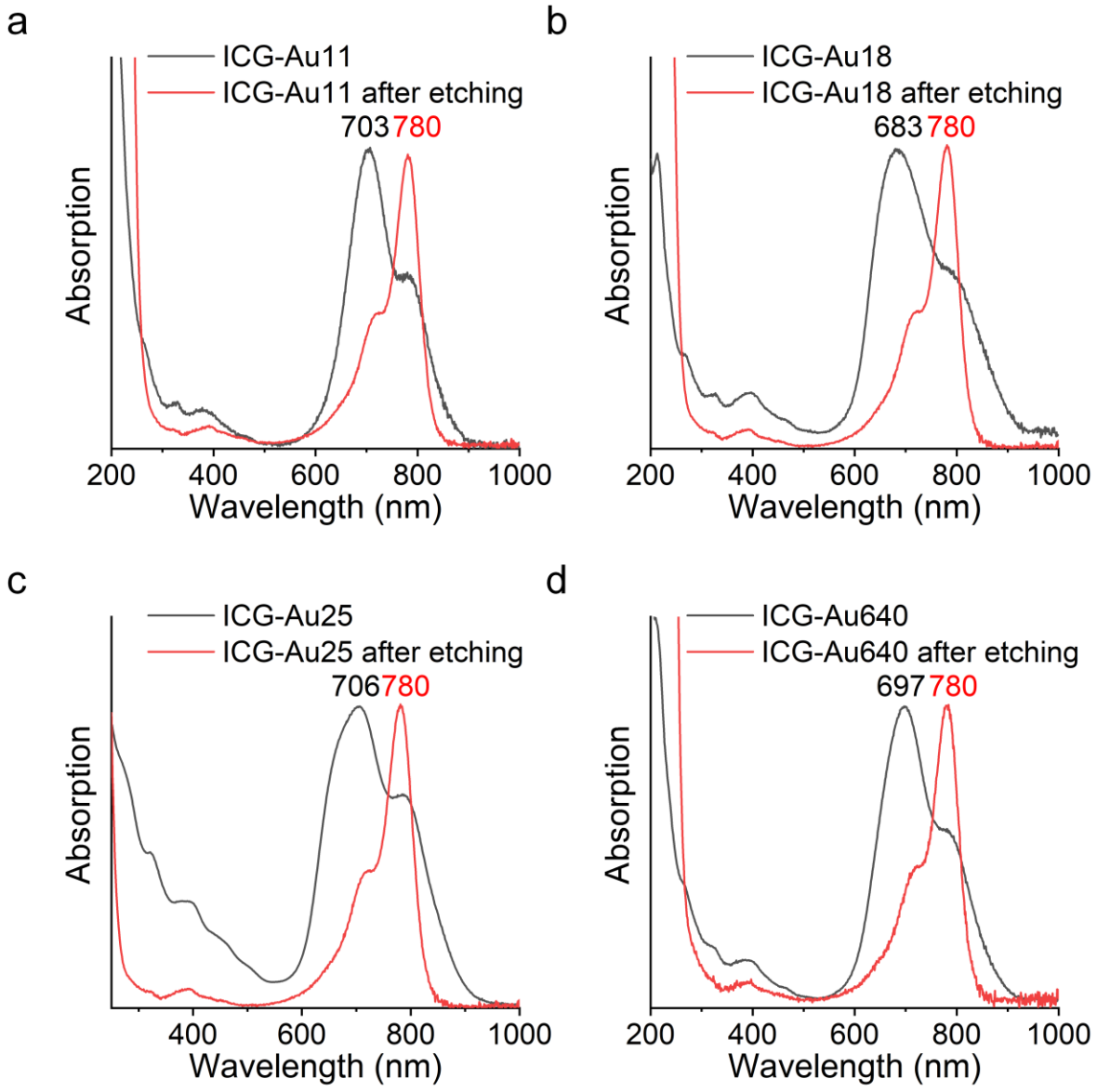

Figure 2.13. The absorption spectrum of different-sized ICG-AuNPs before and after being etched by the thiols.

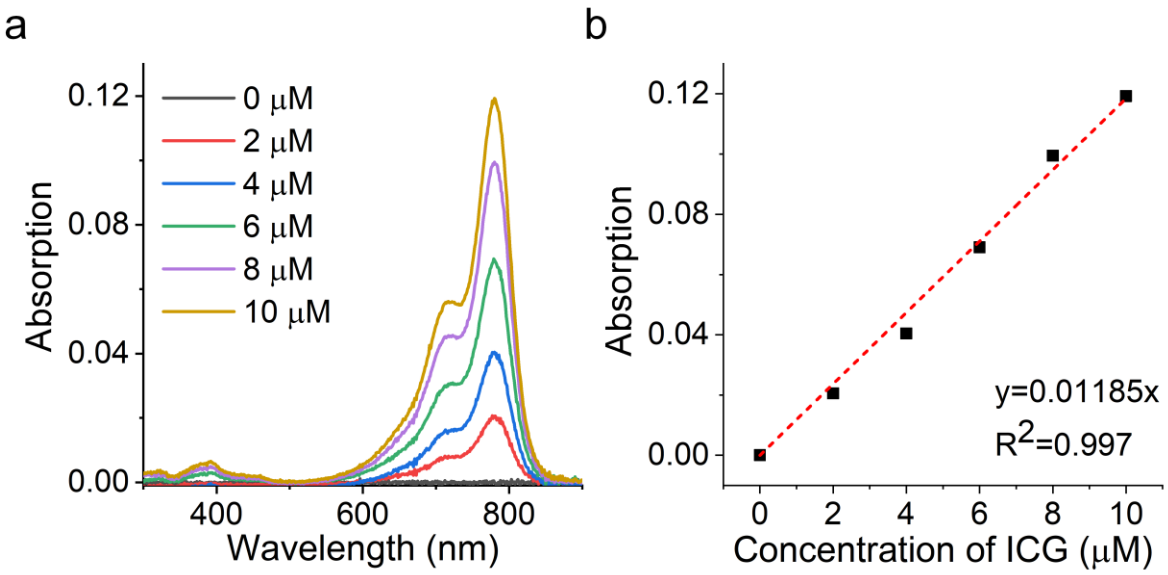

Figure 2.14. The ICG absorption standard curve. (a) The absorption spectrum of ICG with the concentration ranging from 0 to 10 μM. (b) The ICG absorption standard curve at the wavelength of 780 nm.

After the quantification of the amount of ICG molecules, the gold amount of different-sized ICG-AuNPs was quantified by ICP-MS. Then, the number of ICG molecules can be calculated by dividing the ICG amount by the Au amount. As shown in Table 2.4, the ICG number per AuNPs of ICG-Au11, ICG-Au18, ICG-Au25, and ICG-Au640 were 2.43 ± 0.04, 3.13 ± 0.1, 4.26 ± 0.06, and 10.84 ± 0.30.

Table 2.4. The average number of ICG per AuNPs.

	Number of ICG per AuNP
ICG-Au11	2.43 ± 0.04
ICG-Au18	3.13 ± 0.12
ICG-Au25	4.26 ± 0.06
ICG-Au640	10.84 ± 0.30

2.3.3 Quantification of the nanoparticle-biothiol interactions *in vitro*

Biothiols, such as GSH, Cysteine (Cys), and homocysteine (Hcy), play significant roles in multiple physiological processes, such as the regulation of the cellular redox homeostasis, the metabolism of nutrients, and the detoxification of the xenobiotics.[66] Meanwhile, in our recent work,[10] biothiols like GSH and Cys are involved in the biotransformation process of engineered nanoparticles, and the interactions between the biothiols and nanoparticles can significantly alter the *in vivo* fate of nanoparticles. Therefore, it is crucial to fundamentally understand which factor governs the interaction between the biothiols and nanoparticles. According to our recent findings[10], we hypothesis that the size of the nanoparticle, the species of the biothiol, and the protein-binding are three factors that are related to the interactions between the biothiols and nanoparticles. To verify these hypotheses *in vivo*, we investigated the nanoparticle-biothiol interactions *in vitro*.

2.3.3.1 The effect of nanoparticle size on the nanoparticle-biothiol interactions in vitro

To investigate the effect of nanoparticle size on the nanoparticle-biothiol interactions, ICG conjugated AuNPs: ICG-Au11, ICG-Au18, ICG-Au25, and ICG-Au640 were chosen due to their similar structure with different sizes. The size of the Au core of these four nanoparticles was quantified by TEM, (see section 2.3.1.4 Figure 2.7). The core size of these four nanoparticles is 0.80 ± 0.23 nm, 0.95 ± 0.23 nm, 1.22 ± 0.20 nm, and 2.23 ± 0.16 nm, respectively, which increases with the increase of Au atom numbers. After the conjugation of ICG on the surface of the gold nanoparticles, the fluorescence of ICG was nearly completely quenched, which is a fluorescence "off" state. Once these ICG-AuNPs reacted with thiols, the fluorescence of ICG-AuNPs is immediately recovered, which is the fluorescence "on" state. Due to such unique fluorescence "on-off" properties of ICG-AuNPs, the fluorescence change of different-sized ICG-AuNPs can be used to monitor the interactions between different-sized ICG-AuNPs and biothiols. To investigate the effect of nanoparticle size on the nanoparticle-biothiol interactions *in vitro*, the amount of ICG in different-sized ICG-AuNPs was quantified and kept the same. The methods of quantification of ICG amount in different-sized ICG-AuNPs were discussed in section 2.3.2.3. The ICG amount of ICG-Au11, ICG-Au18, ICG-Au25, and ICG-Au640 were the same (20 μM) for this experiment. Then, 10 μL different-sized ICG-AuNPs with the ICG amount of 20 μM were reacted with 190 μL PBS containing 1mM GSH respectively. The fluorescence of each ICG-AuNPs was instantly monitored over time using the plate reader.

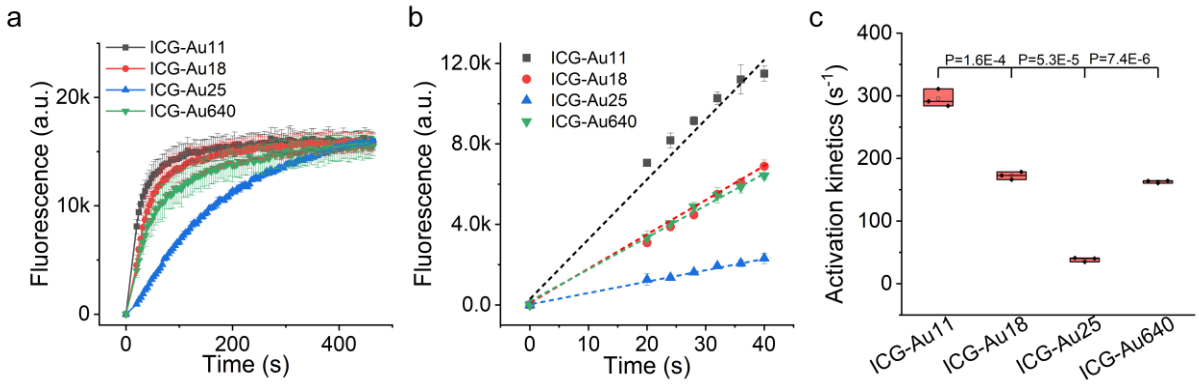

Figure 2.15. The interaction between different-sized ICG-AuNPs and GSH. (a) the time-dependent fluorescence intensity curve of ICG-AuNPs after being reacted with GSH. (b) the time-dependent fluorescence intensity curve of ICG-AuNPs after being reacted with GSH within the 40s. (c) the calculated activation kinetics of different-sized ICG-AuNPs.

As shown in Figure 2.15 a, after being reacted with GSH, the fluorescence of ICG-Au11, ICG-Au18, ICG-Au25, and ICG-Au640 was activated rapidly during the first 40s. Then, the fluorescence of ICG-Au11, ICG-Au18, ICG-Au25, and ICG-Au640 gradually reached a plateau. In Figure 2.15 b, the fluorescence enhancement of ICG-Au11, ICG-Au18, ICG-Au25, and ICG-Au640 at the first 40s was zoomed in. The fluorescence intensity of ICG-Au11, ICG-Au18, ICG-Au25, and ICG-Au640 was linear related to the reaction time with GSH. Due to the amount of ICG of different-sized ICG-AuNPs being consistent before the reaction between the ICG-AuNPs and GSH, the slope of the fluorescence enhancement curve in Figure 2.15 b reflects the activation kinetics of different-sized ICG-AuNPs being reacted with GSH. These activation kinetics of ICG-Au11, ICG-Au18, ICG-Au25, and ICG-Au640 were calculated and summarized in Figure 2.15 c. The activation kinetics of ICG-Au11, ICG-Au18, ICG-Au25, and ICG-Au640 being reacted with GSH was 295.36 ± 14.11 s^{-1}, 172.52 ± 6.28 s^{-1}, 38.73 ± 3.38 s^{-1}, and 163.01 ± 2.21 s^{-1}, respectively. Such activation kinetics are size-dependent in that from ICG-Au11 to ICG-

Au25 the activation kinetics decrease as the size of nanoparticles increases, while from ICG-Au25 to ICG-Au640 the activation kinetics increase as the size of nanoparticles increase. The reaction activity between GSH and different-sized ICG-AuNPs is size-dependent: Generally, the reaction activity decreases with the increase of nanoparticle size, while ICG-Au25 is the exception that the reaction activity of ICG-Au25 is lowest, although the size of ICG-Au25 is not the largest. The phenomenon that the reaction activity of smaller sized ICG-AuNPs is higher than larger sized ICG-AuNPs is consistent with our group findings[10], where the reaction activity of smaller sized ICG conjugated PEGylated AuNPs is higher than larger sized ones in the size range of 5 to 100 nm. The reaction activity of ICG-Au640 (163.01 ± 2.21 s^{-1}) was lower than that of ICG-Au18 (172.52 ± 6.28 s^{-1}) (with no statistic difference) although the size of Au640 (2.23 ± 0.16 nm) is larger than Au18 (0.95 ± 0.23 nm). It is noteworthy that Au18 is atomically precise nanocluster with a much narrower size distribution when compared to that of Au640. The reaction activity of ICG-AuNPs reflects the interaction between Au and sulfur atoms in the form of the Au-S bond. Therefore, the similarity of the reaction activity between ICG-Au18 and ICG-Au640 indicates that the strength of the average Au-S bond in ICG-Au640 is similar to that in ICG-Au18.

2.3.3.2 The effect of thiol species on the nanoparticle-biothiol interactions in vitro

In section 2.3.3.1, we showed the size of ICG-AuNPs could affect the reaction activity between the nanoparticle and GSH. It is unknown whether the size trend could be also observed when ICG-AuNPs react with other types of thiols? Meanwhile, it is also unknown whether the thiol species would affect the reaction activity of the interactions between different-sized ICG-AuNPs

and thiols. As cysteine is another biothiols that is involved in the biotransformation of the nanoparticle *in vivo*, we not only investigated the reaction activity of ICG-AuNPs with GSH, but also investigated the reaction activity of ICG-AuNPs with Cysteine, and a GSH/Cys mixture. The concentration of cysteine was 1 mM, the same as the concentration of GSH. The GSH/Cys mixture was made by dissolving 0.5 mmol GSH and 0.5 mmol Cysteine in 1 L PBS so that the concentration of the total thiols is also 1 mM.

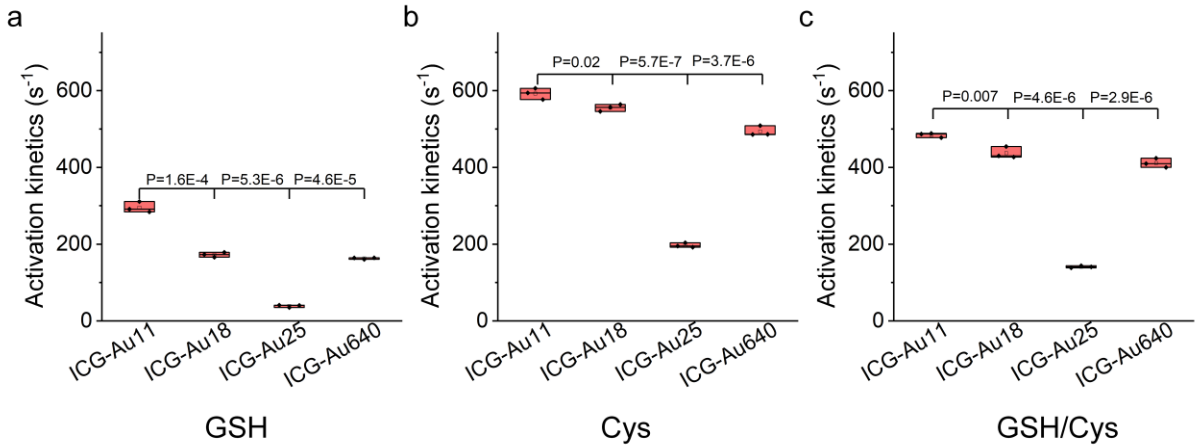

Figure 2.16. The reaction activity of ICG-AuNPs with different thiols. (a) The reaction between ICG-AuNPs with 1 mM GSH. (b) The reaction between ICG-AuNPs with 1 mM Cys. (c) The reaction between ICG-AuNPs with 1 mM GSH/Cys.

As shown in Figure 2.16, the reaction activity of different-sized ICG-AuNPs with GSH, Cys, and a GSH/Cys mixture was quantified. In Figure 2.16 b, the reaction activity of ICG-Au11, ICG-Au18, ICG-Au25, and ICG-Au640 with Cysteine was 592.29 ± 14.70 s^{-1}, 555.61 ± 9.16 s^{-1}, 196.82 ± 5.95 s^{-1}, and 493.56 ± 13.17 s^{-1}, respectively. In Figure 2.16 c, the reaction activity of ICG-Au11, ICG-Au18, ICG-Au25, and ICG-Au640 with GSH/Cys was 484.34 ± 5.99 s^{-1}, 437.12 ± 14.99 s^{-1}, 140.95 ± 2.73 s^{-1}, and 411.26 ± 12.05 s^{-1}, respectively. Similar to the reaction with GSH, the reaction activity of ICG-AuNPs with Cysteine or GSH/Cys mixture are also size-

dependent. From ICG-Au11 to ICG-Au25, the reaction reactivity of Cysteine or GSH/Cys mixture decreases with the increase of the size of ICG-AuNPs. From ICG-Au25 to ICG-Au640, the reaction reactivity of Cysteine or GSH/Cys mixture increase with the increase of the size of ICG-AuNPs. Interestingly, the reaction activity of ICG-AuNPs with Cysteine is larger than GSH/Cys and GSH for each ICG-AuNPs, which means that Cysteine can more easily replace the ICG on the surface of ICG-AuNPs compared to GSH and a GSH/Cys mixture.

2.3.3.3 The effect of protein binding on the nanoparticle-biothiol interactions in vitro

In the section 2.3.3.1 and 2.3.3.2, we systematically investigated the reaction activity between different-sized ICG-AuNPs and different species of thiols. All these reactions were performed in PBS solution, which means no protein was involved in these reactions. When the engineered nanoparticles are transported *in vivo*, proteins play a crucial role in the interactions between nanoparticles and biochemicals. Meanwhile, it was well documented that ICG displays strong protein binding after being administrated *in vivo*. Therefore, the protein binding cannot be ignored for the investigation of nanoparticle-biochemical interactions. To mimic the biological environment, fetal bovine serum (FBS) was chosen as the solvent and the experiments in sections 2.3.3.1 and 2.3.3.2 were repeated with the change of replacing the PBS solution with FBS.

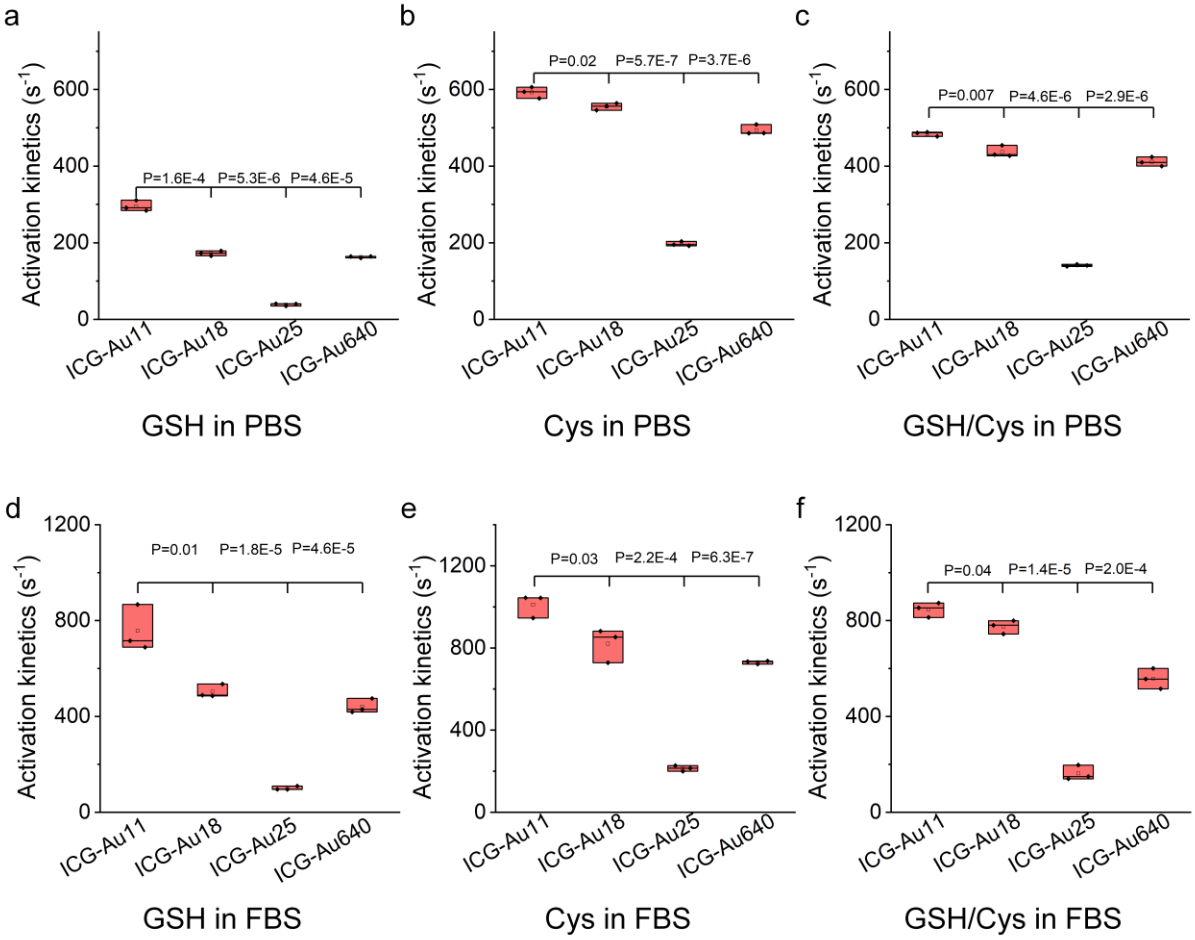

Figure 2.17. The reaction activity of ICG-AuNPs with different thiols in PBS and FBS. a-c, The reaction activity of different-sized ICG-AuNPs with (a) GSH, (b) Cys, and (c) GSH/Cys mixture in PBS. d-f, The reaction activity of different-sized ICG-AuNPs with (d) GSH, (e) Cys, and (f) GSH/Cys mixture in FBS.

As shown in Figure 2.17, the reaction activity of ICG-AuNPs with different thiols in PBS (a-c) and FBS (d-f) were quantified. The effect of nanoparticle size and the effect of thiol species on the reaction activity was also observed in FBS. In FBS, the smaller-sized ICG-AuNPs react more easily with thiols except for ICG-Au25, which reacts with thiols least efficiently. Like in PBS, cysteine in FBS also displays the most reaction activity with ICG-AuNPs, which is followed by the GSH/Cys mixture and GSH. It is noteworthy that the reaction reactivity of ICG-AuNPs with

thiols in FBS is higher than the same condition in PBS. We hypothesis that the proteins in FBS which bind to ICG molecules on the surface of AuNPs can weaken the Au–S bond, making ICG more easily released from the AuNPs in the presence of external thiols.

As shown in Figure 2.18, 3D diagrams were plotted to compare the reaction rate of all these situations. The 3D graph reflects the relationship among reaction rate, size of ICG-AuNCs, thiol types, and the effect of protein binding. We find three trends here. The first trend is size. The reaction rate of ICG-AuNPs first deceases as the Au atom number increased from ICG-Au11 to ICG-Au25, then the reaction rate increase as the gold atom number increased. Second, the reaction rate of all four NPs increases when the thiol type changes from GSH to GSH/Cys mixture to Cys, suggesting that cysteine will more easily react with ICG-AuNPs compared to GSH. Third, the presence of the protein accelerates the reaction between the ICG-AuNPs and thiols.

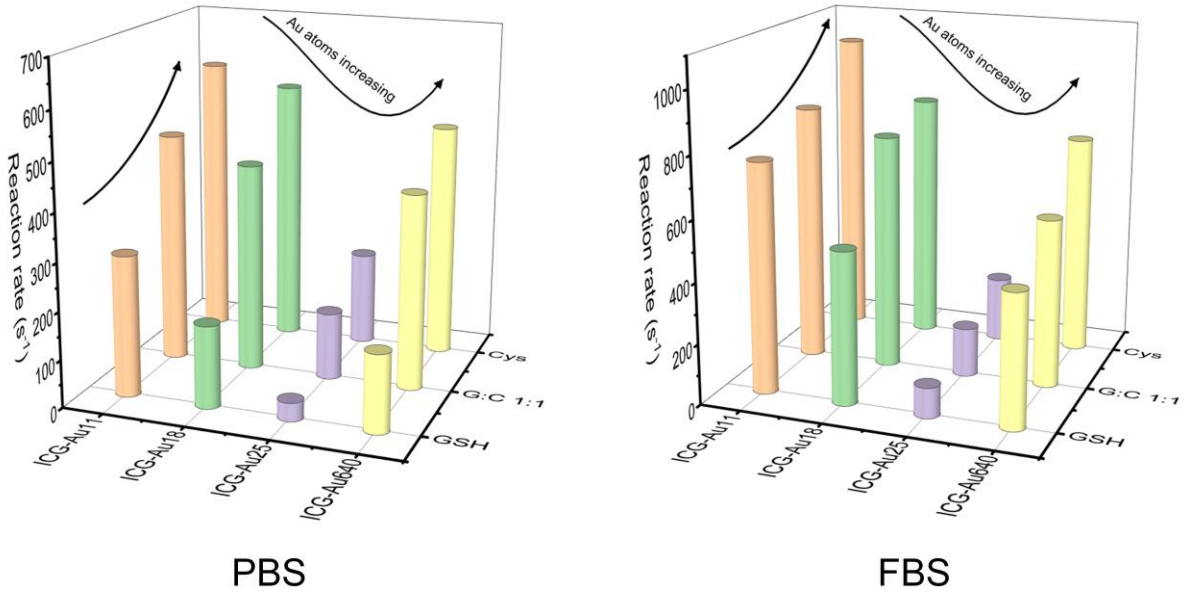

Figure 2.18. The 3D diagrams of the relationship among the activation kinetics, the size of ICG-AuNPs, and the thiols species in (a) PBS and (b) FBS.

According to the Arrhenius equation, the relationship between the reaction rate and the activation energy are listed as below[79]:

$V = dc/dt = KC^n$ (1)

$K = Ae^{(-E/RT)}$ (2)

In the case of the reaction between the ICG-AuNPs with thiols, c is the concentration of the product, which is the amount of detached ICG. K is the rate constant, which has been quantified and compared in Figure 2.16. t is the reaction time; n is the reaction order, E is the activation energy, T is the reaction temperature, R and A are the constants.

To compare the activation of different-sized ICG-AuNPs with thiols, equation (2) can be applied as below. Here we use the reaction of ICG-Au11 and ICG-Au25 with glutathione in PBS as an example:

$K_{(ICG\text{-}Au11,\ GSH,\ PBS)}$ is the reaction rate constant of the reaction between the ICG-Au11 and glutathione in PBS; $K_{(ICG\text{-}Au25,\ GSH,\ PBS)}$ is the reaction rate constant of the reaction between the ICG-Au25 and glutathione in PBS; $E_{(ICG\text{-}Au11,\ GSH,\ PBS)}$ is the activation energy of the reaction between the ICG-Au11 and glutathione in PBS; $E_{(ICG\text{-}Au25,\ GSH,\ PBS)}$ is the activation energy constant of the reaction between the ICG-Au25 and glutathione in PBS.

$$K_{(ICG\text{-}Au11,\ GSH,\ PBS)} = Ae^{(-E(ICG\text{-}Au11,\ GSH,\ PBS)/RT)} \quad (3)$$

$$K_{(ICG\text{-}Au25,\ GSH,\ PBS)} = Ae^{(-E(ICG\text{-}Au25,\ GSH,\ PBS)/RT)} \quad (4)$$

$$K_{(ICG\text{-}Au11,\ GSH,\ PBS)}/K_{(ICG\text{-}Au25,\ GSH,\ PBS)} = Ae^{(-E(ICG\text{-}Au11,\ GSH,\ PBS)/RT)}/Ae^{(-E(ICG\text{-}Au25,\ GSH,\ PBS)/RT)}$$

$$= e^{(-E(ICG\text{-}Au11,\ GSH,\ PBS)/RT)-\ (-E(ICG\text{-}Au11,\ GSH,\ PBS)/RT)}$$

$$= e^{([E(ICG\text{-}Au11,\ GSH,\ PBS)-\ E(ICG\text{-}Au25,\ GSH,\ PBS)]/RT)} \quad (5)$$

Therefore:

$$E_{(ICG\text{-}Au11,\ GSH,\ PBS)} - E_{(ICG\text{-}Au25,\ GSH,\ PBS)} = \ln [K_{(ICG\text{-}Au11,\ GSH,\ PBS)}/K_{(ICG\text{-}Au25,\ GSH,\ PBS)}] \quad (6)$$

According to equation (6), we compare the activation energy of different-sized ICG-AuNPs reacted with thiols in PBS and FBS in Figure 2.19. As shown in Figure 2.19 a-c, the activation energy of different-sized ICG-AuNPs reacted with glutathione, cystine, and glutathione/cysteine mixture in PBS are summarized. In Figure 2.19 e-f, the activation energy of different-sized ICG-AuNPs reacted with glutathione, cystine, and glutathione/cysteine mixture in FBS are compared. In Figure 2.18 a, for the reaction between ICG-AuNPs with glutathione in PBS, the activation energy of ICG-Au25 was the highest, followed by ICG-Au640, ICG-Au18, and ICG-Au11. The activation energy of ICG-Au25 is 3.56 KJ/mol, 3.70 kJ/mol, and 5.03 KJ/mol higher than that of ICG-Au640, ICG-Au18, and ICG-Au11. As for the reaction between ICG-AuNPs with thiols at

other conditions, the size-dependency could also be observed and the size-dependency was similar, where the activation energy of ICG-Au25 was the highest one followed by ICG-Au640, ICG-Au18, and ICG-Au11.

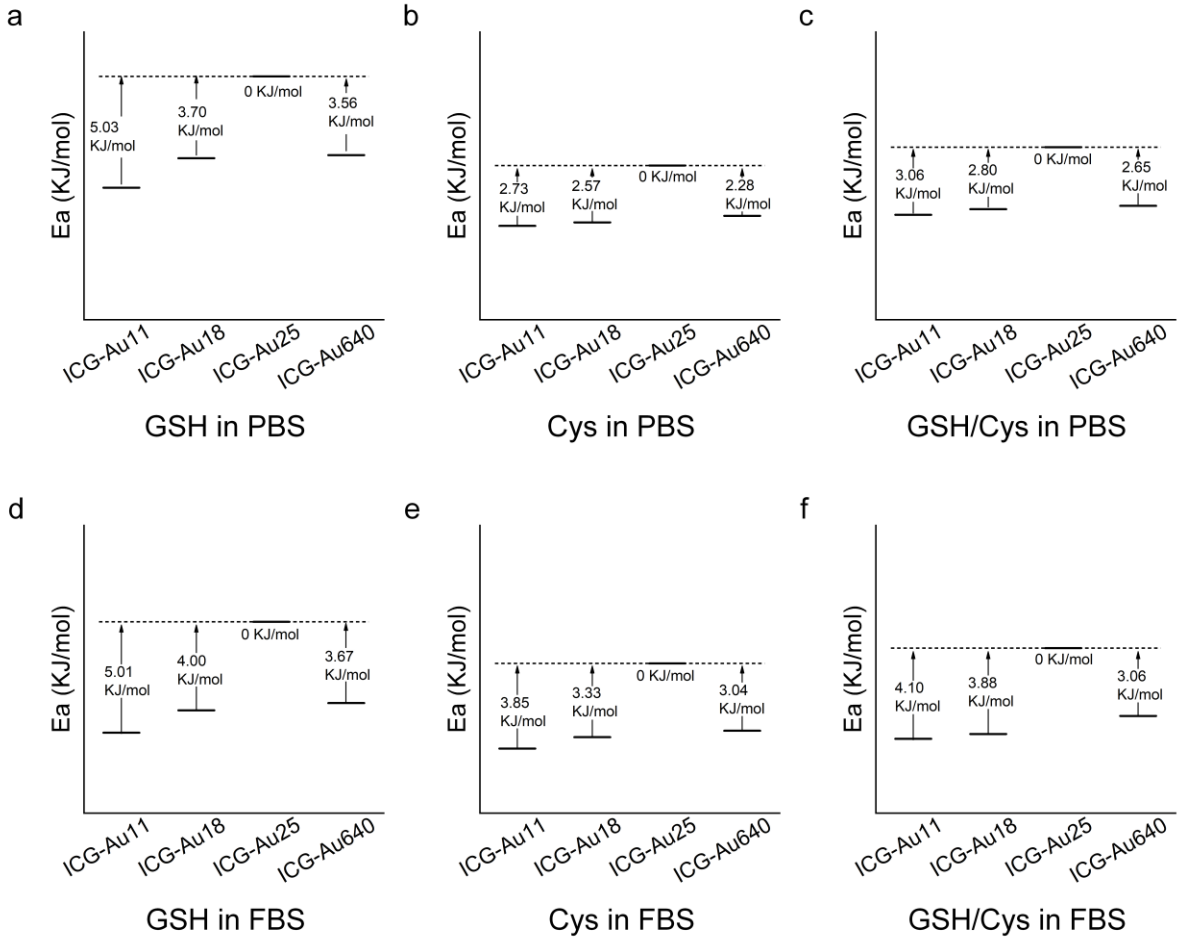

Figure 2.19. The activation energy of different-sized ICG-AuNPs reacting with thiols in PBS and FBS. a-c, The activation energy of different-sized ICG-AuNPs with (a) GSH, (b) Cys, and (c) GSH/Cys mixture in PBS. d-f, The activation energy of different-sized ICG-AuNPs with (d) GSH, (e) Cys, and (f) GSH/Cys mixture in FBS.

2.4 Conclusion

In Chapter 2, the interactions between ICG-AuNPs and biothiols *in vitro* were systematically investigated. In the section 2.3.1 and 2.3.2, the preparation and characterization of ICG-AuNPs were illustrated in detail. In these two sections, the synthesis and purification methods of different sized AuNPs and ICG conjugated AuNPs were summarized step by step. The as-prepared AuNPs and ICG conjugated AuNPs were highly purified. Then, the optical properties and the size of AuNPs and ICG conjugated AuNPs were carefully characterized and compared. After that, the average ICG number on different-sized ICG-AuNPs was quantified. Based on the systematic characterizations of ICG-AuNPs, the interactions between ICG-AuNPs and biothiols *in vitro* could be quantitatively analyzed. In section 2.3.3, the interaction between different-sized ICG-AuNPs and different thiols was investigated. The effect of protein binding was also studied. Combining all the results, three conclusions were drawn. First, the interactions of ICG-AuNPs and biothiols depend on the size of nanoparticles. The smaller ICG-AuNPs react with thiols more easily and efficiently compared to the larger-sized nanoparticles, except for ICG-Au25. The reaction activity of ICG-Au25 with thiols is the least efficient one, which is probably due to the structure of Au25, making Au25 highly stable and highly resistant against thiol etching[80]. Second, the interactions of ICG-AuNPs and biothiols depend on the species of thiol. The cysteine and GSH, which are the two main biothiols involved in multiple biological processes, displayed different reaction activities with ICG-AuNPs. Compared to GSH, cysteine reacts with the ICG-AuNPs more easily and efficiently, which is probably due to the size of cysteine being smaller than GSH, making cysteine reach the Au-S bond on the surface of ICG-AuNPs and replace the ICG-GSH more easily than GSH. Third, the protein binding facilitates the reaction

between the ICG-AuNPs and biothiols, which may result from the fact that the protein binding weakens the Au-S bond on the surface of ICG-AuNPs, making the ICG-GSH conjugates on the surface of ICG-AuNPs more easily replaced by the external biothiols. After that, the activation energy of the reaction between the ICG-AuNPs and different thiols was quantitatively compared. All these *in vitro* results provide a foundation for the investigation of the interactions between engineered nanoparticles and biochemicals *in vivo*, which will be discussed in the following chapter.

2.5 Experiment

2.5.1 Materials and equipment

ICG-NHS was obtained from AdipoGen Life Science, Inc. Fetal Bovine Serum (FBS) was purchased from Corning, Inc. All the other chemicals were purchased from Sigma-Aldrich and used as received without further purification. Ultra-centrifuge filter units with the molecular weight cut-off (MWCO) of 3k, 10k, and 30k Da (MilliporeSigma™ Amicon™) were utilized for the purification of gold nanoparticles and ICG conjugated gold nanoparticles. The amount of gold was measured using an Agilent 7900 inductively coupled plasma mass spectrometer (ICP-MS). The pH was measured by an Accumet AB15 pH meter and an Accuphast microprobe electrode. The gel electrophoresis results were obtained with a Mini PROTEAN Tetra Cell (Bio-Rad Laboratories, Inc. USA). Agarose gel electrophoresis was carried out in a Bio-Rad Mini-Sub Cell GT system (Bio-Rad Laboratories, Inc. USA). Nuclear magnetic resonance (NMR) spectra were obtained with Bruker 600 MHz NMR spectrometer The absorption spectra were collected with a Virian 50 Bio UV-vis spectrophotometer. The luminescence spectra of different-sized

nanoparticles were detected with a PTI QuantaMasterTM 30 Fluorescence Spectrophotometer (Birmingham, NJ). The ESI-MS results were collected with Xevo G2-XS QT of Quadrupole Time-of-Flight Mass Spectrometer. Transmission electron microscopy (TEM) images of AuNPs were obtained using a 200kV Jeol 2100 transmission electron microscope. A Shimadzu Prominence Modular HPLC equipped with UV-Vis detector (SPD-20A) and fluorescence detector (RF-20A) was used for the measurements of the size of nanoparticles. The time-dependent fluorescence enhancement of ICG-AuNPs was monitored using a the BioTek Synergy H4 plate reader.

2.5.2 Methods

Synthesis of glutathione-coated different sized gold nanoparticles (AuNPs)

Atomically precise gold nanoclusters: $Au_{10\text{-}11}(SG)_{10,}$ $Au_{18}(SG)_{14}$, and $Au_{25}(SG)_{18}$ were synthesized according to the previously reported method with modifications[67-69]. The 2 nm gold nanoparticle: $Au_{640}(SG)385$ were synthesized following the method reported by our group previously[30]. For the synthesis of $Au_{10\text{-}11}(SG)_{10}$, the $HAuCl_4{\cdot}3H_2O$ stock solution (1 M) was prepared in deionized water and was stored at 4 ºC before use. The Glutathione (460.98 mg, 1.5 mmol) was dissolved in 80 mL deionized water in a 250 mL flask. Under mild stirring (~800 rpm), a 500 µL 1 M $HAuCl_4{\cdot}3H_2O$ stock solution was added into the glutathione solution. The solution was stirred mildly for about 5 minutes until the white precipitate formed. Then, a certain amount of 10 M NaOH was introduced to the reaction solution to alter the pH to around 4.8. The reaction solution was transparent when the pH was changed to 4.8. After that, the reducing agent $NaBH_3CN$ (40 mL, 1.25 mM) was added, and the reaction solution was kept at ambient temperature without stirring. After the 12 h reaction, the as-synthesized $Au_{10\text{-}11}(SG)_{10}$ was

collected and was purified by dialysis to remove the unreacted gold salt, GSH, and reducing agent. The purified $Au_{10-11}(SG)_{10}$ can be freeze-dried and stored at 4 ºC for future use.

The preparation of $Au_{18}(SG)_{14}$ is listed as follows: 0.138 g GSH (0.45 mmol) was dissolved in 24 mL deionized water. Under mild stirring (~800 rpm), 150 µL 1 M $HAuCl_4 \cdot 3H_2O$ stock solution was introduced. Then, the pH of the reaction solution was adjusted to 4.8~5.0 by adding a certain amount of 10 M NaOH. After that, 3 mL 0.2 mM TBAB (borane *tert*-butylamine complex) was added, and the reaction solution was stirred at 800 rpm at 40 ºC for about 1 hour. The reaction was stopped when the fluorescence of the mixture did not increase anymore. To purify the $Au_{18}(SG)_{14}$, the reaction solution was first cooled to room temperature. Then, for every 20 mL of reaction solution, 2 mL saturated sodium chloride solution and 20 mL ethanol were added and mixed well. The mixture was centrifuged for 5 minutes at 4000 rpm to remove the unreacted gold salt, GSH, and reducing agent. After that, the supernatant was disposed of, and the precipitate was resolved in 5 mL deionized water. The purified $Au_{18}(SG)_{14}$ can be freeze-dried and stored at 4 ºC for future use.

The synthesis method of $Au_{25}(SG)_{18}$ was similar to that of $Au_{18}(SG)_{14}$, with an additional size-focusing step. To synthesize $Au_{25}(SG)_{18}$, the $HAuCl_4 \cdot 3H_2O$ stock solution (1 M) was prepared as mentioned before in the synthesis method of $Au_{18}(SG)_{14}$. Then, 0.7683 g GSH (2.5 mmol) was dissolved in 80 mL deionized water in a tri-neck flask. 500 µL $HAuCl_4 \cdot 3H_2O$ stock solution was then introduced into the tri-neck flask and the reaction solution was stirred for 15 min. Then, 40 mL 0.2 M TBAB solution was added into the flask and the reaction solution was kept stirring for another 2 minutes. After that, the solution was allowed to react for 16 hours without stirring at 40

ºC. The as-synthesized $Au_{25}(SG)_{18}$ was purified by the same method as $Au_{18}(SG)_{14}$. The purified $Au_{25}(SG)_{18}$ can be freeze-dried and stored at 4 ºC for future use.

To synthesis the 2 nm gold nanoparticle $Au_{640}(SG)_{385}$, 36.8 mg GSH (0.12 mmol) was first dissolved in 5 mL deionized water, then 125 µL 1 M NaOH was introduced to adjust the pH of GSH solution to 7~8. Then, 300 µL 0.3 M TCEP was added to the GSH solution and incubated at room temperature for 30 minutes. After that, the GSH solution was added into a 250-mL glass flask containing 45 mL deionized water. Under vigorous stirring, 150 µL 1 M $HAuCl_4 \cdot 3H_2O$ stock solution was added, and the reaction solution was stirred at 95 ºC. After 2 hours of reaction, the products were collected and the unreacted chemicals, such as GSH, gold salt, and TCEP, need to be removed for purification. To purify the as-synthesized $Au_{640}(SG)_{385}$ solution, a certain amount of 1 M NaOH was introduced, and the pH of $Au_{640}(SG)_{385}$ solution was adjusted to around 3~4. Then, ethanol with the equivalent amount of the $Au_{640}(SG)_{385}$ solution was added, and the solution was mixed well. The mixture was precipitated at 4500 rpm for 10 minutes. The supernatant was disposed of after precipitation while the precipitates were redissolved in deionized water. The purified $Au_{640}(SG)_{385}$ can be freeze-dried and stored at 4 ºC for future use.

Characterization of glutathione-coated different sized gold nanoparticles (AuNPs)

The glutathione-coated different-sized gold nanoparticles were characterized concerning their purity, chemical compositions, optical properties, and size.

The purity of different-sized gold nanoparticles was characterized by sodium dodecyl sulfate-polyacrylamide gel electrophoresis (SDS-PAGE). The PAGE experiments were conducted with a Mini PROTEAN Tetra Cell (Bio-Rad Laboratories, Inc. USA). The separating and stacking

gels were prepared using acrylamide with the contents of 30 and 3 wt% (acrylamide/bis-(acrylamide) = 94:6), respectively. The eluting buffer was 1 x Tris-glycine-SDS (TGS) running buffer which contains 25 mM Tris, 192 mM glycine, and 0.1% SDS. The pH of the eluting buffer was about 8.6. The as-purified different sized AuNPs were dissolved in a 10% (v/v) glycerol/water solution (20 μL) at a concentration of 3 mg/mL, respectively. The samples were then loaded into the lanes of the stacking gel and eluted for 2 h at a constant voltage mode (100 V). After 2 hours of eluting, the bright field imaging, as well as the fluorescence image of the gel, was obtained under visible light and UV light.

The chemical compositions were characterized by NMR and ESI-Mass spectroscopy. NMR spectra were acquired with Bruker 600 MHz NMR spectrometer. The purified AuNPs, as well as the free glutathione molecule, were dissolved in Deuterium oxide (D_2O) at a concentration of 6 mg/mL.

The ESI-Mass spectroscopy was carried out with Xevo G2-XS QT Quadrupole Time-of-Flight Mass Spectrometer. The purified $Au_{10\text{-}11}(SG)_{10,}$ $Au_{18}(SG)_{14}$, and $Au_{25}(SG)_{18}$ were first dissolved in pure water at a concentration of 0.4 mg/mL, respectively. Then, the samples were diluted twice by adding the same amount of methanol. Therefore, the final concentration of $Au_{10\text{-}11}(SG)_{10,}$ $Au_{18}(SG)_{14}$, and $Au_{25}(SG)_{18}$ for the ESI-Mass measurement were 0.2 mg/mL respectively, and the solvent of the samples was 50% (v/v) water/methanol system. The sample solution was infused directly into the source at 10 μL/min through the syringe pump. All data were collected in the negative ion mode over the range of 500−2400 m/z. The source block temperature was set at 80 ºC and the desolvation temperature was set at 600 ºC. The cone gas

flow was set as 25 L/h and the desolvation gas was set to 1000 L/hr. The sample cone voltage was set as 39 V and the electrospray capillary voltage was set as 1.48 kV.

The optical properties were acquired using a Virian 50 Bio UV-vis spectrophotometer and a PTI QuantaMasterTM 30 Fluorescence Spectrophotometer, where the absorption spectra and fluorescence spectra of AuNPs were measured in pure water.

The size of AuNPs was quantified by transmission electron microscopy (TEM) and High-performance liquid chromatography (HPLC). The AuNPs were dissolved in pure water and deposited on 400 mesh copper grids for the TEM imaging. HPLC was conducted on a Superose-6 10/300 GL column (Amersham Biosciences) using PBS, pH 7.4 as the mobile phase. The flow rate was 1 mL/min.

Synthesis of ICG conjugated gold nanoparticles (ICG-AuNPs)

Our former group member Dr. Xingya Jiang developed a method to synthesize ICG-Au25 and this method has been reported previously[9, 10]. Briefly, 4 mg ICG-NHS was dissolved in 4 mL DMSO and was covered with aluminum foil to avoid light exposure. 6 mg $Au_{25}(SG)_{18}$ was dissolved in 4 mL DI water and the pH was changed to 8 by adding a certain amount of 1 M NaOH. Then, the ICG-NHS DMSO solution was added into the aqueous solution of $Au_{25}(SG)_{18}$, and the mixture was vortexed for over 16 hours. To purify the ICG-Au25, 0.8 mL saturated NaCl solution and 16 mL ethanol were added to the 8 mL as-synthesized ICG-Au25 solution. The mixture was then centrifugated at 4500 rpm for 10 minutes. The precipitate was redissolved in 1X PBS and purified by 30 k Da Ultra centrifugal filters to remove the unconjugated $Au_{25}(SG)_{18}$. The as-purified ICG-Au25 was redissolved in pure water and was lyophilized for future use.

The synthesis and purification of ICG-Au18 and ICG-Au640 were similar to that of ICG-Au25 with the modifications of the amount of ICG-NHS and AuNPs. For ICG-Au18, 0.8 mg ICG-NHS was dissolved in 1 mL DMSO and was then reacted with 1 mL aqueous solutions of $Au_{18}(SG)_{14}$ with the concentration of 1.8 mg/mL (pH=8) for more than 16 hours. For the synthesis of ICG-Au640, 1 mL 0.8 mg/mL ICG-NHS solution (dissolved in DMSO) was reacted with 1 mL aqueous solution of $Au_{640}(SG)_{385}$ with the concentration of 4.2 mg/mL (pH=8) and vortexed for over 16 hours. The purification process of ICG-Au18 and ICG-Au640 was the same as that of ICG-Au25 by removing the unconjugated ICG-NHS as well as the unconjugated AuNPs.

The synthesis method of ICG-Au11 is similar to ICG-Au25 while the purification of ICG-Au11 is different from that of ICG-Au25. For the synthesis of ICG-Au11, 1 mL 0.4 mg/mL ICG-NHS solutions (dissolved in DMSO) was reacted with 1 mL aqueous solution of $Au_{10\text{-}11}(SG)_{10}$ with the concentration of 1.5 mg/mL (pH=8), and the reaction was allowed to vortex for more than 16 hours. To purify the ICG-Au11, a size exclusive Sephadex LH-20 column was utilized to remove the unconjugated ICG-NHS. First, the as-synthesized solution of ICG-Au11 was diluted twice with pure water. Then, this diluted ICG-Au11 solution was eluted in the Sephadex LH-20 column using 1X PBS as the eluting solution. The unconjugated ICG-NHS was removed due to the lower mobility in the Sephadex LH-20 column compared to ICG-Au11. Then, the unconjugated $Au_{10\text{-}11}(SG)_{10}$ was removed using 30 k Da Ultra centrifugal filters. The purified ICG-Au11 was then redissolved in pure water and was lyophilized for future use.

Quantification of the average number of ICG molecules on the surface of ICG-AuNPs

The average number of ICG molecules on the surface of ICG-AuNPs equals the amount of ICG molecules divided by the amount of AuNPs. The amount of ICG was quantified by its characteristic absorption peak at 780 nm with a pre-established standard curve. The amount of AuNPs was quantified by ICG-MS analysis after the digestion using aqua regia. Briefly, 10 µL purified ICG-AuNPs were digested by the aqua regia, and the amount of Au was measured using ICP-MS. After that, 10 µL purified ICG-AuNPs with the same concentration of ICG-AuNPs were incubated with 190 µL 20 mM dithiothreitol (DTT) for 30 minutes to completely release the ICG molecules from the surface of AuNPs. Then the ICG concentration was quantified by its absorption peaks at 780 nm according to the established standard curve (see Figure 2.13).

Quantification of the nanoparticle-biothiol interactions in vitro

The nanoparticle-biothiol interactions *in vitro* were performed by monitoring the fluorescence enhancement kinetics of ICG-AuNPs after the reaction between different-sized ICG-AuNPs with different thiols in either PBS solution or 50% v/v PBS/FBS solution. The amount of ICG on different-sized ICG-AuNPs was controlled to be consistent (20 µM ICG in 10 µL aqueous solutions of ICG-AuNPs) for each experiment. To investigate the effect of nanoparticle size on the nanoparticle-biothiol interactions *in vitro*, 10 µL aqueous solutions of different-sized ICG-AuNPs were reacted with 190 µl PBS containing 1mM GSH. The fluorescence of different-sized ICG-AuNPs was instantaneously monitored over time using the plate reader. To investigate the effect of thiol species on the nanoparticle-biothiol interactions *in vitro*, the 10 µL aqueous solutions of different-sized ICG-AuNPs were reacted with 190 µl PBS containing 1mM GSH, 1 mM cysteine, and 1 mM GSH/Cys mixture, respectively. The GSH/Cys mixture was made by

dissolving 0.5 mmol GSH and 0.5 mmol Cysteine in 1 L PBS. The fluorescence of different-sized ICG-AuNPs was instantaneously monitored over time using the plate reader. To investigate the effect of protein binding on the nanoparticle-biothiol interactions *in vitro*, 1mM GSH, 1 mM cysteine, and a 1 mM GSH/Cys mixture were prepared in 190 µl PBS and 190 µl 50% v/v PBS/FBS solution, respectively. These thiol solutions were reacted with 10 µL aqueous solutions of different-sized ICG-AuNPs, respectively and the fluorescence of different-sized ICG-AuNPs were instantaneously monitored over time using the plate reader. To monitor the fluorescence enhancement kinetics, the excitation wavelength was set as 760 nm and the emission wavelength was set as 830 nm.

Statistics and reproducibility

Welch's t-test was used to compare two groups of data and analysis of variance (ANOVA) was used for the comparison of multiple data points among data sets. Data were reported as mean values with error bars representing the standard deviation. Differences were considered statistically significant when $P < 0.05$. Unless otherwise specified, all of the experiments were repeated at least three times with similar results to ensure reproducibility.

2.6 Acknowledgement

This study was in part supported by the NIH (1R01DK115986), NIH (1R01DK126140), and CPRIT (PR200233), from the University of Texas at Dallas (J.Z).

2.7 Author contributions

J.Z. conceived the idea and designed experiments with Q.Z.; Q.Z. performed *in vitro* experiments and analyzed data with J.Z.; S.L. and Y.H. assisted with *in vitro* experiment; Z.M assisted with the NMR measurement; Q.Z. wrote the manuscript; J.Z revised the manuscript; J.Z. supervised the whole project. All authors discussed the results and commented on the manuscript.

CHAPTER 3

NANOPARTICLE-BIOTHIOL INTERACTIONS *IN VIVO*

Authors – Qinhan Zhou, Siqing Li, Yingyu Huang, and Jie Zheng

Department of Chemistry and Biochemistry, BSB 13

The University of Texas at Dallas

800 West Campbell Road

Richardson, Texas 75080, USA

3.1 Abstract

The correlation between the nanoparticle-biochemical interactions at the *in vitro* level and at the *in vivo* level remains poorly understood due to the lack of a method to visualize and quantitatively analyze such interactions both at the *in vitro* and *in vivo* level. By utilizing the unique fluorescence "on-off" properties of ICG-AuNPs, we quantitatively compared the nanoparticle-biothiol interactions both at the *in vitro* and *in vivo* levels. The nanoparticle-biothiol interactions at the *in vitro* and *in vivo* levels were both found to be nanoparticle size-dependent. Meanwhile, there was a strong correlation between the size-dependency at the *in vitro* and *in vivo* levels. We believe such findings will not only offer a new way to fundamentally understand the nanoparticle-biochemical interactions at both the *in vitro* and *in vivo* levels, but also provide insight into the biomedical applications of nanoparticles like disease detections.

3.2 Introduction

The past several decades have witnessed the unprecedented developments of engineered nanomaterials in biomedical applications, such as disease diagnosis[21] as well as treatment[13]. Due to the controllable physical and physiological properties, the engineered nanoparticles hold great potential in the biomedical field like biosensing, bioimaging, drug delivery, and gene therapy, *etc*. Fundamental understanding of the interactions between the engineered nanoparticles and the biological system not only provides critical information for the design of desired nanoparticles but also provides insights into the physiology at the nanoscale. In recent years, increasing research has been conducted to investigate the *in vivo* fate of engineered nanoparticles[13, 14, 21, 22, 32]. In these works, the researchers focused on two aspects: first, the understanding of how the

engineered nanoparticles transport between different organs as well as the clearance pathway of nanoparticles, which is so-called the "*in vivo* transport" of engineered nanoparticles; second, how the engineered nanoparticles interact with physiological systems, like different organs, tissues, and cells, which is so-called the "nano-bio interactions" of engineered nanoparticles. However, few of them focus on how the nanoparticle interacts with the biochemicals and how these nano-bio interactions at the molecular level affect the *in vivo* behavior of the nanoparticles.

By designing a library of thiol-responsive organic dye conjugated gold nanoparticles of different sizes, we systematically investigated how the nanoparticle interacts with the specific biochemical—glutathione. Meanwhile, we correlated the *in vitro* nanoparticle-biothiol interactions with the *in vivo* nanoparticle-biothiol interactions. We observed that at *in vivo* level, the different sized nanoparticles interact with the glutathione efflux from the liver at different reaction rates. It should be pointed out that such size-dependent nanoparticle-biothiol interactions found in the liver could be perfectly correlated with the nanoparticle-biothiol interactions *in vitro*. Furthermore, we investigated how these size-dependent nanoparticle-biothiol interactions would affect the *in vivo* behavior of the nanoparticles, especially the blood retention profile as well as the clearance pathway of nanoparticles.

In summary, in this chapter, we first report that the correlation between nanoparticle interactions *in vitro* and *in vivo*, suggesting that the *in vivo* behavior of nanoparticles can be predicted by the *in vitro* results. Second, we found that the nanoparticle-biothiol interactions in the liver dominated the blood retention profile as well as the clearance pathway of nanoparticles, which provide insights into how the nanoparticle-biochemical interactions would affect the *in vivo* fate of nanoparticles.

3.3 Results and discussions

3.3.1 Nanoparticle-biothiol interactions in the liver

In Chapter 2, the interactions between the different-sized ICG-AuNPs and thiols have been investigated systematically *in vitro*. In this chapter, the interactions between the different-sized ICG-AuNPs and thiols *in vivo* will be explored.

In Chapter 2, we observed that the interactions between the ICG-AuNPs and biothiols in vitro were size-dependent. The reaction activity of smaller-sized ICG-AuNPs was higher than larger ones except for ICG-Au25, and ICG-Au25 exhibits the highest resistance against thiols etching. To verify whether the size trend of the interactions between the ICG-AuNPs and biothiols also exist at the *in vivo* level, we treated the balb/c mice (n=3 for each group) with different sizes of ICG-AuNPs and monitored the fluorescence activation in the liver over time. For the comparison of the liver fluorescence activation activity between different-sized ICG-AuNPs, the injection dose of each ICG-AuNPs in terms of ICG were kept the same, which was 150 μL 20 μM per mouse in terms of ICG. As shown in Figure 3.1, the time-dependent noninvasive fluorescence images display the efficient fluorescence activation of different-sized ICG-AuNPs in the liver after systematic administration. The ICG fluorescence of these four ICG-AuNPs was immediately activated in the liver site and the fluorescence intensity increased over time.

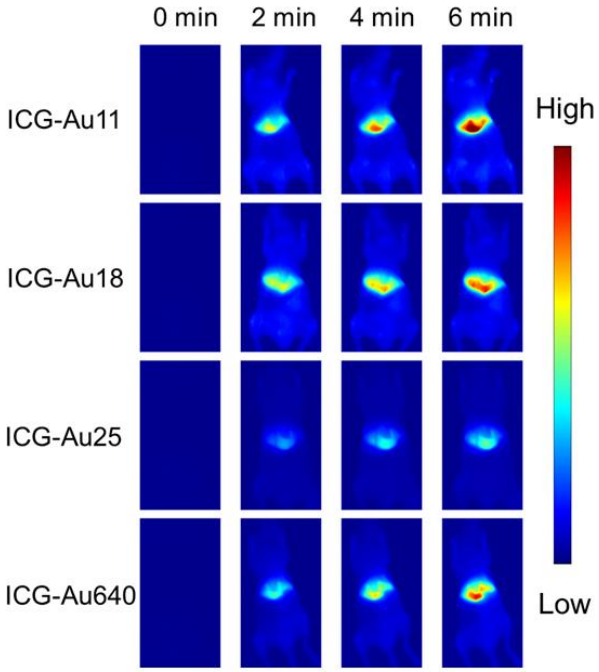

Figure 3.1. Time-dependent noninvasive fluorescence images of the fluorescence activation of different-sized ICG-AuNPs in the liver of normal mice.

The time-dependent fluorescence images of different-sized ICG-AuNPs were then quantitatively analyzed. As shown in Figure 3.2 a, the fluorescence intensity of ICG-Au11, ICG-Au18, ICG-Au25, and ICG-Au640 in the liver all increased linearly over time. The different slope of the fluorescence intensity curves of different-sized ICG-AuNPs reflected the difference in the reaction activity in the liver. The slope of the curves in Figure 3.2 a were calculated as the reaction activity *in vivo* and the reaction activity of different-sized ICG-AuNPs were compared quantitatively in Figure 3.2 b. The reaction activity in the liver of ICG-Au11, ICG-Au18, ICG-Au25, and ICG-Au640 were 62.74 ± 8.61 s^{-1}, 48.38 ± 5.27 s^{-1}, 27.57 ± 2.44 s^{-1} and 42.12 ± 9.29 s^{-1}, respectively. At the *in vivo* level, the reaction activity between biothiols and ICG-Au11 was the highest one, followed by ICG-au18, ICG-Au640, and ICG-Au25.

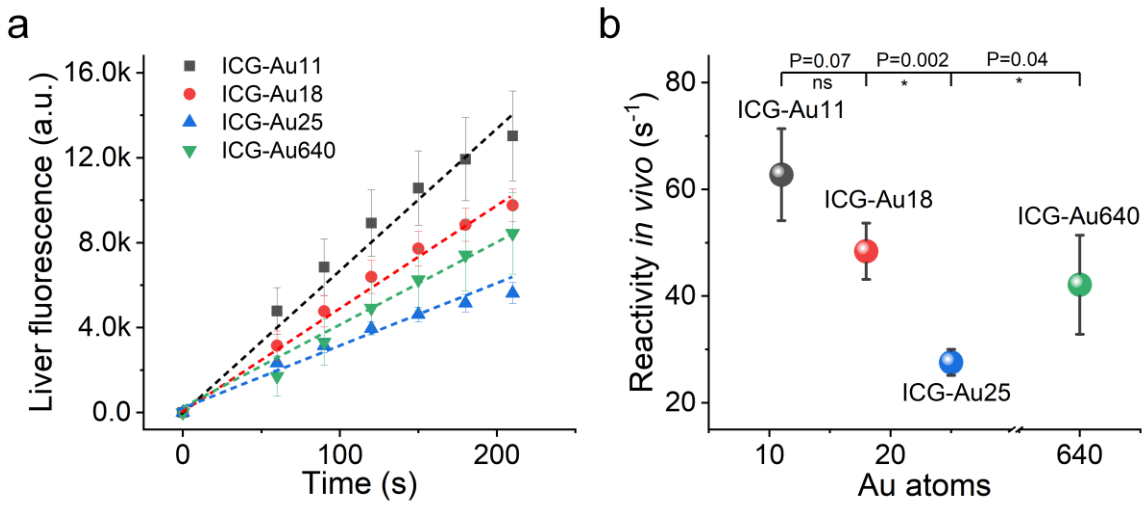

Figure 3.2. The fluorescence activation kinetics of different-sized ICG-AuNPs in the liver. (a) The time-dependent ICG fluorescence curves in the mice liver after injection of different-sized ICG-AuNPs with the same dose in terms of ICG. (b) The calculated liver fluorescence activation kinetics of different-sized ICG-AuNPs.

The size trend of reaction activity *in vivo* was consistent with the size trend *in vitro*, see Figure 3.3 a. In Figure 3.3 b, we plotted the reactivity of different-sized ICG-AuNPs *in vivo* versus *in vivo* and Pearson correlation was applied to indicate the correlation between the *in vitro* and *in vivo* reactivity. Pearson correlation coefficient (Pearson's r) was 0.99, which indicates the strong correlation between the reactivity of different sized AuNPs *in vitro* and *in vivo*. Such a strong correlation between the *in vitro* results and *in vivo* results suggests that the nanoparticle-biochemical interactions *in vitro* could be utilized to predict the nanoparticle-biochemical interactions *in vivo*.

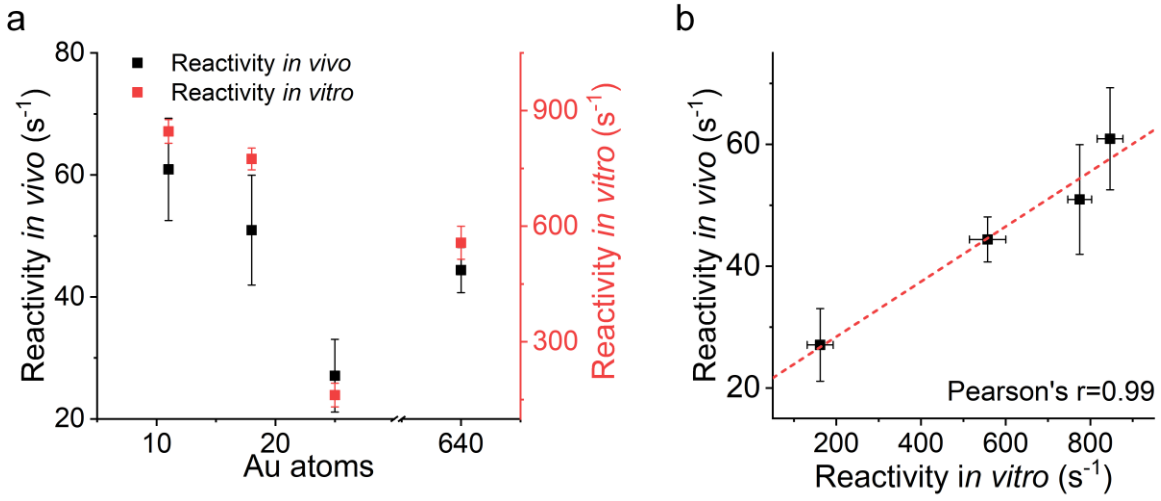

Figure 3.3. The reaction activity of different-sized ICG-AuNPs *in vitro* and *in vivo*. a) The reactivity of different-sized ICG-AuNPs *in vitro* (red line) and *in vivo* (black line). b) The correlation between the reactivity of different-sized ICG-AuNPs *in vitro* and *in vivo*.

3.3.2 Nanoparticle-biothiol interactions in the blood

In section 3.3.1, we investigated the interactions between the different-sized ICG-AuNPs and the thiol efflux from the liver. This type of nanoparticle-biochemical interactions *in vivo* was strongly correlated with the interactions *in vitro*. After that, we explored how this nanoparticle-biothiol interaction would affect the *in vivo* transport of nanoparticles.

Unlike free ultrasmall AuNCs which could be eliminated out of the body efficiently through urine, ICG-AuNCs were prevented from rapid kidney clearance because ICG-AuNPs bind to serum proteins, making their size larger than the kidney filtration threshold and inducing the rapid transport to the liver after systematic administration. After intravenous injection, the ICG-

AuNCs were transported into the liver and the ICG molecules were detached from the surface of ICG-AuNCs by the GSH and cysteine efflux from hepatocytes. After this biotransformation, the detached ICG were taken up by hepatocytes and eliminated through the hepatobiliary clearance pathway, while the biotransformed AuNCs were transported back to blood circulation and were cleared out of the body through the kidney.

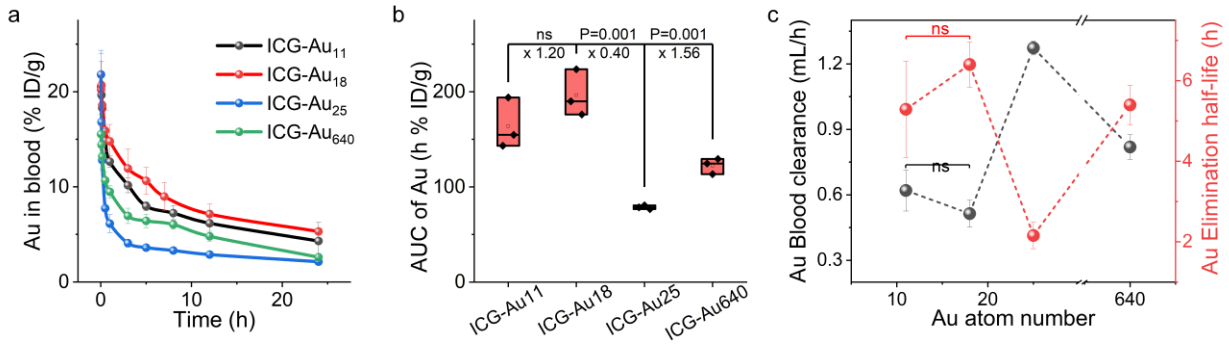

Figure 3.4. The blood retention of ICG-AuNPs in terms of Au. (a) The time-dependent Au concentration in blood of ICG-AuNPs within 24 hours after injection. (b) The area under the curve (AUC) of the blood retention of ICG-AuNPs in terms of Au within 24 hours. (c) The blood clearance and elimination half-life of different-sized ICG-AuNPs in terms of Au.

To further understand the *in vivo* behavior of ICG-AuNCs, we investigated the blood pharmacokinetics of ICG-AuNCs based on ICG and Au separately. We first quantified the Au amount in blood over time (Figure 3.4 a) and compared the AUC of the blood pharmacokinetic (PK) based on Au (Figure 3.4 b). The PK profiles in terms of Au were also quantitatively analyzed by measuring the Au amount in the blood over time, where all four PK profiles followed a two-component decay model (Figure 3.4). The Au based AUC of ICG-Au11, ICG-Au18, ICG-Au25, and ICG-Au640 were 163.95±26.62 h%ID/g, 196.57±24.43 h%ID/g, 78.59±1.99 h%ID/g, and 122.45±8.22 h%ID/g. The Au-based AUC of ICG-Au11 and ICG-Au18

were higher than ICG-Au25, suggesting that after reacting with biothiols from the liver, the biotransformed ICG-Au11 and ICG-Au18 exhibit longer blood retention than ICG-Au25, which is consistent with our group's previously result that smaller AuNCs exhibit longer blood retention than larger ones[31]. Moreover, ICG-Au25 also exhibits the largest blood clearance and fastest elimination half-life among these four ICG-AuNCs (Figure 3.4 c), which was consistent with the shortest Au-based blood retention of ICG-Au25 (Figure 3.4 a and b).

Then, we examined the PK profiles of ICG-AuNCs based on ICG. Two forms of ICG can exist in blood over time: 1) the detached free ICG molecules which were detached from the surface of the ICG-AuNCs by biothiol efflux from liver hepatocytes, and 2) the undetached ICG which remained on the surface of ICG-AuNCs. Due to the "on-off" activatable fluorescence properties of ICG-AuNCs, the fluorescence of undetached ICG molecules in the extracted blood samples were quenched and could only be detected after external thiol etching. Thus, we collected the blood samples from the mice after administration of ICG-AuNCs at each time point and measured the fluorescence intensity (Figure 3.5 a), which can directly reflect the amount of detached free ICG in the blood. After that, we incubated the samples with external thiol DTT to let the DTT fully detach the ICG from the surface of ICG-AuNCs, then we quantify the fluorescence intensity again (Figure 3.5 b), which reflects the total ICG amount in the blood (the sum of free detached ICG and undetached ICG). The fluorescence of free ICG in the blood of all ICG-AuNCs was low and became undetectable after 1h post-injection (Figure 3.5 a), which suggested that there was a very limited amount of detached ICG molecules in blood circulation. However, after incubation with external DTT, the fluorescence intensities of the blood samples in all ICG-AuNCs dramatically increased (Figure 3.5 b), suggesting most of the circulating ICG

molecules in the blood were still conjugated to the AuNCs. The ICG-based AUC of ICG-Au11, ICG-Au18, ICG-Au25, and ICG-Au640 are 3.09±0.53 h%ID/g, 5.96±1.14 h%ID/g, 10.93±1.43 h%ID/g, and 11.28±1.65 h%ID/g, which suggest the blood retention increased as the nanoparticle size increased (Figure 3.5 c). The ICG blood clearance and elimination half-life also confirmed this size dependency (Figure 3.5 d).

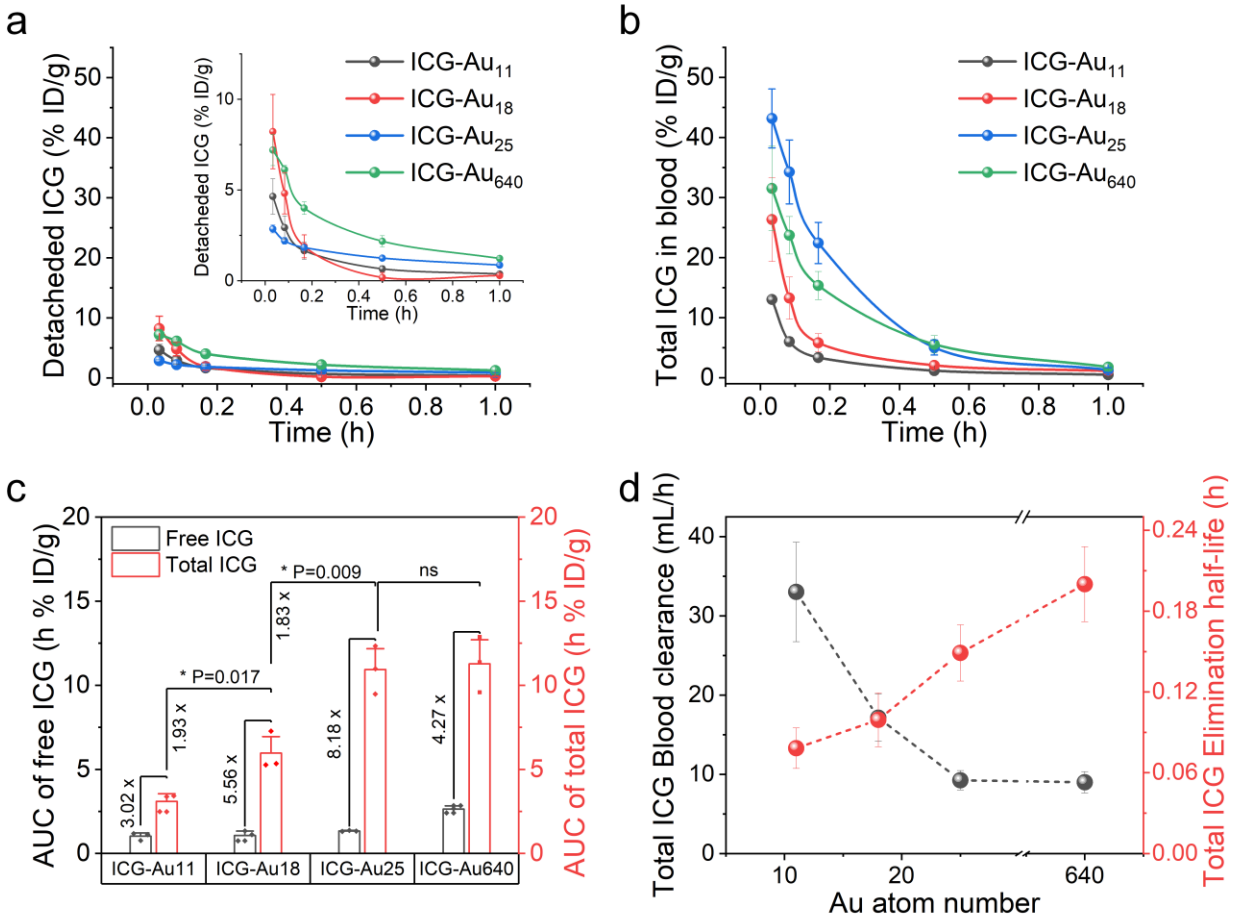

Figure 3.5. The blood retention of ICG-AuNPs in terms of ICG. (a) The time-dependent free ICG concentration in blood of ICG-AuNPs after systematic administration. (Inset: zoomed-in time-dependent free ICG concentration in blood of ICG-AuNPs) (b) The time-dependent total ICG (conjugated ICG + detached ICG) concentration in blood of ICG-AuNPs after systematic administration. (c) The area under the curve (AUC) of the blood retention of detached free ICG (black) and total ICG (red) after systematic administration. (d) The blood clearance and elimination half-life of different-sized ICG-AuNPs in terms of ICG.

By plotting the AUC of the ICG-based PK profile versus the *in vivo* reaction rate, we found a strong linear correlation among them (Pearson's r was -0.933), which suggests that the higher ICG-based blood retention of large-sized ICG-AuNCs was fundamentally due to the low reaction rate of the larger sized ICG-AuNCs with the thiols in the liver (Figure 3.6).

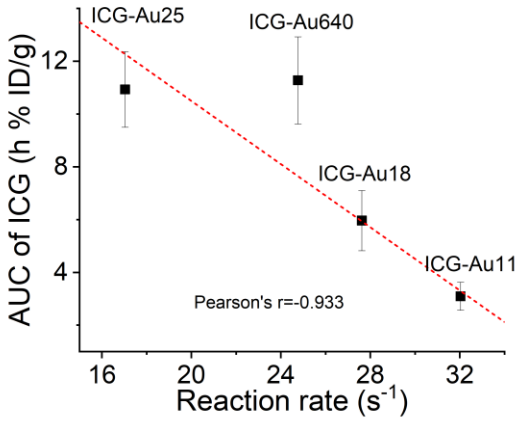

Figure 3.6. The correlation between the blood retention of ICG-AuNPs in terms of ICG and the nanoparticle-thiols reactivity in the liver.

3.4 Conclusion

In this chapter, we investigated the interactions between the nanoparticle and the thiol efflux from the liver. The size-dependency of the interactions between the ICG-AuNPs and liver thiols was explored. The interaction rate of the ICG-AuNPs decreases with the increase of the nanoparticle size from ICG-Au11 to ICG-Au25, then the rate of the interaction of the ICG-AuNPs increases with the increase of the nanoparticle size from ICG-Au25 to ICG-Au640. Such size-dependence of the nanoparticle-biothiol interactions *in vivo* correlated perfectly with the nanoparticle-biothiol interactions at the *in vitro* level. Then, we found that the blood retention of

ICG-AuNPs in terms of ICG was also size-dependent, which fundamentally resulted from the size-dependence of the nanoparticle-biothiol interactions in the liver.

This chapter illustrates the correlation between the chemical reactions *in vitro* and the nano-bio interactions *in vivo*. The nanoparticle-biothiol interactions *in vivo* could be predicted by the nanoparticle-biothiol interactions *in vitro* due to the strong correlation between the nanoparticle-biothiol interactions *in vitro* and *in vivo*. These findings will build a bridge of chemical reactions *in vitro* and *in vivo* study so that the complicated interactions *in vivo* can be mimicked *in vitro,* and the *in vivo* nano-bio interactions could be investigated via the methodology developed *in vitro*.

3.5 Experiment

3.5.1 Materials and equipment

ICG-NHS was obtained from AdipoGen Life Science, Inc. Fetal Bovine Serum (FBS) was purchased from Corning, Inc. All the other chemicals were purchased from Sigma-Aldrich and used as received without further purification. Ultra-centrifugal filter units with the molecular weight cut-off (MWCO) of 3k, 10k, and 30k Da (MilliporeSigma™ Amicon™) were utilized for the purification of gold nanoparticles and ICG conjugated gold nanoparticles. The amount of gold was measured by Agilent 7900 inductively coupled plasma mass spectrometer (ICP-MS). The pH was measured by an Accumet AB15 pH meter and an Accuphast microprobe electrode. Agarose gel electrophoresis was carried out in a Bio-Rad Mini-Sub Cell GT system (Bio-Rad Laboratories, Inc. USA). The absorption spectra were collected with a Virian 50 Bio UV-vis spectrophotometer. The luminescence spectra of different-sized nanoparticles were detected with

a PTI QuantaMasterTM 30 Fluorescence Spectrophotometer (Birmingham, NJ). The time-dependent fluorescence enhancement of ICG-AuNPs was monitored using the BioTek Synergy H4 plate reader. *In vivo* fluorescence images were recorded using a Carestream In-vivo FX Pro imaging system. Optical images of cultured cells and tissue slides were obtained with an Olympus IX-71 inverted fluorescence microscope coupled with Photon Max 512 CCD camera (Princeton Instruments). Animal studies were performed according to the guidelines of the University of Texas System Institutional Animal Care and Use Committee. BALB/c mice (BALB/cAnNCr, strain code 047) of 6-8 weeks old, weighing 20-25g, were purchased from Envigo. Nude mice (Athymic NCr-nu/nu, strain code 069) of 6-8 weeks old, weighing 20-25 g, were also purchased from Envigo. All of these mice were randomly allocated and housed under standard environmental conditions (23±1 ℃, 50±5% humidity, and a 12/12 h light/dark cycle) with free access to water and standard laboratory food.

3.5.2 Methods

In vivo fluorescence imaging of different-sized ICG-AuNPs

The fur of 6~8 weeks old Balb/c mice (~25 g/mouse) was removed a day before the imaging. Under 3% isoflurane anesthesia, the mouse was tail-vein catheterized and prone-positioned on the imaging stage. Different-sized ICG-AuNPs were dissolved in 150 μL PBS respectively with the ICG concentration of 20 μM. The mice were intravenously injected with ICG-AuNPs following by sequential time-series fluorescence imaging. The excitation and emission wavelength of the fluorescence imaging are 760 nm and 780 nm respectively. The exposure time of each imaging was 10s. The binning of the imaging was set as 2 x 2.

Pharmacokinetics study of ICG-AuNPs

BALB/c mice were i.v. injected with 150 μL ICG-AuNPs (the amount of ICG was about 20 μM the amount of ICG, in PBS) per mouse. At a certain time point post-injection, a blood sample (~30 μL) was retro-orbitally collected and weighed, followed by the addition of 1 mL PBS solution containing 2 wt.% of ethylenediaminetetraacetic acid (EDTA) (pH=8). Then, the fluorescence of the blood samples was measured by the *in vivo* imaging system as the "fluorescence off state". After that, 200 μL 20 mM dithiothreitol (DTT) solution was added to the blood sample and stored in a dark place to avoid light exposure. After 1 hour of incubation, the fluorescence of the DTT treated blood sample was measured by the *in vivo* imaging system as the "fluorescence on state".

The amount of ICG in the blood samples was quantified through the fluorescence according to the preestablished standard curve using the *in vivo* imaging system. After that, the blood sample was completely dissolved in freshly made aqua regia and the Au amount in blood was analyzed by ICP-MS.

Statistics and reproducibility

Welch's t-test was used to compare two groups of data and analysis of variance (ANOVA) was used for the comparison of multiple data points among data sets. Data were reported as mean values with error bars representing the standard deviation. Differences were considered statistically significant when $P < 0.05$. Unless otherwise specified, all of the experiments were repeated at least three times with similar results to ensure reproducibility.

3.6 Acknowledgements

This study was in part supported by the NIH (1R01DK115986), NIH (1R01DK126140), and CPRIT (PR200233), from the University of Texas at Dallas (J.Z).

3.7 Author contributions

J.Z. conceived the idea and designed experiments with Q.Z.; Q.Z. performed *in vitro* experiments and analyzed data with J.Z.; S.L. and Y.H. assisted with *in vitro* experiment; Q.Z. wrote the manuscript; J.Z revised the manuscript; J.Z. supervised the whole project. All authors discussed the results and commented on the manuscript.

CHAPTER 4

THE APPLICATION OF NANOPARTICLE-BIOTHIOL INTERACTIONS IN DISEASED MICE

Authors – Qinhan Zhou, Siqing Li, Yingyu Huang, and Jie Zheng

Department of Chemistry and Biochemistry, BSB 13

The University of Texas at Dallas

800 West Campbell Road

Richardson, Texas 75080, USA

4.1 Abstract

Fundamental understanding of the *in vivo* behaviour of engineered nanomaterials are crucial to the successful application of nanomaterial-based disease detection and treatment. Herein, by designing a library of fluorescent gold nanoparticles-ICG-AuNPs, we systematically investigated the nanoparticle-biothiol interactions, *in vivo* transport, and tumor targeting effect of ICG-AuNPs in the tumor-bearing mice. We observed the size-dependency of nanoparticle-biothiol interactions in the tumor-bearing mice, and such size-dependency nanoparticle-biothiol interactions result in the size-dependency of the blood retention as well as the tumor-targeting effect of ICG-AuNPs. We envision that such investigation would not only provide the information of physiology at the nanoscale but also help the design of the next generation of nanomedicine for disease diagnosis and therapy.

4.2 Introduction

The past decades have witnessed a dramatic development of nanomaterials in cancer detection and therapy. Compared to conventional chemotherapeutic drugs, these novel nanomaterials are designed to deliver the imaging agents or therapeutics to the tumor site with high concentration and to lower the nonspecific systemic toxicity. The stimuli-responsive nanomaterials can further optimize the efficacy of treating tumors. The physicochemical properties of these stimuli-responsive nanomaterials change drastically in response to the tumor microenvironment, which could precisely release the payload at the tumor site. Among them, thiol-activatable nanoparticles are widely used to deliver imaging and therapeutic agents to solid tumors by taking advantage of the dissociation of cargo and vehicles due to the evaluated glutathione level in the

tumor microenvironment. However, it is still unclear how the *in vivo* transport of nanoprobes affects their tumor-targeting efficiencies.

Recently, our group designed a thiol-activatable fluorescent gold nanoprobe–ICG-Au25, whose fluorescence can be activated through glutathione (GSH) biotransformation to enhance the tumor-targeting efficiency of ICG. However, the fast renal clearance and low blood retention of Au25 limit the tumor-targeting efficiency of ICG-Au25, which makes Au25 not a perfect vehicle for delivery of imaging agents or therapeutic agents to diseased tissue like tumors. In our previous work[31], we observed that *in vivo* transport and blood retention of nanoparticles could be tailored by precisely changing the size of the nanoparticles. Therefore, it would be possible to enhance the tumor-targeting of ICG-Au25 by tailoring the size of AuNCs.

Herein, to systematically investigate how the size of nanoparticles would affect the tumor targeting of ICG-AuNCs, we conjugated ICG on a series of gold nanoclusters with different sizes to get ICG-Au11, ICG-Au18, ICG-Au25, and ICG-Au640, and then compared their tumor targeting efficiency. We observed the tumor-targeting efficiency in terms of ICG increases with the size of ICG-AuNCs increases, while the tumor-targeting efficiency in terms of gold decreases with the size of ICG-AuNCs increases. To unravel the origin of this contradictory size-dependent tumor-targeting effect, we investigated the blood pharmacokinetics of the ICG-AuNCs and quantitatively compare the reaction rate of ICG-AuNCs with hepatic GSH in the liver. We found that the contradictory size-dependent tumor-targeting effect could be attributed to the reversed ICG-based and Au-based blood retention of ICG-AuNCs. And the reversed blood retention in terms of ICG and Au was fundamentally due to the *in vivo* transport of ICG-AuNCs modulated by size-dependent hepatic GSH-mediated biotransformation. These findings offer a new method

to modulate the tumor target efficiency of thiol-activatable nanoparticles through the control of the GSH-mediated biotransformation in the liver.

4.3 Results and discussions

4.3.1 The nanoparticle-biothiol interactions in the liver of tumor-bearing mice

In Chapter 3, the nanoparticle-biothiol interactions in the normal mice were discussed and these interactions were size-dependent. In this chapter, we would like to explore whether this size-dependent nanoparticle-biothiol interaction also exists in diseased mice. First, we conducted the experiments in tumor-bearing mice. The reason we chose tumor-bearing mice is ICG-Au25 has been proved that can successfully target tumors by our group[10], and we would like to investigate how the interactions ICG-AuNPs with biothiols would affect their tumor targeting. Therefore, the 4T-1 tumor-bearing mice were intravenously injected with the different-sized ICG-AuNPs, followed by the time-dependent noninvasively fluorescence imaging. The amount of ICG in different-sized ICG-AuNPs was controlled as the same before injection, which was 150 μL 20 μM per mouse. As shown in Figure 4.1, the time-dependent noninvasive fluorescence images of the tumor-bearing mice display the efficient fluorescence activation of different-sized ICG-AuNPs in the liver after systematic administration. The ICG fluorescence of these four ICG-AuNPs was immediately activated in the liver site and the fluorescence intensity increased over time, which was similar to that of normal mice.

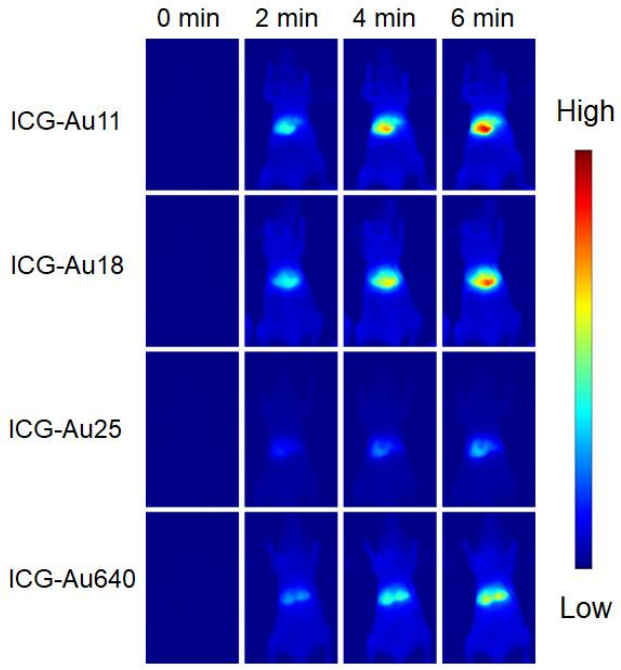

Figure 4.1. Time-dependent noninvasive fluorescence images of the fluorescence activation of different-sized ICG-AuNPs in the liver of 4T-1 tumor-bearing mice.

The time-dependent noninvasive fluorescence images of different-sized ICG-AuNPs of 4T-1 tumor-bearing mice were then quantitatively analyzed in Figure 4.2. As shown in Figure 4.2 a, the fluorescence intensity of ICG-Au11, ICG-Au18, ICG-Au25, and ICG-Au640 in the liver 4T-1 tumor-bearing mice all increased linearly over time, which is similar to normal mice. The different slope of the fluorescence intensity curves of different-sized ICG-AuNPs reflected that the difference in the reaction activity in the liver. Similar to normal mice, the slope of the curves in Figure 4.2 a were also calculated as the reaction activity *in vivo* and were compared quantitatively in Figure 4.2 b. The reaction activity in the liver of 4T-1 tumor-bearing mice of ICG-Au11, ICG-Au18, ICG-Au25, and ICG-Au640 was 60.90 ± 8.37 s^{-1}, 50.95 ± 9.00 s^{-1}, 27.08 ± 5.96 s^{-1} and 44.39 ± 3.70 s^{-1}, respectively.

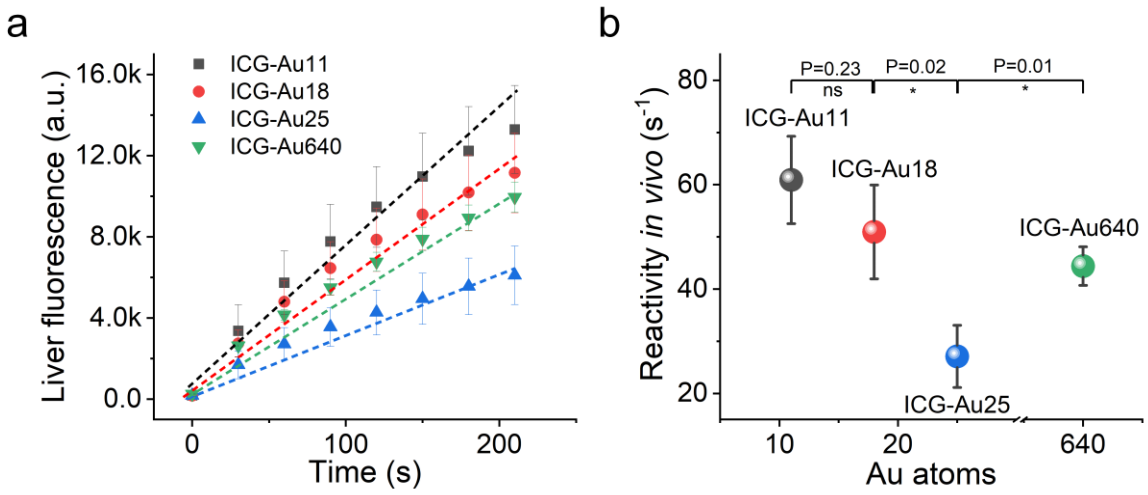

Figure 4.2. The fluorescence activation kinetics of different-sized ICG-AuNPs in the liver of 4T-1 tumor-bearing mice. (a) The time-dependent ICG fluorescence curves in the liver of 4T-1 tumor-bearing mice after injection of different-sized ICG-AuNPs with the same dose in terms of ICG. (b) The calculated liver fluorescence activation kinetics of different-sized ICG-AuNPs in 4T-1 tumor-bearing mice.

In 4T-1 tumor-bearing mice, the reaction activity between biothiols and ICG-Au11 was also the highest one, followed by ICG-Au18, ICG-Au640, and ICG-Au25. The size trend of reaction activity in 4T-1 tumor-bearing mice was the same as that in normal mice (Figure 4.3). We quantitatively compared the reaction activity in 4T-1 tumor-bearing mice (Figure 4.3 b) with that in normal mice (Figure 4.3 a) for each ICG-AuNPs, no statistically significant difference was observed (Figure 4.3 c).

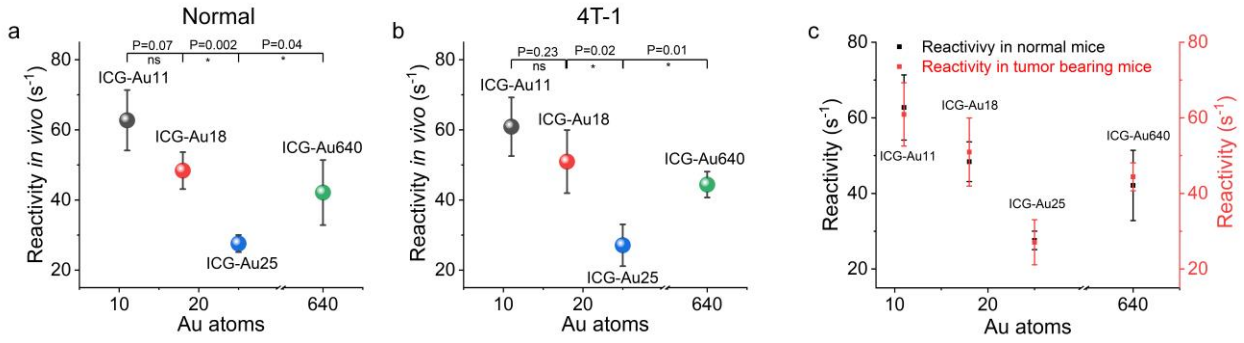

Figure 4.3. The comparison of the reaction activity between different-sized ICG-AuNPs and biothiols in normal mice and diseased mice. (a) The reaction activity between different-sized ICG-AuNPs and biothiols in normal mice. (b) The reaction activity between different-sized ICG-AuNPs and biothiols in 4T-1 tumor-bearing mice. (c). The comparison of the reaction activity between different-sized ICG-AuNPs and biothiols in normal mice and diseased mice.

The reaction reactivity of the interactions between different-sized ICG-AuNPs and biothiols were comparable, and we hypothesize that the liver GSH concentration in the 4T-1 tumor mice was not changed due to the tumor implantation. Therefore, we measured the liver GSH concentration in the normal mice as well as the GSH concentration in the liver of 4T-1 tumor-bearing mice. As shown in Figure 4.4, the liver GSH concentration in the liver of normal mice was 6.4 ± 0.45 µmole/g tissue, while the liver GSH concentration in the liver of 4T-1 tumor-bearing mice were 6.2 ± 0.31 µmole/g tissue. There is no statistically significant difference between the GSH liver in normal mice and 4T-1 tumor-bearing mice (P = 0.55). In conclusion, the reaction activity of different-sized ICG-AuNPs in the 4T-1 tumor-bearing mice were not changed compared to the normal mice, which is fundamental since the GSH concentration in the 4T-1 tumor-bearing mice was not changed compared to normal mice. Combing the reaction activity of different-sized ICG-AuNPs *in vitro* as well as the reaction activity in normal or

diseased mice, the reaction activity of different-sized ICG-AuNPs *in vivo* was fundamentally modulated by the liver thiol levels.

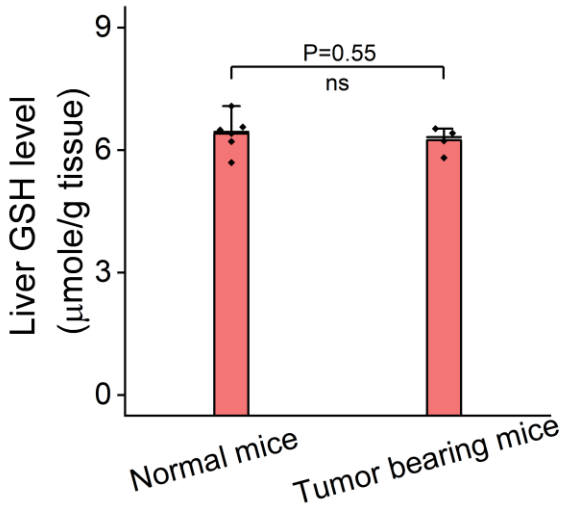

Figure 4.4. The liver glutathione concentration in normal and diseased mice. The liver glutathione concentration in normal Balb/c mice and 4T-1 tumor-bearing mice was not significantly different.

4.3.2 The correlation of nanoparticle-biothiol interactions in liver and tumor

After investigating the relationships of the fluorescence activity of different-sized ICG-AuNPs in the livers of the normal mice and the tumor-bearing mice in section 4.3.1, we further studied the fluorescence activity of different-sized ICG-AuNPs in the tumor. As shown in Figure 4.5, we quantitatively monitored the fluorescence intensity of different-sized ICG-AuNPs in the liver (Figure 4.5 a) and the tumor tissue (Figure 4.5 c) within 4 minutes post-injection of different-sized ICG-AuNPs in the 4T-1 tumor-bearing mice. The fluorescence intensity of different-sized ICG-AuNPs in the liver and tumor both linearly increased over time. Then, we compared the

reactivity of different-sized ICG-AuNPs by quantitatively analyzing the slope fluorescence enhancement of different-sized ICG-AuNPs in the liver (Figure 4.5 b) and tumor (Figure 4.5 d). The reactivity of different-sized ICG-AuNPs in the liver and tumor are both size-dependent and the size trend are similar that from ICG-Au11 to ICG-Au25, the reactivity in the liver and tumor both decrease with the increase of the size of ICG-AuNPs while from ICG-Au25 to ICG-Au640, the reactivity in the liver and tumor both increase with the increase of the size of ICG-AuNPs. The size-dependent reactivity of ICG-AuNPs in the liver was fundamentally due to the size-dependent reaction rate between the different-sized ICG-AuNPs with the glutathione in the liver. Therefore, we hypothesis that the size-dependent reactivity of ICG-AuNPs in the tumor may also result from the size-dependent reaction rate between the different-sized ICG-AuNPs with the glutathione in the tumor. Furthermore, we hypothesis that the glutathione level in the tumor would be lower than that in the liver due to the fluorescence activity of all these four types of ICG-AuNPs in the tumor being lower than that in the liver.

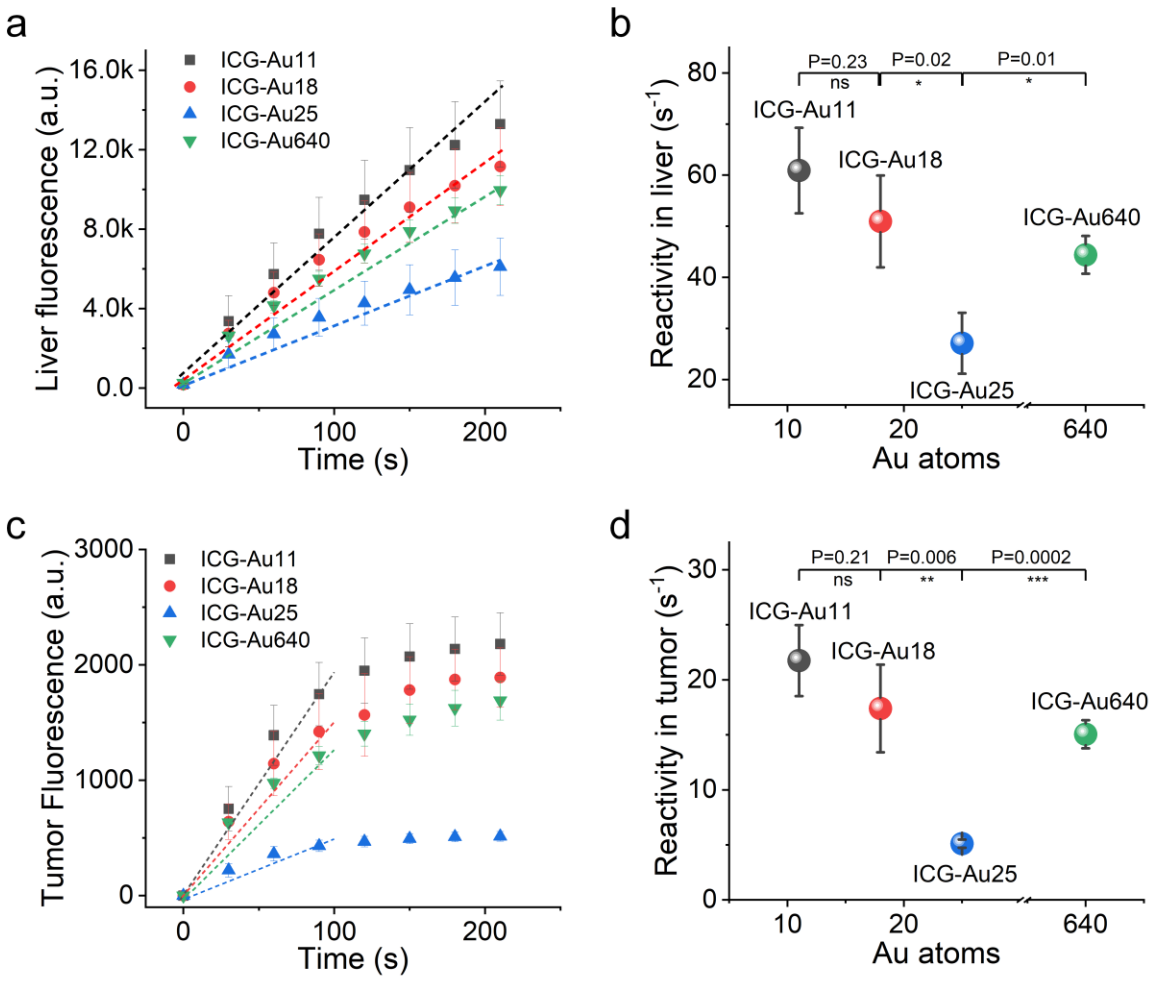

Figure 4.5. The comparison of the reaction activity of different-sized ICG-AuNPs between the liver and tumor of 4T-1 tumor-bearing mice. (a) The time-dependent ICG fluorescence curves in the liver of 4T-1 tumor-bearing mice after injection of different-sized ICG-AuNPs with the same dose in terms of ICG. (b) The calculated liver fluorescence activation kinetics of different-sized ICG-AuNPs in 4T-1 tumor-bearing mice. (c) The time-dependent ICG fluorescence curves in the tumor of 4T-1 tumor-bearing mice after injection of different-sized ICG-AuNPs with the same dose in terms of ICG. (d) The quantitative analysis of the tumor fluorescence activation kinetics of different-sized ICG-AuNPs in 4T-1 tumor-bearing mice.

To verify these two hypotheses, we measured the glutathione level in the liver as well as in the tumor of the 4T-1 tumor-bearing mice (Figure 4.6 a), and we also compared the fluorescence reactivity of ICG-AuNPs in the liver versus in the tumor (Figure 4.6 b). The GSH concentration

in the liver of 4T-1 tumor-bearing mice were 6.2 ± 0.31 μmole/g tissue, which is 8.23 folds higher than the GSH concentration in the tumor (0.76 ± 0.25 μmole/g tissue). Combing these results suggests that the lower fluorescence reactivity of ICG-AuNPs in the tumor than that in the liver results from the lower GSH concentration in the tumor than that in the liver. In Figure 4.10 b, the fluorescence reactivity of different-sized ICG-AuNPs in the liver and tumor were head-to-head compared. The fluorescence reactivity of ICG-Au11, ICG-Au18, ICG-Au25, and ICG-Au640 in the liver is 2.80 times, 2.93 times, 5.30 times, and 2.95 times higher than that of fluorescence reactivity in the tumor, respectively. However, the liver glutathione level was 8.23-fold higher than the glutathione level in the tumor, which is higher than the increase-times of the fluorescence activity of ICG-AuNPs between the liver and tumor (2.80~5.30 times). We hypothesis this inconsistency might result from the fact that the fluorescence intensity in the tumor was composed of (1) the ICG molecules on the surface of ICG-AuNPs detached by the glutathione in the tumor; (2) the free ICG molecules which were detached by the glutathione in the liver and transport into tumor site through the blood stream. If the tumor fluorescence solely comes from the ICG molecules on the surface of ICG-AuNPs detached by the glutathione in the tumor, the fluorescence activity of all these ICG-AuNPs in the tumor should be 8.23-fold lower than that in the liver. As shown in Figure 4.6 c, the fluorescence activity ratio between liver and tumor of ICG-Au25 was the closest one (5.30 versus 8.23 folds) to the GSH level ratio between liver and tumor, which followed by ICG-Au640 (2.95 versus 8.23 folds), ICG-Au18 (2.93 versus 8.23 folds) and ICG-Au11(2.80 versus 8.23 folds). This phenomenon may be due to the fact that the lowest fluorescence activity of ICG-Au25 in the liver, which leads to the fewest ICG molecules released in the liver and transported into the tumor through the bloodstream.

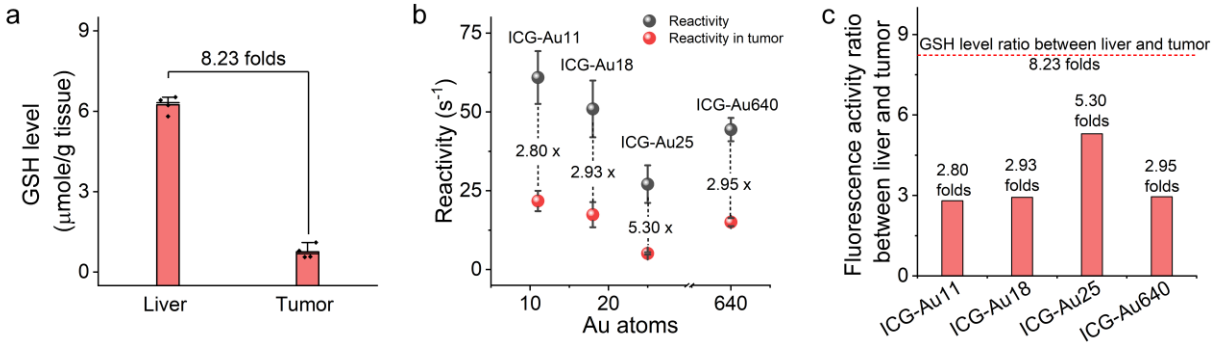

Figure 4.6. The correlation between the GSH level and the reactivity of different sized ICG-AuNCs in the liver and tissue. (a) the comparison of the GSH level in the liver and tumor. (b) the comparison of the reactivity of different sized ICG-AuNCs in the liver and tumor. (c) The comparison between the fluorescence activity ratio and GSH level ratio of the liver and tumor.

4.3.3 The *in vivo* behaviour of ICG-AuNPs mediated by the nanoparticle-biothiol interactions

In section 4.3.1, we found that the nanoparticle-biothiol interactions of ICG-AuNPs in the liver of healthy mice were comparable to that in the liver of 4T-1 tumor-bearing mice. It was because the nanoparticle-biothiol interactions of ICG-AuNPs were mediated by the glutathione in the liver, and the glutathione level in the liver of healthy mice was comparable to that in the tumor-bearing mice. In the following section 4.3.2, we investigated the correlation of the fluorescence activity of ICG-AuNPs in the liver and tumor. The fluorescence activity of ICG-AuNPs in the liver and tumor we studied were chemical reactions between the ICG-AuNPs and biothiols several minutes post injection of the ICG-AuNPs, which was the short-term (serval minutes) effect of the nanoparticle-biothiol interactions. Apart from this short-term effect of the nanoparticle-biothiol interactions, we would also investigate the long-term (24 hours) effect of

the nanoparticle-biothiol interactions in this section, which is the accumulated tumor-targeting effect of the ICG-AuNPs as well as the *in vivo* transport of ICG-AuNPs within 24 hours post injection of different-sized ICG-AuNPs.

After the nanoparticle-biothiol interactions of ICG-AuNPs in the liver, the detached ICG from the surface of ICG-AuNPs was eliminated by liver hepatocytes efficiently. While the undetached ICG was remained on the ICG-AuNPs surface and entered the blood circulation. We noninvasively monitored the ICG fluorescence of the tumor site over time after the mice were treated with different types of ICG-AuNPs with the same dose of ICG amount (Figure 4.7). Time-dependent quantitative analysis of fluorescence intensity in tumor site revealed that the tumor fluorescence intensity increased in the first-hour post-injection and then decreased over time for all types of ICG-AuNPs (Figure 4.8 a). Meanwhile, the fluorescence contrast index in the tumor site increased over time for all types of ICG-AuNPs and reached a plateau at 10 hours p.i (Figure 4.8 b).

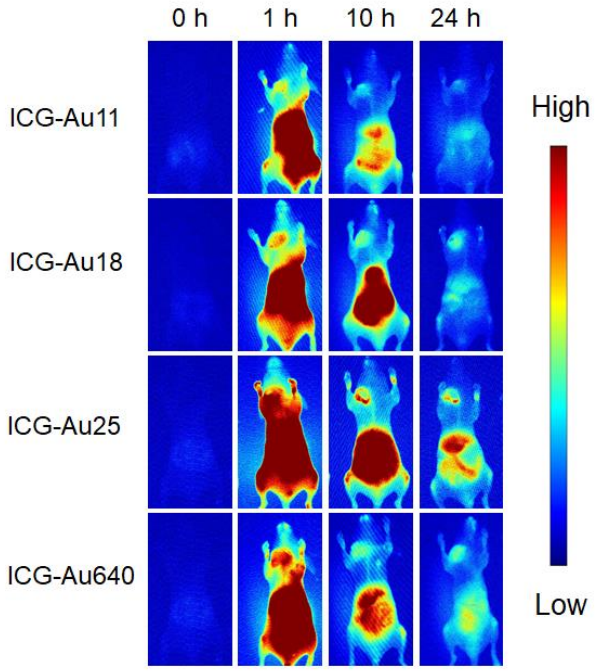

Figure 4.7. The time-dependent noninvasively fluorescence tumor imaging of the 4T-1 tumor-bearing mice with the administration of different-sized ICG-AuNPs.

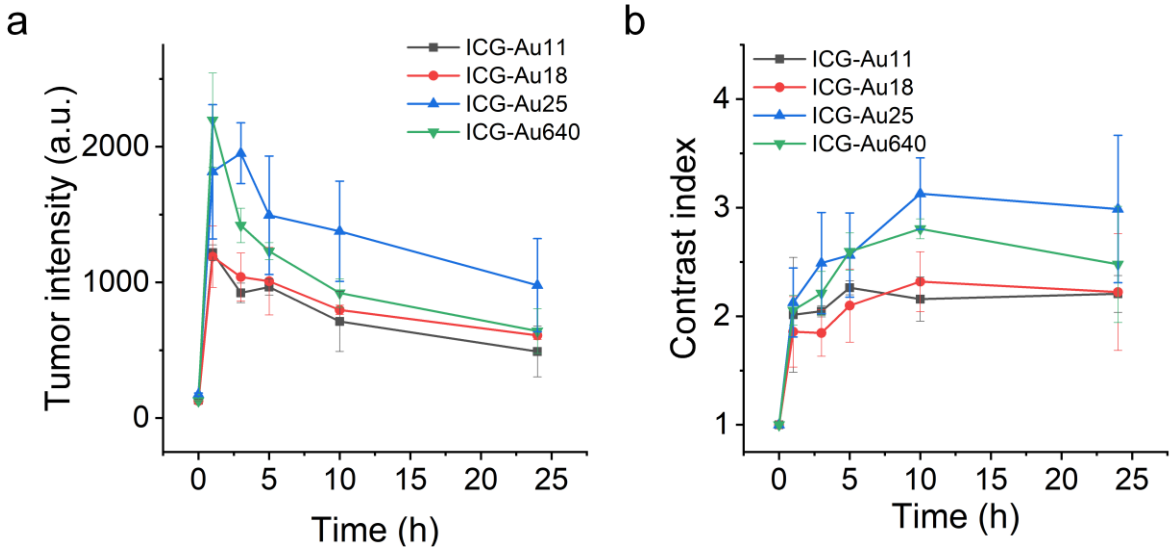

Figure 4.8. The quantitative analysis of (a) the tumor fluorescence intensity of ICG and (b) the contrast index over time.

The AUC (area under the curve) of the time-dependent tumor fluorescence intensity revealed that the tumor-targeting was also size-dependent. The tumor AUC increased as the ICG-AuNCs size increased from Au11to Au18 to Au25, then the AUC decreased as the size increased from 25 to 640. This size-dependent trend was also found in the ICG-based tumor targeting efficiency by quantifying the fluorescence intensity of extracted tumor tissues 24h p.i. of ICG-AuNCs (Figure 4.9 a). The fluorescence intensity (Figure 4.9 b) of extracted tumor tissues increased from 3971±45 to 4392±1031 to 12905±3256 with the size increased from ICG-Au11 to ICG-Au18 to ICG-Au25. The fluorescence intensity decreased from 12905±3256 to 9315±2125 as the size increased from ICG-Au25 to ICG-Au640.

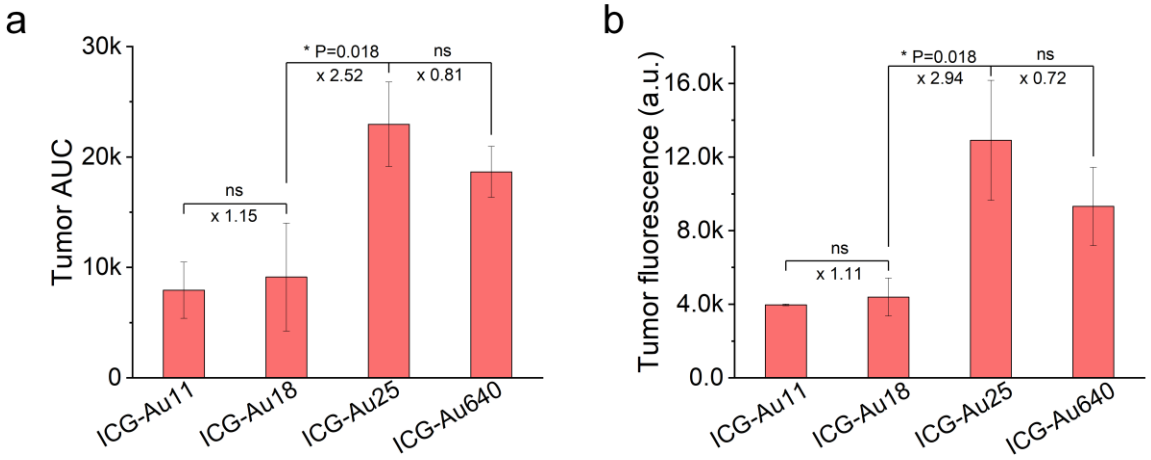

Figure 4.9. The quantitative analysis of time-dependent fluorescence imaging of 4T-1 tumor-bearing mice after administration of different sized ICG-AuNCs. (a) The area under the curve (AUC) of time-dependent fluorescence imaging of 4T-1 tumor-bearing mice after administration of different sized ICG-AuNCs. b) The tumor fluorescence intensity of 4T-1 tumor-bearing mice after administration of different sized ICG-AuNCs.

It is noteworthy that by plotting the fluorescence intensity of extracted tumor tissue at 24h p.i of ICG-AuNCs (Figure 4.7 b) versus the AUC of blood retention of ICG (Figure 3.5 a), we

observed a strong linear correlation among them (Figure 4.8), which suggested that the size dependency of tumor-targeting efficiency was fundamentally due to the size dependency of blood retention. Combing these results, it is clear that the size dependency tumor-targeting effects of ICG-AuNCs in terms of ICG were fundamentally due to the size-dependent blood retention of ICG-AuNCs in terms of ICG. Meanwhile, the size-dependent blood retention of ICG-AuNCs in terms of ICG fundamentally results from the size-dependent nanoparticle-biothiol interactions *in vivo*. Therefore, it is the nanoparticle-biothiol interactions that modulate the blood retention of ICG-AuNPs and therefore modulate the tumor-targeting efficiency of ICG-AuNPs.

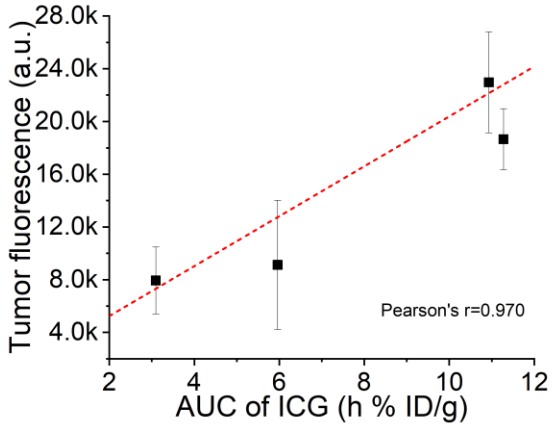

Figure 4.10. The correlation of the blood retention of ICG-AuNPs in terms of ICG and the fluorescence intensity of the tumor tissues extracted from the 4T-1 tumor-bearing mice administrated with different-sized ICG-AuNPs.

After 24 hours p.i. of different-sized ICG-AuNPs, the mice were dissected and the amount of ICG and Au in major organs are quantitatively analyzed. As shown in Figure 4.11 a-d, at 24 hours p.i., the liver displayed the highest fluorescence intensity compared to other organs, which was followed by kidney and tumor for all these four different-sized ICG-AuNPs (Figure 4.11 e). In Figure 4.11 f, the tumor/liver fluorescence ratio for different-sized ICG-AuNPs was quantified and ICG-Au25 was the highest one, followed by ICG-Au640, ICG-Au18, and ICG-Au11. The highest tumor/liver fluorescence ratio of ICG-Au25 was fundamentally due to the lowest liver activation and highest tumor-targeting effect of ICG-Au25 among these four different-sized ICG-AuNPs.

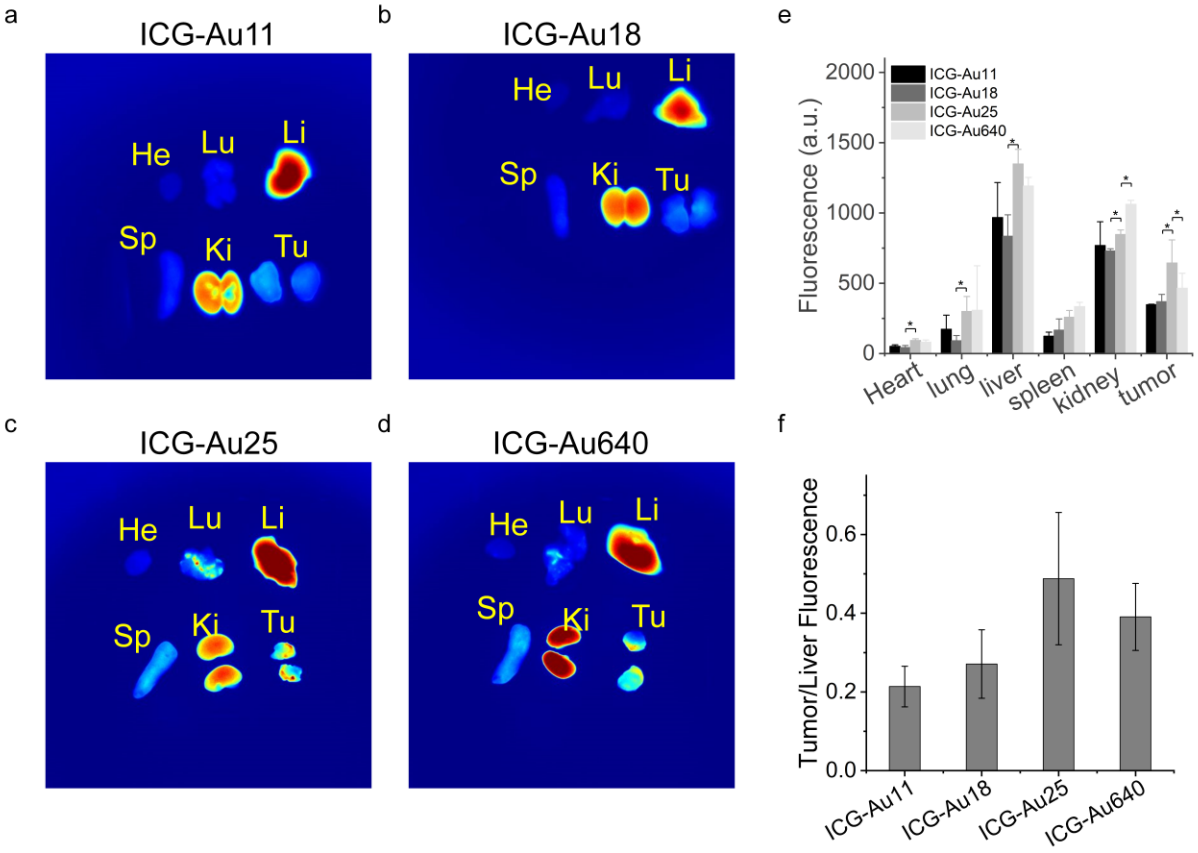

Figure 4.11. Biodistribution of different-sized ICG-AuNPs in tumor-bearing mice at 24 hours p.i. in terms of ICG. a-d, the fluorescence imaging of the biodistribution of (a) ICG-Au11, (b) ICG-Au18, (c) ICG-Au25, and (d) ICG-Au640 in tumor-bearing mice at 24 hours p.i. in terms of ICG. (e) Quantitative analysis of the ICG fluorescence in the major organs. (f) The tumor/liver fluorescence ratio of different-sized ICG-AuNPs in tumor-bearing mice at 24 hours p.i. He: heart; Lu: lung; Li: liver; Sp: spleen; Ki: kidney; Tu: tumor.

Apart from the biodistribution of ICG, the Au amount in the major organs is also investigated. As shown in Figure 4.12, at 24 hours p.i., the kidneys display the highest accumulation of Au, which was fundamental since, after the interactions with biothiols in the liver, the ICG molecules of ICG-AuNPs were detached and were eliminated through the hepatobiliary clearance pathway while the AuNPs were cleared out of the body through the kidney. In Figure 4.12 b, the ratio between the amount of Au in the tumor and liver was quantified. ICG-Au11 exhibits the highest

tumor/liver ratio, followed by ICG-Au18, ICG-Au25, and ICG-Au640. The tumor-targeting effect of ICG-AuNPs in terms of Au was similar to the tumor-targeting effect of free AuNPs which our group reported previously[31], that similar-sized nanoparticles exhibit stronger interactions with kidneys than larger ones and therefore exhibit longer blood retention and higher tumor targeting efficiency than larger ones. Combing these results together indicates the tumor-targeting effect of ICG-AuNPs should be divided into two separate components, the tumor-targeting effect in terms of ICG and the tumor-targeting effect in terms of Au. On one hand, the tumor-targeting effect in terms of Au was fundamentally due to the *in vivo* transport of gold nanoparticles. On the other hand, the tumor-targeting effect in terms of ICG was fundamentally mediated by the interactions between the ICG-AuNPs and the biothiols in the liver.

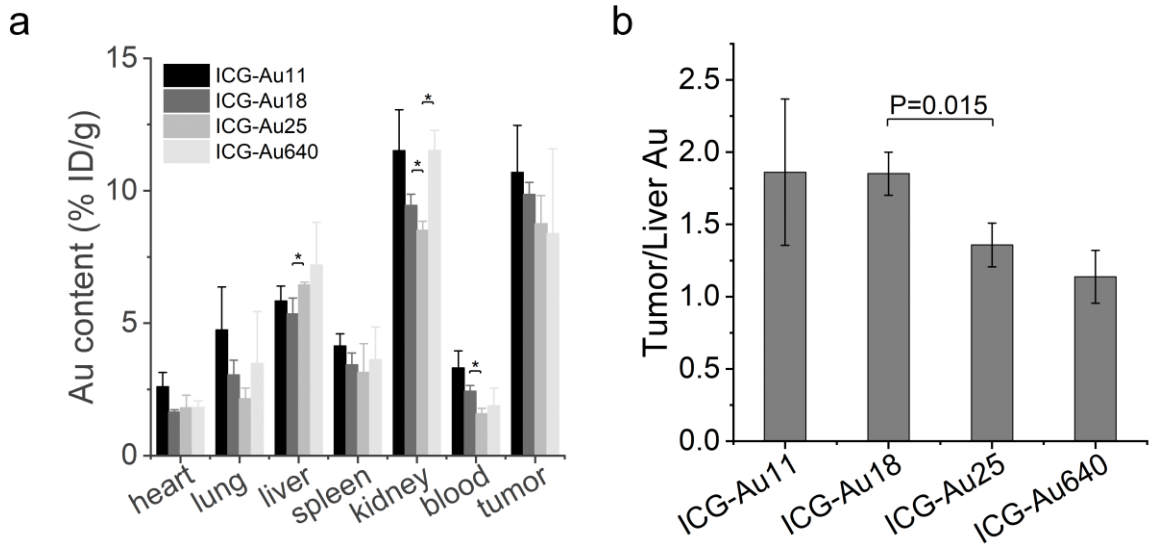

Figure 4.12. Biodistribution of different-sized ICG-AuNPs in tumor-bearing mice at 24 hours p.i. in terms of Au. (a) Quantitative analysis of the ICG fluorescence in the major organs. (b) The amount of Au in Tumor/Liver of different-sized ICG-AuNPs in tumor-bearing mice at 24 hours p.i.

4.4 Conclusions

In summary, we observed the size-dependency of GSH-mediated biotransformation of our thiol-activatable nanoprobes—ICG-AuNPs and such size-dependency tailored the tumor-targeting effect of the ICG-AuNPs. We first compared these nanoparticle-biothiol interactions in normal and disease mice, and we found that the nanoparticle-biothiol interactions in the liver of the normal mice were comparable to the interactions in tumor-bearing mice, which was fundamentally due to the unchanged liver glutathione level between the tumor-bearing mice and the normal mice. Next, we compared the fluorescence reactivity of different-sized ICG-AuNPs in the tumor and liver and we found that the fluorescence reactivity of different-sized ICG-AuNPs in the tumor exhibit a similar size trend, but lower reactivity compared to that in the liver. Such phenomena were fundamental because the ICG-AuNPs can both be activated by the glutathione in the tumor and liver while the liver glutathione concentration is nearly one order higher than that in the tumor, leading to the higher fluorescence reactivity of different-sized ICG-AuNPs in the liver. Then, we observed that this size-dependent nanoparticle-biothiol interaction not only modulates the blood retention of the thiol-activatable nanoprobes but also results in the size-dependent tumor-targeting effect of the different sized nanoprobes. We believe the understanding of nano-bio interactions at the molecular level not only helps us understand physiology at the nanoscale but also provides a foundation for the design of safe and efficacious nanomedicines.

4.5 Experiments

4.5.1 Materials and equipment

ICG-NHS was obtained from AdipoGen Life Science, Inc. Fetal Bovine Serum (FBS) was purchased from Corning, Inc. All the other chemicals were purchased from Sigma-Aldrich and used as received without further purification. Ultra-centrifugal filter units with the molecular weight cut-off (MWCO) of 3k, 10k, and 30k Da (MilliporeSigma™ Amicon™) were utilized for the purification of gold nanoparticles and ICG conjugated gold nanoparticles. The amount of gold was measured by Agilent 7900 inductively coupled plasma mass spectrometry (ICP-MS). The pH was measured by an Accumet AB15 pH meter and an Accuphast microprobe electrode. Agarose gel electrophoresis was carried out in a Bio-Rad Mini-Sub Cell GT system (Bio-Rad Laboratories, Inc. USA). The absorption spectra were collected with a Virian 50 Bio UV-vis spectrophotometer. The luminescence spectra of different-sized nanoparticles were detected with a PTI QuantaMasterTM 30 Fluorescence Spectrophotometer (Birmingham, NJ). The time-dependent fluorescence enhancement of ICG-AuNPs was monitored by the BioTek Synergy H4 plate reader. *In vivo* fluorescence images were recorded using a Carestream In-vivo FX Pro imaging system. Optical images of cultured cells and tissue slides were obtained with an Olympus IX-71 inverted fluorescence microscope coupled with Photon Max 512 CCD camera (Princeton Instruments). Animal studies were performed according to the guidelines of the University of Texas System Institutional Animal Care and Use Committee. BALB/c mice (BALB/cAnNCr, strain code 047) of 6-8 weeks old, weighing 20-25g, were purchased from Envigo. Nude mice (Athymic NCr-nu/nu, strain code 069) of 6-8 weeks old, weighing 20-25 g, were also purchased from Envigo. All of these mice were randomly allocated and housed under

standard environmental conditions (23±1 ℃, 50±5% humidity, and a 12/12 h light/dark cycle) with free access to water and standard laboratory food.s

4.5.2 Methods

Tumor implantation

The human breast cancer cell line 4T1 was cultured in Dulbecco's Modified Eagle Medium (DMEM) with 10% (v/v) fetal bovine serum (FBS) and 1% (v/v) penicillin-streptomycin at 37 ºC in a humidified atmosphere containing 5% CO2. The cell suspension (in DMEM with 10% (v/v) FBS) was then mixed 2:1 (v/v) with matrix gel and injected subcutaneously upper near the mammary fat pad (MFP) area of the Balb/c mice with a volume of 100 µL dense suspension (containing about 1×106 cells) for each mouse. The tumor was allowed to grow ~1 week and reach a ~6-8 mm size before the study.

Biodistribution study of different-sized ICG-AuNPs

BALB/c mice were i.v. injected with 150 µL ICG-AuNPs (the amount of ICG was about 20 µM the amount of ICG, in PBS) per mouse. At a certain time point post-injection, Organs/tissues were collected and weighed following the sacrifice of mice and then completely digested in aqua regia to determine the Au content via ICP-MS. The ICG content in different organs/tissues was quantified by the fluorescence of ICG using the *in vivo* imaging system.

The quantification of the concentration of liver glutathione concentration

The mice were dissected and about 0.4 g of liver tissues were collected. The liver tissues were immediately stored in liquid nitrogen for the future quantification of the concentration of liver

glutathione concentration. The quantification of the liver GSH level was performed according to the modified Tietze enzymatic recycling assay, which was published previously[81].

Statistics and reproducibility

Welch's t-test was used to compare two groups of data and analysis of variance (ANOVA) was used for the comparison of multiple data points among data sets. Data were reported as mean values with error bars representing the standard deviation. Differences were considered statistically significant when $P < 0.05$. Unless otherwise specified, all of the experiments were repeated at least three times with similar results to ensure reproducibility.

4.6 Acknowledgements

This study was in part supported by the NIH (1R01DK115986), NIH (1R01DK126140), and CPRIT (PR200233), from the University of Texas at Dallas (J.Z).

4.7 Author contributions

J.Z. conceived the idea and designed experiments with Q.Z.; Q.Z. performed *in vitro* experiments and analyzed data with J.Z.; S.L. and Y.H. assisted with *in vitro* experiment; Q.Z. wrote the manuscript; J.Z revised the manuscript; J.Z. supervised the whole project. All authors discussed the results and commented on the manuscript.

CHAPTER 5

SUMMARY AND OUTLOOK

Authors – Qinhan Zhou, Siqing Li, Yingyu Huang, and Jie Zheng

Department of Chemistry and Biochemistry, BSB 13

The University of Texas at Dallas

800 West Campbell Road

Richardson, Texas 75080, USA

5.1 Summary

In this thesis, we fundamentally investigate one type of nano-biochemical interaction. We used the atomically precise gold-dye hybrid nanoparticles with activatable fluorescence (ICG-AuNPs) to explore nano-biochemical interactions at the *in vitro* level, in the normal organs as well as tumors. We first synthesized and purified the different-sized ICG-AuNPs, followed by the careful characterization of the physical and physicochemical properties of the ICG-AuNPs. Then, a systematic investigation of the interactions between the thiols and the different-sized ICG-AuNPs was performed at *in vitro* level. We explored the influence of the nanoparticle size, thiol species, and protein binding on the interactions between the thiols and the different-sized ICG-AuNPs. After *in vitro* study, we conducted the research on the interactions of nanoparticle-biothiol at *in vivo* level and correlated the interactions of nanoparticle-biothiol *in vitro* with the interactions *in vivo*. In this section, we systematically investigated the size of nanoparticles affects the nanoparticle-biothiol interactions in the liver. Then, we studied how these nanoparticle-biothiol interactions in the liver affect the *in vivo* transport of nanoparticles. It was noteworthy that the blood retention of ICG-AuNPs was modulated by the interactions of nanoparticle-biothiol in the liver, where stronger nanoparticle-thiol interactions in the liver would result in the lower blood retentions of nanoparticles.

After investigating the interactions of nanoparticle-biothiol in the healthy mice, we would like to verify whether these interactions exist in diseased mice and how these interactions affect the *in vivo* behavior of the nanoparticles in the diseased mice. In this section, we discovered the size-dependent tumor-targeting effect of ICG-AuNPs, and such size-dependency was due to the size-dependent blood retention of ICG-AuNPs. The size-dependent blood retention of ICG-AuNPs

fundamentally arose from the size-dependent nanoparticle-biothiol interactions in the liver. Therefore, to achieve the highest tumor-targeting effect of the engineered nanoparticles, it is necessary to modulate the nanoparticle-biothiol interactions. These new understanding on nano-biochemical interactions at both *in vitro* and *in vivo* levels will help further advance physiology at the nanoscale as well as open new pathways to early disease diagnosis and treatment.

5.2 Outlook

In this dissertation, we investigate the nano-biochemical interactions at both the *in vitro* and the *in vivo* levels. We also study the nano-biochemical interactions at normal and disease conditions. We comprehensively investigate how the nano-biochemical interactions affect the tumor-targeting efficiency of our nanomaterials. In future research, we will focus on two directions to further explore the study of nano-biochemical interactions. First, we would investigate the interactions of nanoparticles with other biochemicals at both *in vitro* level and *in vivo* levels and the correlation of these interactions *in vitro* and *in vivo*. Second, it is necessary to explore the nano-biochemical interactions in other disease models like diabetes, liver fibrosis, and cirrhosis model. It is noteworthy that the difference in nanomaterials behaviors between the normal and disease conditions could be attributed to either the difference of nanomaterials transport between the normal and disease conditions or the difference of nano-bio interactions between the normal and disease conditions. These two factors need to be decoupled in the future when we investigate the *in vivo* behavior of nanomaterials in disease conditions.

REFERENCES

1.Peng, C.; Xu, J.; Yu, M.; Ning, X.; Huang, Y.; Du, B.; Hernandez, E.; Kapur, P.; Hsieh, J. T.; Zheng, J., Tuning the In Vivo Transport of Anticancer Drugs Using Renal-Clearable Gold Nanoparticles. *Angewandte Chemie* **2019**.

2.Peng, C.; Yu, M.; Hsieh, J. T.; Kapur, P.; Zheng, J., Correlating Anticancer Drug Delivery Efficiency with Vascular Permeability of Renal Clearable Versus Non-renal Clearable Nanocarriers. *Angewandte Chemie* **2019,** *131* (35), 12204-12208.

3.Barreto, J. A.; O'Malley, W.; Kubeil, M.; Graham, B.; Stephan, H.; Spiccia, L., Nanomaterials: Applications in Cancer Imaging and Therapy. *Advanced Materials* **2011,** *23* (12), H18-H40.

4.Abd Elkodous, M.; El-Sayyad, G. S.; Abdelrahman, I. Y.; El-Bastawisy, H. S.; Mosallam, F. M.; Nasser, H. A.; Gobara, M.; Baraka, A.; Elsayed, M. A.; El-Batal, A. I., Therapeutic and diagnostic potential of nanomaterials for enhanced biomedical applications. *Colloids and Surfaces B: Biointerfaces* **2019,** *180*, 411-428.

5.Brigger, I.; Dubernet, C.; Couvreur, P., Nanoparticles in cancer therapy and diagnosis. *Advanced drug delivery reviews* **2012,** *64*, 24-36.

6.Zhang, X.-Q.; Xu, X.; Bertrand, N.; Pridgen, E.; Swami, A.; Farokhzad, O. C., Interactions of nanomaterials and biological systems: Implications to personalized nanomedicine. *Advanced drug delivery reviews* **2012,** *64* (13), 1363-1384.

7.Liu, J.; Yu, M.; Zhou, C.; Yang, S.; Ning, X.; Zheng, J., Passive Tumor Targeting of Renal-Clearable Luminescent Gold Nanoparticles: Long Tumor Retention and Fast Normal Tissue Clearance. *Journal of the American Chemical Society* **2013,** *135* (13), 4978-4981.

8.Du, B.; Chong, Y.; Jiang, X.; Yu, M.; Lo, U. G.; Dang, A.; Chen, Y. A.; Li, S.; Hernandez, E.; Lin, J. C.; Hsieh, J. T.; Zheng, J., Hyperfluorescence Imaging of Kidney Cancer Enabled by Renal Secretion Pathway Dependent Efflux Transport. *Angewandte Chemie International Edition* **2020**.

9.Jiang, X.; Zhou, Q.; Du, B.; Li, S.; Huang, Y.; Chi, Z.; Lee, W. M.; Yu, M.; Zheng, J., Noninvasive monitoring of hepatic glutathione depletion through fluorescence imaging and blood testing. *Science Advances* **2021,** *7* (8), eabd9847.

10.Jiang, X.; Du, B.; Zheng, J., Glutathione-mediated biotransformation in the liver modulates nanoparticle transport. *Nature nanotechnology* **2019,** *14* (9), 874-882.

11.Riley, M.; Vermerris, W., Recent Advances in Nanomaterials for Gene Delivery—A Review. *Nanomaterials* **2017,** *7* (5), 94.

12.Park, J.; Kim, W. J., Current status of gene delivery: spotlight on nanomaterial-polymer hybrids. *Journal of drug targeting* **2012,** *20* (8), 648-666.

13.Blanco, E.; Shen, H.; Ferrari, M., Principles of nanoparticle design for overcoming biological barriers to drug delivery. *Nature Biotechnology* **2015,** *33* (9), 941-951.

14.Tsoi, K. M.; Macparland, S. A.; Ma, X.-Z.; Spetzler, V. N.; Echeverri, J.; Ouyang, B.; Fadel, S. M.; Sykes, E. A.; Goldaracena, N.; Kaths, J. M.; Conneely, J. B.; Alman, B. A.; Selzner, M.; Ostrowski, M. A.; Adeyi, O. A.; Zilman, A.; McGilvray, I. D.; Chan, W. C. W., Mechanism of hard-nanomaterial clearance by the liver. *Nature Materials* **2016,** *15* (11), 1212-1221.

15.Wang, L.; Yan, L.; Liu, J.; Chen, C.; Zhao, Y., Quantification of Nanomaterial/Nanomedicine Trafficking in Vivo. *Analytical Chemistry* **2018,** *90* (1), 589-614.

16.Zolnik, B. S.; Sadrieh, N., Regulatory perspective on the importance of ADME assessment of nanoscale material containing drugs. *Advanced drug delivery reviews* **2009,** *61* (6), 422-427.

17.Owens III, D. E.; Peppas, N. A., Opsonization, biodistribution, and pharmacokinetics of polymeric nanoparticles. *International journal of pharmaceutics* **2006,** *307* (1), 93-102.

18.Li, S.-D.; Huang, L., Pharmacokinetics and Biodistribution of Nanoparticles. *Molecular Pharmaceutics* **2008,** *5* (4), 496-504.

19.Almeida, J. P. M.; Chen, A. L.; Foster, A.; Drezek, R., In vivo biodistribution of nanoparticles. *Nanomedicine* **2011,** *6* (5), 815-835.

20.Hoshyar, N.; Gray, S.; Han, H.; Bao, G., The effect of nanoparticle size on in vivo pharmacokinetics and cellular interaction. *Nanomedicine* **2016,** *11* (6), 673-692.

21.Yu, M.; Zheng, J., Clearance Pathways and Tumor Targeting of Imaging Nanoparticles. *ACS Nano* **2015,** *9* (7), 6655-6674.

22.Poon, W.; Zhang, Y.-N.; Ouyang, B.; Kingston, B. R.; Wu, J. L. Y.; Wilhelm, S.; Chan, W. C. W., Elimination Pathways of Nanoparticles. *ACS Nano* **2019,** *13* (5), 5785-5798.

23.Du, B.; Yu, M.; Zheng, J., Transport and interactions of nanoparticles in the kidneys. *Nature Reviews Materials* **2018,** *3* (10), 358-374.

24.Walkey, C. D.; Chan, W. C. W., Understanding and controlling the interaction of nanomaterials with proteins in a physiological environment. *Chem. Soc. Rev.* **2012,** *41* (7), 2780-2799.

25.Zhang, Y.; Wu, J. L.; Lazarovits, J.; Chan, W. C., An analysis of the binding function and structural organization of the protein corona. *Journal of the American Chemical Society* **2020,** *142* (19), 8827-8836.

26.Zamboni, W. C., Liposomal, Nanoparticle, and Conjugated Formulations of Anticancer Agents. *Clinical Cancer Research* **2005,** *11* (23), 8230-8234.

27.Lazarovits, J.; Chen, Y. Y.; Sykes, E. A.; Chan, W. C. W., Nanoparticle–blood interactions: the implications on solid tumour targeting. *Chemical Communications* **2015,** *51* (14), 2756-2767.

28.Setyawati, M. I.; Tay, C. Y.; Docter, D.; Stauber, R. H.; Leong, D. T., Understanding and exploiting nanoparticles' intimacy with the blood vessel and blood. *Chemical Society Reviews* **2015,** *44* (22), 8174-8199.

29.Soo Choi, H.; Liu, W.; Misra, P.; Tanaka, E.; Zimmer, J. P.; Itty Ipe, B.; Bawendi, M. G.; Frangioni, J. V., Renal clearance of quantum dots. *Nature Biotechnology* **2007,** *25* (10), 1165-1170.

30.Zhou, C.; Long, M.; Qin, Y.; Sun, X.; Zheng, J., Luminescent Gold Nanoparticles with Efficient Renal Clearance. *Angewandte Chemie International Edition* **2011,** *50* (14), 3168-3172.

31. Du, B.; Jiang, X.; Das, A.; Zhou, Q.; Yu, M.; Jin, R.; Zheng, J., Glomerular barrier behaves as an atomically precise bandpass filter in a sub-nanometre regime. *Nature Nanotechnology* **2017,** *12* (11), 1096-1102.

32.Zhang, Y.-N.; Poon, W.; Tavares, A. J.; McGilvray, I. D.; Chan, W. C. W., Nanoparticle–liver interactions: Cellular uptake and hepatobiliary elimination. *Journal of Controlled Release* **2016,** *240*, 332-348.

33.Loynachan, C. N.; Soleimany, A. P.; Dudani, J. S.; Lin, Y.; Najer, A.; Bekdemir, A.; Chen, Q.; Bhatia, S. N.; Stevens, M. M., Renal clearable catalytic gold nanoclusters for in vivo disease monitoring. *Nature Nanotechnology* **2019,** *14* (9), 883-890.

34.Huang, J.; Lyu, Y.; Li, J.; Cheng, P.; Jiang, Y.; Pu, K., A Renal-Clearable Duplex Optical Reporter for Real-Time Imaging of Contrast-Induced Acute Kidney Injury. *Angewandte Chemie* **2019,** *131* (49), 17960-17968.

35.Kane, R. S.; Stroock, A. D., Nanobiotechnology: Protein-Nanomaterial Interactions. *Biotechnology Progress* **2007,** *23* (2), 316-319.

36.Walkey, C. D.; Olsen, J. B.; Guo, H.; Emili, A.; Chan, W. C. W., Nanoparticle Size and Surface Chemistry Determine Serum Protein Adsorption and Macrophage Uptake. *Journal of the American Chemical Society* **2012,** *134* (4), 2139-2147.

37.Glancy, D.; Zhang, Y.; Wu, J. L. Y.; Ouyang, B.; Ohta, S.; Chan, W. C. W., Characterizing the protein corona of sub-10 nm nanoparticles. *Journal of Controlled Release* **2019,** *304*, 102-110.

38.García-Álvarez, R.; Hadjidemetriou, M.; Sánchez-Iglesias, A.; Liz-Marzán, L. M.; Kostarelos, K., In vivo formation of protein corona on gold nanoparticles. The effect of their size and shape. *Nanoscale* **2018,** *10* (3), 1256-1264.

39.Madathiparambil Visalakshan, R.; González García, L. E.; Benzigar, M. R.; Ghazaryan, A.; Simon, J.; Mierczynska-Vasilev, A.; Michl, T. D.; Vinu, A.; Mailänder, V.; Morsbach, S.; Landfester, K.; Vasilev, K., The Influence of Nanoparticle Shape on Protein Corona Formation. *Small* **2020,** *16* (25), 2000285.

40.Benetti, F.; Fedel, M.; Minati, L.; Speranza, G.; Migliaresi, C., Gold nanoparticles: role of size and surface chemistry on blood protein adsorption. *Journal of Nanoparticle Research* **2013,** *15* (6).

41.Pozzi, D.; Caracciolo, G.; Capriotti, A. L.; Cavaliere, C.; La Barbera, G.; Anchordoquy, T. J.; Laganà, A., Surface chemistry and serum type both determine the nanoparticle–protein corona. *Journal of Proteomics* **2015,** *119*, 209-217.

42.Tavares, A. J.; Poon, W.; Zhang, Y.-N.; Dai, Q.; Besla, R.; Ding, D.; Ouyang, B.; Li, A.; Chen, J.; Zheng, G.; Robbins, C.; Chan, W. C. W., Effect of removing Kupffer cells on nanoparticle tumor delivery. *Proceedings of the National Academy of Sciences* **2017,** *114* (51), E10871-E10880.

43.Zhang, Y.-N.; Poon, W.; Sefton, E.; Chan, W. C. W., Suppressing Subcapsular Sinus Macrophages Enhances Transport of Nanovaccines to Lymph Node Follicles for Robust Humoral Immunity. *ACS Nano* **2020,** *14* (8), 9478-9490.

44.Liu, J.; Chen, Q.; Feng, L.; Liu, Z., Nanomedicine for tumor microenvironment modulation and cancer treatment enhancement. *Nano Today* **2018,** *21*, 55-73.

45.Yang, S.; Gao, H., Nanoparticles for modulating tumor microenvironment to improve drug delivery and tumor therapy. *Pharmacological Research* **2017,** *126*, 97-108.

46.Liu, Y.; Guo, J.; Huang, L., Modulation of tumor microenvironment for immunotherapy: focus on nanomaterial-based strategies. *Theranostics* **2020,** *10* (7), 3099.

47.Kalanaky, S.; Hafizi, M.; Safari, S.; Mousavizadeh, K.; Kabiri, M.; Farsinejad, A.; Fakharzadeh, S.; Nazaran, M. H., TLc-A, the leading nanochelating-based nanochelator, reduces iron overload in vitro and in vivo. *International journal of hematology* **2016,** *103* (3), 274-282.

48.Yang, Y.; Tang, J.; Zhang, M.; Gu, Z.; Song, H.; Yang, Y.; Yu, C., Responsively Aggregatable Sub-6 nm Nanochelators Induce Simultaneous Antiangiogenesis and Vascular Obstruction for Enhanced Tumor Vasculature Targeted Therapy. *Nano Letters* **2019,** *19* (11), 7750-7759.

49.Kang, H.; Han, M.; Xue, J.; Baek, Y.; Chang, J.; Hu, S.; Nam, H.; Jo, M. J.; El Fakhri, G.; Hutchens, M. P.; Choi, H. S.; Kim, J., Renal clearable nanochelators for iron overload therapy. *Nature Communications* **2019,** *10* (1).

50.Wang, J.; Wang, K.; Zhu, Z.; He, Y.; Zhang, C.; Guo, Z.; Wang, X., Inhibition of metal-induced amyloid β-peptide aggregation by a blood–brain barrier permeable silica–cyclen nanochelator. *RSC Advances* **2019,** *9* (25), 14126-14131.

51.Jones, G.; Goswami, S. K.; Kang, H.; Choi, H. S.; Kim, J., Combating iron overload: a case for deferoxamine-based nanochelators. *Nanomedicine* **2020,** (0).

52.Yang, B.; Chen, Y.; Shi, J., Reactive oxygen species (ROS)-based nanomedicine. *Chemical reviews* **2019,** *119* (8), 4881-4985.

53.Hou, Z.; Zhang, Y.; Deng, K.; Chen, Y.; Li, X.; Deng, X.; Cheng, Z.; Lian, H.; Li, C.; Lin, J., UV-emitting upconversion-based TiO2 photosensitizing nanoplatform: near-infrared light mediated in vivo photodynamic therapy via mitochondria-involved apoptosis pathway. *ACS nano* **2015,** *9* (3), 2584-2599.

54.Zheng, C.; Zheng, M.; Gong, P.; Jia, D.; Zhang, P.; Shi, B.; Sheng, Z.; Ma, Y.; Cai, L., Indocyanine green-loaded biodegradable tumor targeting nanoprobes for in vitro and in vivo imaging. *Biomaterials* **2012,** *33* (22), 5603-9.

55.Li, L.; Guo, J.; Wang, Y.; Xiong, X.; Tao, H.; Li, J.; Jia, Y.; Hu, H.; Zhang, J., A Broad-Spectrum ROS-Eliminating Material for Prevention of Inflammation and Drug-Induced Organ Toxicity. *Advanced Science* **2018,** *5* (10), 1800781.

56.Shuhendler, A. J.; Pu, K.; Cui, L.; Uetrecht, J. P.; Rao, J., Real-time imaging of oxidative and nitrosative stress in the liver of live animals for drug-toxicity testing. *Nature Biotechnology* **2014,** *32* (4), 373-380.

57.Holzinger, M.; Le Goff, A.; Cosnier, S., Nanomaterials for biosensing applications: a review. *Frontiers in chemistry* **2014,** *2*, 63.

58.Han, X.; Xu, K.; Taratula, O.; Farsad, K., Applications of nanoparticles in biomedical imaging. *Nanoscale* **2019,** *11* (3), 799-819.

59.Peng, C.; Huang, Y.; Zheng, J., Renal clearable nanocarriers: Overcoming the physiological barriers for precise drug delivery and clearance. *Journal of Controlled Release* **2020,** *322*, 64-80.

60.Couvreur, P., Nanoparticles in drug delivery: past, present and future. *Advanced drug delivery reviews* **2013,** *65* (1), 21-23.

61.Wang, Y.; Cai, R.; Chen, C., The Nano–Bio Interactions of Nanomedicines: Understanding the Biochemical Driving Forces and Redox Reactions. *Accounts of Chemical Research* **2019,** *52* (6), 1507-1518.

62.Tian, X.; Chong, Y.; Ge, C., Understanding the Nano–Bio Interactions and the Corresponding Biological Responses. *Frontiers in Chemistry* **2020,** *8*.

63.Wang, X.; Cui, X.; Zhao, Y.; Chen, C., Nano-bio interactions: the implication of size-dependent biological effects of nanomaterials. *Science China Life Sciences* **2020,** *63*, 1168-1182.

64.Pearson, R. M.; Hsu, H.-J.; Bugno, J.; Hong, S., Understanding nano-bio interactions to improve nanocarriers for drug delivery. *MRS Bulletin* **2014,** *39* (3), 227-237.

65.Bertrand, N.; Grenier, P.; Mahmoudi, M.; Lima, E. M.; Appel, E. A.; Dormont, F.; Lim, J.-M.; Karnik, R.; Langer, R.; Farokhzad, O. C., Mechanistic understanding of in vivo protein corona formation on polymeric nanoparticles and impact on pharmacokinetics. *Nature Communications* **2017,** *8* (1).

66.Wu, G.; Fang, Y.-Z.; Yang, S.; Lupton, J. R.; Turner, N. D., Glutathione metabolism and its implications for health. *The Journal of nutrition* **2004,** *134* (3), 489-492.

67.Chevrier, D. M.; Thanthirige, V. D.; Luo, Z.; Driscoll, S.; Cho, P.; Macdonald, M. A.; Yao, Q.; Guda, R.; Xie, J.; Johnson, E. R.; Chatt, A.; Zheng, N.; Zhang, P., Structure and formation of highly luminescent protein-stabilized gold clusters. *Chemical Science* **2018,** *9* (10), 2782-2790.

68.Yao, Q.; Yu, Y.; Yuan, X.; Yu, Y.; Xie, J.; Lee, J. Y., Two-Phase Synthesis of Small Thiolate-Protected Au15and Au18Nanoclusters. *Small* **2013,** *9* (16), 2696-2701.

69.Wu, Z.; Suhan, J.; Jin, R., One-pot synthesis of atomically monodisperse, thiol-functionalized Au25nanoclusters. *J. Mater. Chem.* **2009,** *19* (5), 622-626.

70.Liu, J.; Duchesne, P. N.; Yu, M.; Jiang, X.; Ning, X.; Vinluan, R. D.; Zhang, P.; Zheng, J., Luminescent Gold Nanoparticles with Size-Independent Emission. *Angewandte Chemie International Edition* **2016,** *55* (31), 8894-8898.

71.Yu, Y.; Chen, X.; Yao, Q.; Yu, Y.; Yan, N.; Xie, J., Scalable and Precise Synthesis of Thiolated Au10–12, Au15, Au18, and Au25Nanoclusters via pH Controlled CO Reduction. *Chemistry of Materials* **2013,** *25* (6), 946-952.

72.Wu, Z.; Gayathri, C.; Gil, R. R.; Jin, R., Probing the Structure and Charge State of Glutathione-Capped Au25(SG)18 Clusters by NMR and Mass Spectrometry. *Journal of the American Chemical Society* **2009,** *131* (18), 6535-6542.

73.Negishi, Y.; Nobusada, K.; Tsukuda, T., Glutathione-Protected Gold Clusters Revisited: Bridging the Gap between Gold(I)−Thiolate Complexes and Thiolate-Protected Gold Nanocrystals. *Journal of the American Chemical Society* **2005,** *127* (14), 5261-5270.

74.Jin, R., Atomically precise metal nanoclusters: stable sizes and optical properties. *Nanoscale* **2015,** *7* (5), 1549-1565.

75.Zhu, M.; Aikens, C. M.; Hollander, F. J.; Schatz, G. C.; Jin, R., Correlating the Crystal Structure of A Thiol-Protected Au25Cluster and Optical Properties. *Journal of the American Chemical Society* **2008,** *130* (18), 5883-5885.

76. Tsuno, K., Resolution limit of a transmission electron microscope with an uncorrected conventional magnetic objective lens. *Ultramicroscopy* **1993,** *50* (3), 245-253.

77.Katla, S. K.; Zhang, J.; Castro, E.; Bernal, R. A.; Li, X., Atomically Precise Au25(SG)18 Nanoclusters: Rapid Single-Step Synthesis and Application in Photothermal Therapy. *ACS Applied Materials & Interfaces* **2018,** *10* (1), 75-82.

78.Armstrong, J. K.; Wenby, R. B.; Meiselman, H. J.; Fisher, T. C., The Hydrodynamic Radii of Macromolecules and Their Effect on Red Blood Cell Aggregation. *Biophysical journal* **2004,** *87* (6), 4259-4270.

79.Ren, C.; Liu, D.; Qu, L.; Tan, R., Synthesis of hydroxyapatite nanoparticles in ultrasonic precipitation. *Jiamusi Daxue Xuebao, Ziran Kexueban* **2009,** *27* (3), 402-404.

80.Shichibu, Y.; Negishi, Y.; Tsunoyama, H.; Kanehara, M.; Teranishi, T.; Tsukuda, T., Extremely High Stability of Glutathionate-Protected Au25 Clusters Against Core Etching. *Small* **2007,** *3* (5), 835-839.

81.Rahman, I.; Kode, A.; Biswas, S. K., Assay for quantitative determination of glutathione and glutathione disulfide levels using enzymatic recycling method. *Nature Protocols* **2006,** *1* (6), 3159-3165.

BIOGRAPHICAL SKETCH

Qinhan Zhou was born in Huaian, Jiangsu, China. He got his BS degree in chemistry at the Beijing Institute of Technology, China in 2015. In Fall 2016, he joined Dr. Jie Zheng's lab in the Department of Chemistry and Biochemistry at The University of Texas at Dallas to pursue his PhD.

CURRICULUM VITAE

Qinhan Zhou

Qinhan.zhou@utdallas.edu

PhD in Chemistry, with experience in nanomedicine and disease detection

Research Interest

- Cancer immunotherapy
- Nanoparticle-enabled disease detection
- Fundamental understanding of nano-bio interactions

Education

December 2021 (expected)	**PhD in Chemistry** *The University of Texas at Dallas*
June 2015	**BS in Applied Chemistry** *Beijing Institute of Technology*

Research Experience

2016 - present	Research assistant
2013 - 2015	Undergraduate researcher • Fabrication of multifunctional graphene-based foams • Preparation of micro-fiber supercapacitor

Awards and Honors

2016	Graduate Studies Scholarship	*The University of Texas at Dallas*
2015	*Excellent graduation thesis*	*Beijing Institute of Technology*
2013	*China Century Group Scholarship*	*Beijing Institute of Technology*
2013	*1st Prize of the 5th Beijing College Students Chemistry Experiment Competition*	*Beijing, China*

Skills

Experimental Skills	Animal handling	IV injection, Dissection, Blood perfusion, Surgery Pharmacokinetics, Renal clearance, Biodistribution, Preclinical animal in vivo fluorescence imaging, Histology (H&E staining), Flow cytometry
	Nanoparticle characterization	UV/Vis spectroscopy, Fluorescence spectroscopy, Transmission electron microscopy, Optical microscopy, ICP-MS, DLS, HPLC, Gel electrophoresis
Computing Skills	Data analysis and visualization	Microsoft Office, Origin, ImageJ, Endnote, Adobe Photoshop, Adobe Illustrator

Publications

- *Zhou, Q.; Li, S.; Huang, Y.; Hernandez, E.; Zheng, J., Thiol activatable indocyanine green conjugated gold nanoprobes exhibits contradictory tumor-targeting effects for ICG and gold.* To be submitted.
- *Jiang, X.[1]; Zhou, Q.[1]; Du, B.; Li, S.; Huang, Y.; Chi, Z.; Lee, W. M.; Yu, M.; Zheng, J., Noninvasive monitoring of hepatic glutathione depletion through fluorescence imaging and blood testing.* Science Advances *2021, 7 (8), eabd9847. (Both authors contributed equally)*
- *Xu, J.; Yu, M.; Peng, C.; Carter, P.; Tian, J.; Ning, X.; Zhou, Q.; Tu, Q.; Zhang, G.; Dao, A., Dose Dependencies and Biocompatibility of Renal Clearable Gold Nanoparticles: From Mice to Non-human Primates.* Angew. Chem. Int. Ed. *2018, 57, 266 –271.*
- *Du, B.; Jiang, X.; Das, A.; Zhou, Q.; Yu, M.; Jin, R.; Zheng, J., Glomerular barrier behaves as an atomically precise bandpass filter in a sub-nanometre regime.* Nature Nanotechnology *2017, 12 (11), 1096-1102.*
- *Liang, Y.; Liu, F.; Deng, Y.; Zhou, Q.; Cheng, Z.; Zhang, P.; Xiao, Y.; Lv, L.; Liang, H.; Han, Q.; Shao, H.; Qu, L., A Cut-Resistant and Highly Restorable Graphene Foam. Small 2018, 14 (38), 1801916.*
- *Liang, Y.; Zhao, F.; Cheng, Z.; Zhou, Q.; Shao, H.; Jiang, L.; Qu, L., Self-powered wearable graphene fiber for information expression. Nano Energy 2017, 32, 329-335.*
- *Zhang, P.; Lv, L.; Cheng, Z.; Liang, Y.; Zhou, Q.; Zhao, Y.; Qu, L., Superelastic, Macroporous Polystyrene-Mediated Graphene Aerogels for Active Pressure Sensing. Chemistry - An Asian Journal 2016, 11 (7), 1071-1075.*